Characteristic and Sensing Properties of Near- and Mid-Infrared Optical Fibres

Hongxia Li

Submitted for the degree of Doctor of Philosophy

Heriot-Watt University

School of Engineering and Physical Sciences

August, 2009

ACADEMIC REGISTRY
Research Thesis Submission

Name*:*	Hongxia Li		
School/PGI:	School of Engineering and Physical Sciences （EPS）		
Version: *(i.e. First, Resubmission, Final)*	Final Submission	Degree Sought (Award **and** Subject area)	PhD

Declaration

In accordance with the appropriate regulations I hereby submit my thesis and I declare that:

1) the thesis embodies the results of my own work and has been composed by myself
2) where appropriate, I have made acknowledgement of the work of others and have made reference to work carried out in collaboration with other persons
3) the thesis is the correct version of the thesis for submission and is the same version as any electronic versions submitted*.
4) my thesis for the award referred to, deposited in the Heriot-Watt University Library, should be made available for loan or photocopying and be available via the Institutional Repository, subject to such conditions as the Librarian may require
5) I understand that as a student of the University I am required to abide by the Regulations of the University and to conform to its discipline.

* *Please note that it is the responsibility of the candidate to ensure that the correct version of the thesis is submitted.*

Signature of candidate*:*	Hongxia Li	Date:	01-May-2010

Submission

Submitted By *(name in capitals):*	
Signature of Individual Submitting:	
Date Submitted:	

For Completion in Academic Registry

Received in the Academic Registry by *(name in capitals):*			
Method of Submission *(Handed in to Academic Registry; posted through internal/external mail):*			
*E-thesis Submitted (**mandatory for final theses from January 2009)***			
Signature:		Date:	

Please note this form should bound into the submitted thesis.

Updated February 2008, November 2008, February 2009

Abstract

The work within this thesis investigates the characteristics and sensing properties of novel near- and mid-infrared tellurite and germanate glass fibres and their potential as sensing elements.

An asymmetric splicing method for fusion-splicing tellurite and germanate glass fibres to standard silica fibre is demonstrated. The thermal and strain sensing properties of these glass fibres have been studied by analysing the properties of optical fibre Fabry-Perot cavities, which were formed when these high refractive index fibres were spliced to silica fibre, and fibre Bragg gratings. Using fibre F-P interferometer, the normalized thermal sensitivity of tellurite and germanate fibre was measured to be 10.76×10^{-6}/°C and 15.56×10^{-6}/°C respectively, and the normalized strain sensitivity of tellurite and germanate fibre was also measured with values of 0.676×10^{-6} /με and 0.817×10^{-6} /με respectively. These results show good agreement with measurements using fibre Bragg gratings in these fibres and are reasonably consistent with the values predicted using available published data for glasses of similar compositions. Tellurite and germanate glass fibres show potential as thermal sensing and load sensing elements compared with silica fibre.

The design of an evanescent field gas sensor using tapered germanate fibre for methane gas species detection was investigated and modelled. This model shows the maximum gas cell length (sensing fibre length), detectable gas concentration range, and required gas cell length range for the expected minimum detectable gas concentration of a fibre evanescent field sensor, which gives guidance for the effective gas cell length choosen according to different minimum detectable gas concentration requirement in practise.

The investigation of tellurite and germanate glass fibre characteristics and sensing properties offer guidance for their applications in sensing areas.

Acknowledgments

I would like to thank my supervisors, Jim Barton and Bill MacPherson, for their insight, guidance, and continual support throughout the duration of this work. I have benefited greatly from their friendship, management and constant encouragement, and would appreciate their patience with my “Chinese style English”. I would also like to acknowledge members of the Fibre Optics Group, in particular Robert Maier, Nicolas Gayraud, Amanda Fender, for their wide range of expertise and support throughout this work.

My thanks also go to Henry Bookey and Ajoy Kar for their collaborative support and ideas for this work. I would like to thank Joris Lousteau, Xin Jiang and Animesh Jha from Leeds Uinversity for supplying of the novel glass fibres, Rui Suo and Lin Zhang from Aston University for fabricating the fibre gratings. I also thank the UK EPSRC for the provision of a project studentship. I would also like to thank the staff in the physics department and school for their help and support during my PhD study period.

I would also like to thank all my friends in Edinburgh for sharing living experiences and help in daily life.

Finally, I have to express my gratitude to my families and would like to dedicate this thesis to them: my parents who give me constant support and encouragement; my husband Yongkai, who provided all his love, support and patience for my works over the years; and my son Yunxiang, who gives me small surprises everyday!

Contents

List of Publications

Journals

- H. Li, J. Lousteau, W. N. MacPherson, X. Jiang, H. T. Bookey, J. S. Barton, A. Jha, A. K. Kar. “Thermal sensitivity of tellurite and germinate optical fibers”. *Optics Express*, Vol.15, 8857-8863 (2007).
- R. Suo, J. Lousteau, H. Li, X. Jiang, K. Zhou, L. Zhang, W. N. MacPherson, H. T. Bookey, J. S. Barton, A. K. Kar A. Jha and I. Bennion, “Fiber Bragg gratings inscribed using 800nm femtosecond laser and a phase mask in single and multi-core mid-IR glass fibers”. *Optics Express*, Vol. 17, No. 9, 7540-7548 (2009)
- H. T. Bookey, J. Lousteau, N. Gayraud, R. R. Thomson, N. D. Psaila, H. Li, W. N. MacPherson, J. S. Barton and A. K. Kar, “Multiple rare earth emissions in a multicore tellurite fiber with a single pump wavelength,” *Optics Express*, Vol. 15, No. 26, 17554-17561(2007)

Conference Presentations

- Hongxia Li, Joris Lousteau, Henry T. Bookey, William N. MacPherson, James S. Barton, Ajoy K. Kar, Animesh Jha, “Thermal response of tellurite glass optical fibre”. Poster presentation at the third European Workshop on Optical Fibre Sensors Conference. Naple (Italy). *Proceedings of SPIE*. Vol. 6619, pp. 66190O (2007).
- Hongxia Li, Joris Lousteau, William N. MacPherson, Xin Jiang, Henry T. Bookey, James S. Barton, Animesh Jha, Ajoy K. Kar, “Sensing properties of tellurite and germinate glass fibres”. Oral presentation at Photon08 Conference in Heriot-Watt University. Edinburgh (United Kingdom) 2008.
- Hongxia Li, Joris Lousteau, Rui Suo, Xin Jiang, William N. MacPherson,

Henry T. Bookey, James S. Barton, Ajoy K. Kar , Lin Zhang, Animesh Jha, Ian Bennion, “Sensing properties of germanate and tellurite glass optical fibres”. Submitted to 20th International conference on Optical Fiber Sensors, Edinburgh (United Kingdom) Oct-2009

- H. T. Bookey, H. Li, R. R. Thomson, A. K. Kar, W. N. MacPherson, J. S. Barton, J. Lousteau, C. J. Hill, X. Jiang and A. Jha, “Characterisation of multicoretellurite optical fibre”. CLEO-IQEP Conference 2007. Munich(Germany).*IEEE*.2007-11-21
- H. T. Bookey, R. R. Thomson, A. K. Kar, H. Li, W. N. MacPherson, J. S. Barton, J. Lousteau, C. J. Hill, X. Jiang and A. Jha, “Three-core tellurite fiber with multiple rare earth emission”, CLEO Conference 2008. San Jose, California (USA). *IEEE*.2008-05-04

Chapter 1

Introduction

1.1 Introduction

The work investigated within this thesis is a part of the project: Novel Multicore Optical Fibres for Lasers, Amplifiers and Sensors in the Near and Mid Infrared, which is a collaboration, funded by EPSRC, between Heriot-Watt University, Leeds University and Aston University to investigate multicore fibres in novel germanate and tellurite glasses for operation at near- and mid-infrared wavelengths by exploiting the rare-earth-ion spectroscopic and sensing properties for applications in laser technology and in sensor devices.

Mid-infrared wavelengths are an important region for spectroscopic detection of many substances, and conventional silica fibres become unusable for wavelengths beyond about 2 microns due to severe attenuation inherent in the silica. Tellurite and germanate glass fibres have great potential for use in near and mid infrared (mid-IR) optics, because the different electronic structures in these glasses promise much lower attenuation. The high nonlinearity and its excellent transmission properties in the mid infrared make it an ideal candidate for many linear and nonlinear optical devices, and give the possibility of fibre lasers and fibre sensors in a previously inaccessible part of the spectrum.

The aim of this thesis is to investigate the optical characteristics and sensing properties of novel fibres and to determine their potential applications to physical and gas sensors.

1.2 Optical Fibres

The first research into the guided transmission of light can be traced back to John Tyndall's experiment in 1870, which demonstrated the possibility to confine light propagation along a waveguide structure by the principle of total internal reflection. Around the same time, William Wheeling patented a method of light transfer called ''piping light'' by using mirrored pipes to send the light to many different rooms [1.1]. However optical fibre technology was only extensively developed in the middle of the twentieth century. Early success of light guiding came during the 1950's by introducing a cladding layer of lower refractive index around the glass fibre, which is the base of optical fibre waveguides used today. Early all-glass fibres experienced excessive optical loss of 1000dB/km due to impurties in the glass rather than fundamental physical effects such as scattering. The proposed use of optical fibres for optical communications with losses lower than 20dB/km by Charles Kao and George Hockham [1.2, 1.3] in 1966 led to the work on the problem of purifying glass. The purest glasses, mainly silica, were fabricated by Maurer and Schultz of Corning in 1970 and optical glass fibres with losses of less than 5dB/km were developed [1.4]. Figure 1.1 shows the reduction in the propagation loss of optical radiation through silica glass fibres in recent decades and its four transmission windows [1.5]. Now optical fibres have become a centre of interest as transmission lines for various applications, such as communication links and sensing systems, based on the successful fabrication of low loss silica-based optical fibres whose transmission losses are reduced to as low as 0.2dB/km. The minimum optical loss of silica fibre occurs at 1.55μm and increases rapidly with wavelength due to multiphoton absorption and parasitic OH^- vibrations. However various processes require optical fibres to transmit energy in the infrared region, such as the CO_2 laser at 10.6μm, remote analysis of polychromatic IR radiation, IR emission of black bodies, spectroscopy of gaseous bodies, and sensors.

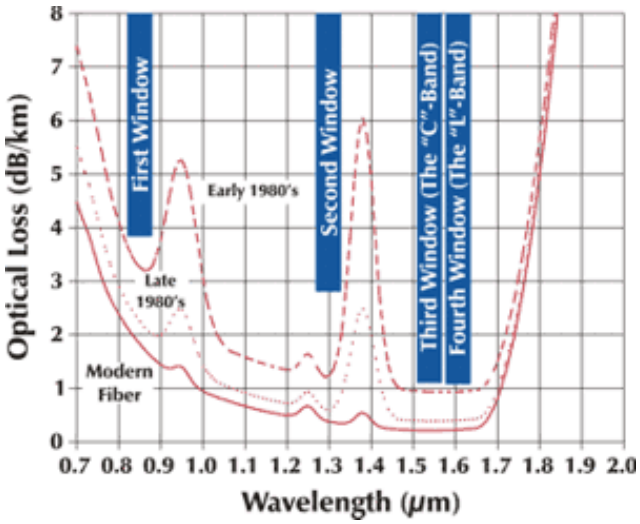

Fig. 1.1 Silica glass fibre transmission loss in recent decade years with its four transmission windows [1.5]

1.2.1 Infrared optical fibres

The possibility of infrared materials with an ultra-low loss less than 0.01dB/km was first discussed by Pinnow, Van Uitert and Goodman etc in 1970's, and these discussions motivated the research efforts on the non-silica-based infrared optical fibres [1.6]. Optical materials studied to date for infrared optical fibres are heavy-metal oxides, halides and chalcogenides. In the heavy-metal oxides, GeO_2-based glasses have been extensively studied by Olshansky and Scherer in 1979 and a low loss reaching below 0.2dB/km was predicted [1.7]. Crystalline halide materials are particularly advantageous for CO_2 laser power transmissions due to their sufficiently lower losses at 10.6μm. Chalcogenides are basically divided into sulphides, selenides and tellurides. Sulphide glass fibres can transmit light of wavelength between 2 to 5μm, while selenide and telluride glass fibres have a wide transparency range which covers around 10μm in wavelength. The discovery of ZrF_4-based fluoride glasses by Poulain in 1975 and subsequent research made it possible to fabricate low loss infrared fibres [1.8]. These fluoride glasses are thought to be the most promising candidates for the ultra-low loss optical fibres in long distance optical communication with predicted loss value less than 0.01dB/km at 2~4 μm wavelengths. On the other hand, hollow core fibres utilizing total

reflections between the hollow cores and dielectric claddings have also been developed which can transmit wavelengths in the IR range of 2~20 μm [1.9].

1.3 Optical Fibre Sensors

A sensor system or sensor is a type of transducer that converts one form of energy into another form of energy, which is usually made up of a transducer device, a communication channel and a subsystem for generating or detecting, treating, processing and conditioning the signal. An optical sensor is a system in which the measurand introduces modifications or modulations in some of the characteristics of light in the optical system, such as amplitude, phase, frequency or polarization. Consequently, if fibre-optic technology is used in any of the processes or parts of the sensor system, it is often known as an optical fibre sensor.

Optical fibre sensors offer many potential advantages over other measurement techniques. The optical fibres with small size are suitable for fabricating small and lightweight sensors which have the potential of high bandwidth measurements. The dielectric medium of optical fibre means it is electrically non-conducting and immune to electromagnetic interference, thus it can be used in noisy electromagnetic environments where it is not possible to use electrical based sensors. Moreover, optical fibre sensors can also be used in potentially dangerous environments such as flammable or explosive environments because they do not radiate electromagnetic waves. As a consequence of the excellent transmission characteristics offered by optical fibres, remote sensing can be carried out using optical fibre to transmit information from a sensing region or element to the optical interrogation system, and a number of sensors can be integrated using multiplexing and appropriate interrogation techniques along a single optical fibre.

Optical fibre sensors also have a number of disadvantages, such as the fragility of the glass fibre which can limit their incorporation into engineering structures, or the potentially increased cost or complexity of the sensor and the optical interrogation system, compared to other measurement techniques. The cross sensitivity of an optical fibre to different measurands is an important limitation because it introduces errors in the output signals; however, this problem also exists for conventional sensors.

1.4 Aim of Thesis

The aim of the work within this thesis is to investigate sensing properties of infrared tellurite and germanate glass fibres. Thermal and strain responses of tellurite and germanate fibres are explored using a fibre Fabry-Perot (FFP) interferometric technique and fibre Bragg gratings (FBGs), and the design of a germanate glass fibre evanescent field gas sensor is investigated and modelled.

1.4.1 Layout of thesis

Chapter 2 gives an overview of suitable information to set out the background of the work reported in this thesis. The fundamental concepts of optical fibres and characteristics of infrared fibres are reviewed, and then the basic information of techniques used to investigate the tellurite and germanate fibre thermal and strain sensing properties are described, followed by the introduction of infrared spectroscopic technique for the chemical species detection and a review of the optical sources in mid-infrared region.

Chapter 3 describes experimental investigations of the chromatic dispersion characteristics and the thermal sensing properties of tellurite and germanate glass fibres. The refractive index and dispersion characteristics are measured using low-coherence interferometry based on dispersive Fourier transform spectroscopy. Then the thermal response of tellurite and germanate fibres are investigated by measuring the phase sensitivity to temperature of a fibre Fabry-Perot cavity, which is formed by splicing these soft glass fibres to a single mode silica fibre using an asymmetric fusion splicing technique. The thermal responses of FBGs in tellurite and germanate fibres are also investigated and compared with the results from FFP interferometer, and contributions from the thermal expansion, thermal optical effects and electronic polarizability are discussed.

Using the fibre Fabry-Perot interferometer and fibre Bragg gratings, the strain sensitivity and Young's modulus of tellurite and germanate glass fibres are explored in chapter 4.

In chapter 5, the design of a tapered germanate glass fibre evanescent field gas sensor is investigated and modelled. The mid-infrared light generation using an optical parametric oscillator is investigated and the power ratio of evanescent wave to total

propagating wave of the tapered fibre is modelled. The sensor performance of detectable gas concentration, minimum detectable gas concentration and resolution with relationship to the gas cell length and fibre attenuation are analysed and modelled.

Finally general conclusions and further work are discussed in chapter 6.

1.5 References

[1.1] Jeff Hecht. *City of Light, the Story of Fiber Optics*. New York, Oxford University Press, 1999

[1.2] K. C. Kao, G. A. Hockham. *Dielectric fiber surface waveguides for optical frequencies*. Proc. IEE, Vol. 113, No. 7, pp. 1151-1158, 1966

[1.3] A. Werts. *Propagation de la lumière cohérente dans les fibres optiques.* L'Onde Electrique, Vol. 46, pp. 967-980, 1966

[1.4] D. Keck. *A future full of light.* IEEE Journal on Selected Topics in Quantum Electronics, Vol. 6, No. 6, pp. 1254-1258, 2000

[1.5] A. A. Huurdeman. *The Worldwide History of Telecommunications*. John Wiley & Sons, Inc., Publication, 2003

[1.6] S. Takahashi, T. Kawashima. *Preparation of low loss multi-component glass fiber*. Tech. Dig. Int. Conf. Integr. Opt. and Opt. Fiber Commun., pp.621, 1977

[1.7] T. Katsuyama, H. Matsumura. *Infrared Optical Fibers*. IOP Publishing Ltd, Adam Hilger, Bristol, UK, 1989

[1.8] S. Mitachi, Y. Ohishi, T. Miyashita. *A fluoride glass optical fiber operating in the Mid-Infrared wavelength range*. Journal of Lightwave Technology, Vol. LT-1, No.1, Mar.1983

[1.9] T. M. Munro, Y. D. West, D. W. Hewak, N. G. R. Broderick, D. J. Richardson. *Chalcogenide holey fibres*. Electronic Letters, Vol.36, pp.1998-2000, 2000

Chapter 2

Literature Review

2.1 Introduction

This chapter gives an overview of conventional and infra-red fibres and application to sensors to set out the background of the work reported in this thesis. First the fundamental concepts of optical fibres and wave theory used for simple description of the light propagating in the optical fibres are introduced; and secondly an introduction of infrared optical fibres and their characteristics are described; then optical fibre sensing techniques are described, in which the Fabry-Perot interferometric and the Bragg grating sensing techniques are reviewed in more details as they were used for the mid-infrared glass fibre thermal and strain sensing property investigations in the work of this thesis in chapter 3 and chapter 4; Infrared spectroscopic techniques for the chemical species detection are also introduced in detail; finally a review of the optical sources in mid-infrared region are reported in detail.

2.2 Optical Fibres

Optical fibres are waveguides that can guide light from one place to another, which are usually made from either of glass, crystal or polymers. The simplest kind of optical fibre typically consists of a step-index structure, which has a core of constant refractive index n_{co}, and a cladding of a slightly lower refractive index n_{cl}. For single-mode optical fibres the core diameter can vary between ~ 2μm to 10μm depending on the operating wavelength of the fibre and refractive indices of the core and cladding; this is to ensure only one propagation mode is supported by the fibre. Comparatively, multimode fibre is manufactured with a core diameter of 50μm, 62.5μm or larger. The

diameter of the outermost cladding layer often has the standard value of 125 μm, which are usually protected by a buffer layer (typically a plastic coating). The buffer, often a polyacrylate material, is typically 250μm in diameter. The core and cladding together form the basic optical system that transmits light, while the buffer primarily protects the cladding surface and inhibits cracks that would lead to brittle failure at handling, and secondly its higher refractive index helps to strip out cladding modes, as shown in figure 2.1(a). Communications cables are usually further protected inside jackets or tubing as shown in figure 2.1(b) [2.1].

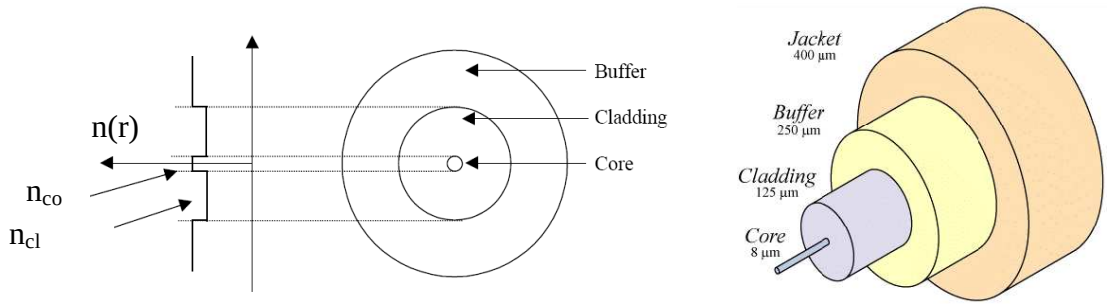

(a) (b)

Figure 2.1: Basic structure of an optical fibre [2.1]

2.2.1 Light propagation in an optical fibre

Light propagating in an optical fibre can be analysed either using geometric optics as a basic approximate model or electromagnetic wave theory which gives a more detailed description of the light propagation.

Typically fibre with large core diameter (great than 10μm), called multimode fibre, may be analyzed by geometric optics. In a step-index multimode fibre, as shown in figure 2.2(a), light is guided through the fibre by total internal reflection. According to the Snell's law, if a ray of light propagating within the core approaches the boundary with the cladding at an angle larger than a critical angle, defined by

$$\phi_c = \sin^{-1}\left(\frac{n_{cl}}{n_{co}}\right) \tag{2.1}$$

it will not pass through the boundary but will be reflected back into the core n_{core}, provided that $n_{co} > n_{cl}$.

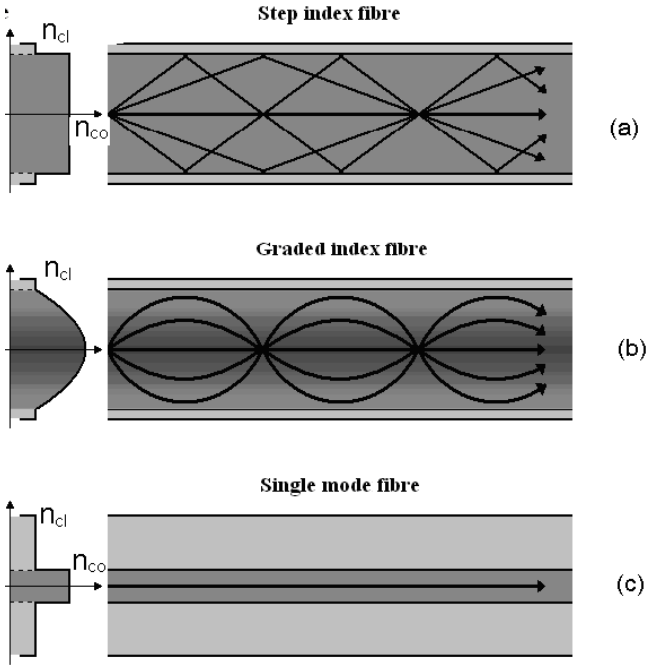

Fig.2.2 Light propagation in multimode step index (a), graded index fibre (b) and single mode fibre (c) [2.2]

If a ray of light meets the boundary at a lower angle than the critical angle, it is refracted from the core into the cladding where it is not useful for confining light along the fibre. Thus Snell's law can be used to find the maximum angle that the incident ray should make with the fibre axis to remain confined inside the core. The minimum angle for total internal reflection determines the acceptance angle of the fibre, typically known as the numerical aperture (NA.) of the fibre, which represents the light-gathering capacity of an optical fibre. For $n_{co} \approx n_{cl}$, the NA. can be approximated by

$$NA = \sqrt{2(n_{co}^2 - n_{cl}^2)} = n_{co}(2\Delta)^{1/2} \tag{2.2}$$

Where

$$\Delta = (n_{co} - n_{cl}) / n_{co} \tag{2.3}$$

is the fractional index change of the core-cladding interface.

It is easier to efficiently couple light into fibre with higher numerical aperture, but a higher numerical aperture also increases the amount of multi-path spreading by allowing light to propagate down the fibre in rays both close to the axis and at various angles, which affects light pulses in the fibre, known as intermodal dispersion.

For graded-index fibre, the refractive index of fibre core decreases with increasing distance from the axis of the core, which causes light rays crossing the core

axis to be progressively refracted back towards the core centre at angles less than the critical angle, as shown in figure 2.2(b). These curved paths reduce the intermodal dispersion because high angle rays pass more through the lower index of the core rather than the higher index centre. This property of graded index fibres is called self-focusing.

Figure 2.2(c) shows the light rays propagate in a singlemode fibre, where the single ray picture is only a simple model where the really ray idea breaks down for this smaller – core structures. Typically a singlemode fibre with a core diameter lower than 10μm is analysed as an electromagnetic structure by solving Maxwell's equations, which gives a more detailed description of the light propagation.

Modal anaylsis for a step-index fibre using wave equation

The use of electromagnetic theory is an alternative approach to understand the light propagation in the fibre, it is governed by Maxwell's equations. Full modal analyses of fibre using the wave equation are described in many references [2.3, 2.4, 2.5, 2.6], and here we will give a summarised description.

For step-index fibre with small difference of the core and cladding refractive index, a scalar wave approximation can be used. In this condition, the spatial variation of the electric field for cylindrical fibre in a polar coordinate system (r,ϕ, z) can be written as:

$$E(r,\phi,z) = E_0(r,\phi)\exp(-j\beta z) \tag{2.4}$$

where β is known as propagation constant. Substituting equation 2.4 into the scalar wave equation

$$\nabla^2 E - \mu\varepsilon\frac{\partial^2 E}{\partial t^2} = 0 \tag{2.5}$$

which is derived from Maxwell's equations. Using the polar Laplacian given by

$$\nabla^2\psi = \frac{\partial^2\psi}{\partial r^2} + \frac{1}{r}\frac{\partial\psi}{\partial r} + \frac{1}{r^2}\frac{\partial^2\psi}{\partial\phi^2} + \frac{\partial^2\psi}{\partial z^2} \tag{2.6}$$

we obtain the following solutions for the electric field inside the fibre core

$$(\frac{\partial^2}{\partial r^2} + r\frac{\partial}{\partial r} + \frac{1}{r^2}\frac{\partial^2}{\partial\phi^2} + U^2\frac{r^2}{a^2})E_z = 0 \qquad 0<r<a \tag{2.7}$$

and the electric field within the cladding

$$(\frac{1}{r^2}\frac{\partial^2}{\partial r^2} + r\frac{\partial}{\partial r} + \frac{1}{r^2}\frac{\partial^2}{\partial\phi^2} - W^2\frac{r^2}{a^2})E_z = 0 \qquad r>a \tag{2.8}$$

where a is the fibre core radius, E_z is the electric field in the core and in the cladding regions of an optical fibre.

Equation 2.7 and 2.8 are of standard form of Bessel's equation, where ordinary Bessel functions J and Y for equation 2.7 describe an oscillatory function in the core and the modified Bessel function K and I for equation 2.8 describe monotonic decay with increasing radius in the cladding known as the evanescent field, as shown in figure 2.3(a,b).

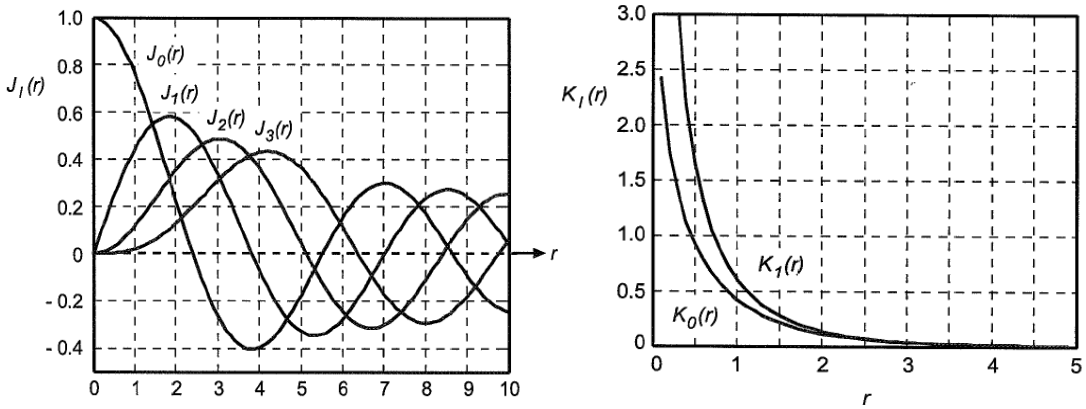

(a) (b)

Fig.2.3 *J* type Bessel function (a) and *K* type Bessel function

From above analysis, we can get the dimensionless transverse propagation constant for the core U as

$$U = a(k^2 n_{co}^2 - \beta^2)^{1/2} \tag{2.9}$$

and the dimensionless attenuation constant W for the cladding

$$W = a(\beta^2 - k^2 n_{cl}^2)^{1/2} \tag{2.10}$$

where $k = \omega\sqrt{\mu\varepsilon}$, ω is the optical frequency, and β is the propagation constant.

From equation (2.9) and (2.10), the important dimensionless normalized waveguide parameter V is given by

$$V = (U^2 + W^2)^{1/2} = k_0 a(n_{co}^2 - n_{cl}^2)^{1/2} = \frac{2\pi}{\lambda} a(n_{co}^2 - n_{cl}^2)^{1/2} \tag{2.11}$$

The normalized waveguide parameter V, often called the V-number, is widely used to describe general mode propagation properties in a fibre and depends on the fibre's core radius, fibre core and cladding refractive indices and the wavelength.

In a standard step-index fibre, the number of modes guided by the fibre is determined by the V-number. For a fibre to support a singlemode at a wavelength λ, V should satisfy $V(\lambda)<2.405$. If the V-number exceeds the limit for singlemode operation, higher order modes start to propagate and the fibre is known to be multimode, and the approximate number of modes N is given by

$$N = V^2/2 \tag{2.12}$$

The V-number defines a wavelength limit, called the cut-off wavelength, which determines a fibre supporting a singlemode or multimode.

Fractional power in the core

The fractional power carried in the core is one of the important parameters associated with an optical fibre. The fractional power propagating in the core is given by [2.3]

$$\eta = \frac{P_{core}}{P_{tot}} = [\frac{W^2}{V^2} + \frac{U^2}{V^2}\frac{K_l^2(W)}{K_{l+1}(W)K_{l-1}(W)}] \tag{2.13}$$

in which $K_l(W)$ is the modified Bessel function of l^{th} order.

For a single mode fibre, the fundamental mode field distribution can be well approximated by a Gaussian function which can be written as

$$\psi(r) = A\exp(-r^2/w^2) \tag{2.14}$$

where w is the spot size of the mode field pattern. The quantity $d=2w$ is usually referred to as the mode field diameter (MFD). For a step index fibre single mode fibre, the spot size can be calculated from the following empirical expression, which gives a value of w to within about 1% [2.3]

$$\frac{w}{a} \approx 0.65 + \frac{1.619}{V^{3/2}} + \frac{2.879}{V^6} \qquad 0.8 \le V \le 2.5 \tag{2.15}$$

where a is the core radius. The fraction of power confined in the core of single mode fibre is given by the following confinement factor

$$\Gamma = 1 - \exp(-\frac{2a^2}{w^2}) \tag{2.16}$$

Using equation (2.15) and (2.16), it can be seen that the mode power carried in the core of a singlemode fibre drops as the V-number decreases and the remaining fraction propagates into the cladding as an evanescent field, which can be used for evanescent

field sensing applications. An analysis of evanescent field gas sensing devices using tapered fibre is described in chapter 5.

2.2.2 Optical fibre properties

Attenuation

Attenuation represents one of the most important characteristics of an optical fibre. The two physical processes that cause attenuation are absorption and scattering.

Absorption loss is caused by interaction of the propagating lightwave with one or more major components that constitute the fibre's material composition, which is known as intrinsic absorption, or extrinsic absorption caused by the presence of minute quantities of materials such as transition metal ions and OH^- ions dissolved in glass. Various technologies, such as vapour-phase axial deposition (VAD) technique to reduce the residual OH^- content in fibre material, have been developed for fabrication of extremely low loss optical fibres.

Rayleigh scattering is responsible for the scattering loss and is a fundamental mechanism that is caused by small scale inhomogeneities that are frozen into the fibre. These inhomogeneties are produced during the fabrication of the fibre and result in composition and density fluctuations. The loss due to Rayleigh scattering is proportional to $1/\lambda^4$ and obviously decreases rapidly with increase in wavelength. Thus the Rayleigh scattering loss is extremely small for infrared fibres (λ_0>2μm) which is described in following section 2.3. Scattering losses may also be caused by fibre bending or imperfections in the fibre such as core-cladding irregularities, or diameter fluctuations.

The attenuation of an optical beam is usually measured in decibels (dB). If an input power P_1 results in an output power P_2, then the loss in decibels is given by

$$\alpha = 10\log_{10}\frac{P_1}{P_2} \tag{2.17}$$

For example, if the output power is half the input power, then the loss is about 3dB.

Dispersion

Pulse dispersion represents one of the most important characteristics of an optical fibre that determines the information-carrying capacity of a fibre optic communication system.

Dispersion can generally be categorised into four groups: material, waveguide, intermodal, and polarisation mode dispersion.

In multimode step-index fibres, the primary cause of dispersion is the fact that the modes follow different paths down the fibre and so take different lengths of time to reach the end; this is called intermodal dispersion. Intermodal dispersion is of particular importance for multi-mode fibres and describes the propagation variation between a discrete number of modes supported by the fibre; however this is negligible for single-mode fibre.

In singlemode fibre there are two types of significant dispersion, material and waveguide dispersion. Material dispersion describes the interaction of the propagating fields with the bulk material through which they are travelling. The refractive index of the optical fibre material is not a constant, and is dependent on the transmission light wavelength. As no source is perfectly monochromatic, when it propagates through an optical fibre, the transmission velocity varies with the light wavelength due to the frequency dependence of the refractive index of the medium, which gives rise to material dispersion. When the optical fields propagate within a waveguide, the profile of the modes and the refractive index variation across the mode profile (due to refractive index difference between the core and cladding) modifies the material dispersion and this is known as waveguide dispersion. Finally, polarisation mode dispersion describes the propagation variation with respect to the polarisation state of the optical field. In general the optical field is decomposed into two orthogonal polarisation eigenmodes and the polarisation mode dispersion describes the variation between these modes due to anisotropies within the fibre which affect each mode differently.

Material dispersion and waveguide dispersion are also called chromatic dispersion because the broadening occurs within the transmitted mode. The velocity of the propagating waves is important for the understanding of chromatic dispersion. In practice no source is perfectly monochromatic, thus a more important quantity is the group velocity v_g which describes the velocity of the group of waves with similar frequencies called wave-packet. The group velocity is defined as

$$v_g = \frac{d\omega}{dk} \tag{2.18}$$

The pulse spread from chromatic dispersion is usually obtained by considering the group delay τ_g in the fibre, which describes the transit time of the wave-packet through the fibre and is given by the reciprocal of the group velocity, defined as

$$\tau_g = L\frac{d\beta}{d\omega} = \frac{L}{c}\frac{d\beta}{dk} \tag{2.19}$$

where L is the length of fibre. The chromatic (or first order) dispersion per unit length of a single-mode fibre can be obtained by derivation of the group delay τ_g with wavelength λ, which is described in more detail in chapter 3.

2.3 Infrared Optical Fibres

Infrared (IR) optical fibres have attracted a great deal of attention both in fundamental research and also in optical devices due to their low loss transmission characteristics in the mid to far infrared wavelength regions from 2 to approximately 20μm.

The first IR fibres were fabricated from chalcogenide glasses in the 1965 by means of a double crucible method. They were restricted to the application of short length light transmission such as image guiding and infrared remote sensing due to transmission losses in excess of 10dB/m from 2 to 8μm [2.7]. During the mid-1970s, there was interest in developing an efficient and reliable IR fibre to link broadband, long wavelength radiation to remote photodetectors in military sensor applications and an increasing need for a flexible fibre delivery system for transmitting CO_2 laser radiation in surgical applications. Based on these requirements, various infrared transmitting materials and fibres were developed, and the possibilities of ultra-low loss infrared optical materials less than 10^{-5} dB/m were indicated by Pinnow *et al*. [2.8] in 1978. Typically infrared transmitting materials have small force constants and large masses of constituent atoms therefore they are relatively soft and usually contain heavy metals. These infrared optical materials include heavy-metal oxides, halides and chalcogenides.

Based on these infrared optical materials, various infrared optical fibres have been proposed and fabricated to date. In principle, infrared optical fibres can be divided into three broad categories: glass, crystalline, and hollow waveguides. These categories may be further subdivided based on the fibre material or structure, as shown in table 2.1.

An excellent review of the types of IR fibres can be found in a book by Harrington [2.9] and in some papers [2.10, 2.11, 2.12, 2.13].

Table 2.1 Classification of infrared optical fibres with typical examples

Main	Subcategory	Typical examples
Glass fibre	Oxide glass fibre	GeO_2 and TeO_2 based glass fibres
	Fluoride glass fibre	ZBLAN-(ZrF_4-BaF_2-LaF_3-AlF_3-NaF)
	Chalcogenide glass fibre	As_2S_3 and AsGeTeSe
Crystalline fibre	Polycrystalline fibre	AgBrCl
	Single crystalline fibre	Sapphire
Hollow waveguide	Metallic/dielectric hollow waveguide	Hollow glass waveguide
	Refractive index<1	Hollow sapphire at 10.6μm

For the work in this thesis, the GeO_2 and TeO_2 based glass fibre characteristics and their sensing properties are investigated, therefore more detail of the infrared oxide glass fibres are described in the following section 2.3.1.

2.3.1 Oxide glass fibres

Heavy metal oxide glass fibres such as tellurite or germanate based oxide glass fibres have been proposed and investigated as good candidates for ultra-low loss optical fibres in the mid-infrared regions. The advantage of heavy-metal glasses such as GeO_2 or TeO_2 glass is that their constituent metals are heavier than Si in SiO_2 glass, infrared absorption due to lattice vibration (Ge-O) can be shifted towards a longer wavelength. This leads to the ultra-low loss in the infrared region. The heavy-metal oxide glasses proposed for infrared optical fibres can be divided into GeO_2 based and TeO_2 based glasses. Typically these germanate or tellurite based glasses have a strong absorption in 3-3.5μm region because of the presence of the hydroxyl ion-OH^- as an impurity, which also contributes to significantly high absorption loss at 3.8μm combined with CO_2

impurity [2.14]. Consequently some purification methods have been developed to eliminate OH^- and CO_2 impurity[2.15]. The transmission properties of the purified GeO_2 and TeO_2 based glasses are shown in figure 2.4 [2.16] and figure 2.5 [2.17], respectively. It can be seen from the figures that the intrinsic absorptions due to lattice vibrations are shifted to the wavelengths above 5μm. Physical properties of GeO_2 and TeO_2 based glasses reported in the literature [2.18～2.28] compared with SiO_2 glass are shown in table 2.2.

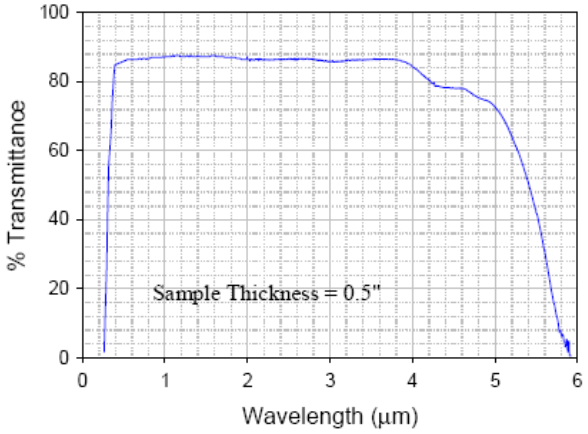

Fig.2.4 Typical vis-IR transmission spectrum of a 0.5'' thick BGG ($BaO-Ga_2O_3-GeO_2$) glass [2.16]

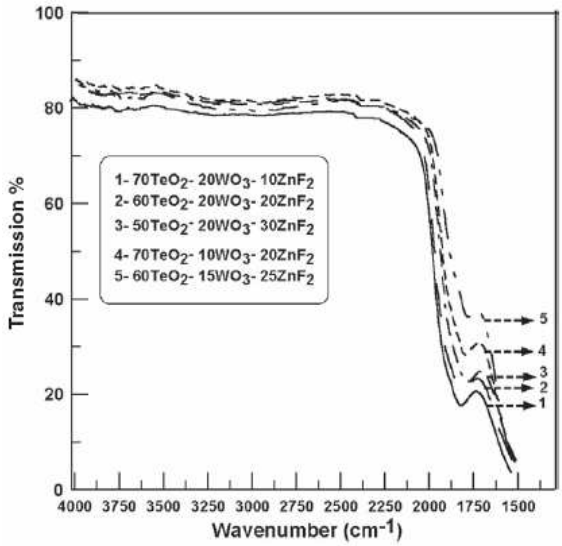

Fig.2.5 Vis-IR transmission spectrum of glasses in the series of the system $TeO_2-Wo_3-ZnF_2$ with 1mm thickness [2.17]

As shown in figure 2.4 and 2.5, low loss transmission characteristic in the mid-infrared region of GeO_2 and TeO_2 based glasses offers the potential to develop new sensing devices such as chemical sensors to detect liquid and gaseous species or for the temperature and strain measurement either as interferometric elements or as fibre gratings. Therefore the sensing properties of these types of glass fibres and their potential to be chemical sensors are mainly investigated in this thesis. For this purpose, different optical fibre sensing techniques are described in detail in the following section 2.4 correspondingly.

Table 2.2 Physical properties of GeO_2 and TeO_2 based glasses compared with SiO_2 glass

Parameters		GeO_2-based glass	TeO_2 -based glass	SiO_2 glass
Density (g/cm^3)		~4.8		2.21 [2.25]
Hardness(kg/mm^2)		~420		461 [2.18]
Melting temperature(K)		~750	~590 [2.19]	~1470 [2.18]
Refractive index		~1.8	~2 [2.19]	1.44 [2.18]
dn/dT (K^{-1})		$\sim 8\times10^{-6}$ [2.16]	$\sim -23.3\times10^{-6}$ [2.21, 2.22]	$\sim 11.6\times10^{-6}$ [2.25]
Thermal expansion		$\sim 10\times10^{-6}$ [2.19]	$\sim 18.6\times10^{-6}$ [2.19]	$\sim 0.55\times10^{-6}$ [2.25]
Elastic modulus (GPa)		63.6 [2.16]	37.15 [2.23]	72.4 [2.26, 2.27]
Poisson's ratio		0.282 [2.20]	0.233 [2.24]	0.17 [2.28]
Strain-optic coefficient	p_{11}	0.225 [2.20]	0.0074 [2.24]	0.113 [2.28]
	p_{12}	0.235 [2.20]	0.187 [2.24]	0.252 [2.28]

Table 2.2 shows that the refractive indices of GeO_2 or TeO_2 based glasses are larger than that of SiO_2 glass, which offers potential of these type of glass fibres for stimulated Brillouin amplifiers since the Brillouin scattering coefficient is proportional to the material refractive index raised to the power of 7 [2.29]. On the other hand, the cross sections of the Raman scattering for the GeO_2 glass is about one order of magnitude larger than that of SiO_2 glass [2.8], therefore GeO_2 glass fibres have potential for applications of nonlinear optical devices such as Raman amplification which can be used as wavelength tunable lasers. In addition, TeO_2 based glasses can also be used to fabricate optical amplifiers and lasers, because they are capable of incorporating large concentrations of rare-earth ions [2.30] with their relatively low phonon energy ($780cm^{-1}$) compared with other oxide glasses such as silica/silicates (1050-1100 cm^{-1})

hosts. Recently, a tellurite glass based triple core fibre structure doped with rare earth ion has been developed to generate large bandwidth of fluorescence or amplified spontaneous emission in the 1500~2050 nm region pumped with a single 980 nm source [2.31]. More over, the fabrication of a three core TeO_2 based glass fibre where each of the cores has a different rare earth doping has been developed, which is also of great interest for the development of multi-band fiber amplifiers and lasers [2.32].

GeO_2 and TeO_2 based glass fibre fabrication

Typically GeO_2 and TeO_2 based glass fibres can be fabricated by a VAD-vapour-phase axial deposition process [2.8], which is one of the most reliable processes for the fabrication of highly pure silica glass fibres because of its excellent controllability and growth rate, or a conventional crucible technique [2.33]. Recently the extrusion process has been applied to infrared transmitting glasses to produce core/clad optical fibre preforms [2.34] and also been used to manufacture photonic crystal fibre preforms [2.35]. The tellurite or germanate glass fibres investigated within this thesis are manufactured by conventional rotational casting in combination with stretching via extrusion process by colleagues in Leeds University, and are described in detail in reference [2.36].

2.4 Optical Fibre Sensing Techniques

Optical fibre sensors are essentially a means whereby light guided within an optical fibre can be modified in response to an external physical, chemical, biological, biomedical or similar influence. The potential advantages of optical fibre sensors come from the fact that the modulated signal can be transmitted to and from the sensing region without recourse to electrical connection due to their sensor material, principle and signal processing. This gives the following principal features:

1. High sensitivity, spatial resolution, and dynamic range;
2. Small size and low weight because of the fibre optic transmission medium, which make them suitable in aerospace applications;
3. Ability to address measurement problems which are inaccessible using alternative technologies, such as the measurement of chemical constituents in the blood of patients undergoing surgical treatment;

4. Ability to monitor parameters in harsh environments such as temperature or pressure in very high intensity radiofrequency fields or explosive environments;
5. Immunity from electromagnetic interference which can limit electrical sensor performance, such as current and voltage in very high electromagnetic interference environments.

According to the interaction type of the physical quantity being measured with the optical fibre sensors, fibre sensors typically can be categorised into two groups as extrinsic and intrinsic sensors. Extrinsic sensors are those in which the fibre is only used to transport the light and an external measurement volume is used to interact with the interested measurand, while intrinsic sensors are defined as those in which the measurand, such as strain or temperature, affects some optical property of the fibre itself resulting in modulation of a characteristic of the propagating light, such as intensity, phase, spectrum or polarisation.

The measurand can be any physical or chemical influence and the range of optical fibre sensors that have been demonstrated is extremely diverse, such as pressure [2.37, 2.38], strain [2.39], temperature [2.40], chemical composition and electric or magnetic field, as well as some medical applications. The characteristics of the light travelling through the fibre that may be used in a fibre sensor include phase, amplitude, modal dispersion, wavelength and polarisation. Depending on the transduction mechanisms which can be exploited, optical fibre sensors also can be categorised into the following groups: intensity measurement, spectral measurement, polarimetric measurement and phase measurement using interferometry. The simplest form of the intensity modulation sensors are based on the modulation of light intensity within the fibre, and multimode fibres are acceptable for most intensiometric sensors in which the phase and the polarisation of the light carries no meaningful information. The problem is that any change of intensity is interpreted as a measurement such as source power fluctuations, bend losses; while the interferometry or wavelength encoded approaches are less sensitivie to this effect. Fibre interferometers use a measurand – induced phase change for detection; singlemode fibre is more suitable for interferometers in which the propagating light phase carries the information related to the measurand. Polarisation based sensors use birefringence as a means of detection.

A number of reviews of optical fibre sensors have been introduced in the literature [2.41, 2.42] and also covered extensively in several books [2.43, 2.44, 2.45].

Related to the work in this thesis, a multiple beam interferometric sensing techniques defined as Fabry-Perot interferometry and a spectral sensing technique using fibre Bragg gratings are used to investigate the thermal and strain sensing properties of tellurite and germanate glass fibres, and an evanescent field sensing technique based on different fibre shapes is also investigated in the modelling for gas species detection. The following sections will describe their sensing mechanism and applications for thermal, strain and gas species measurement in detail.

2.4.1 Interferometric sensing techniques

Interferometry is a technique that makes high precision optical measurements by measuring the change in interference of two or more light beams where one of the beams has been perturbed by the measurand, and includes Fabry-Perot, Michelson, Mach Zehnder and Sagnac interferometers. These interferometric sensing techniques have been demonstrated for the measurement of temperature, strain, displacement and pressure etc in references [2.42, 2.46, 2.47, 2.48, 2.49]. For all of these measurands, the transduction mechanism relies on measuring changes in the optical path difference or in the phase of the interferometer, which result from a mechanical length change or a change in the refractive index of the light guiding medium caused by the strain or temperature. The advantage of optical fibre based interferometers is that they can be constructed directly from the fibre itself so as to measure small phase changes in light transmitted through the measuring region with a precision in the order of wavelength of light, and the optical fibre equivalents of these interferometric configurations are shown in figure 2.6(a,b,c,d). Optical fibre interferometers can also be intrinsic or extrinsic depending on whether the change in the optical path length is within the fibre or not.

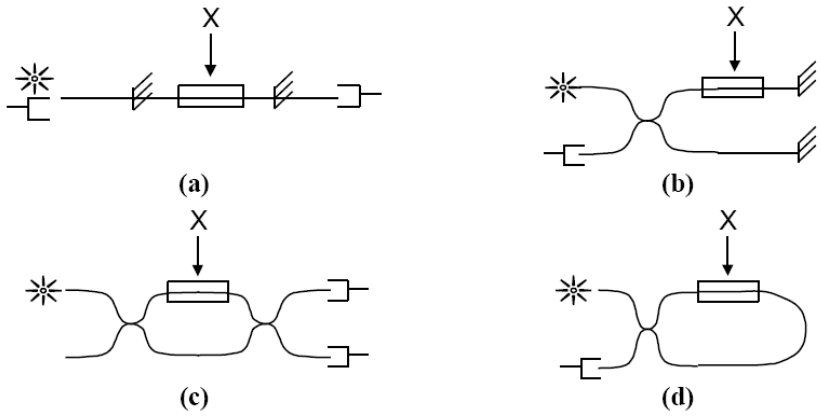

Figure 2.6 : Schematic of optical fibre (a) Fabry-Perot, (b) Michelson, (c) Mach-Zehnder, and (d) Sagnac interferometers with an applied perturbation X [2.110]

Since there are a number of effects which can affect the optical path length in the interferometers, for example both arms of Michelson interferometer are sensitive to environmental conditions such as temperature over their entire length, great care should always be taken to reduce or to compensate for these unwanted changes. Among these sensing techniques, Fabry-Perot interferometers are one of the simplest interferometers to fabricate due to its simple structure, high stability, small size and ease of being embedded into structural materials, which also offer the advantages of very low downlead sensitivity because the reference and signal beams pass through the same fibre to and from the sensor.

FFP (Fibre Fabry-Perot) interferometer

Typically fibre Fabry-Perot interferometers can also be intrinsic or extrinsic depending on whether the change induced by the measurand is in the fibre or not. The extrinsic Fabry-Perot interferometer may consist of two fibres inserted into an alignment tube and one fibre, usually single mode, carries the light to and from the interferometer while the second fibre simply acts as a reflector; the air gap between these two fibres forms the FP etalon and the changes in the gap due to the measurand affects the interferometric signal being detected, as shown in figure 2.7.

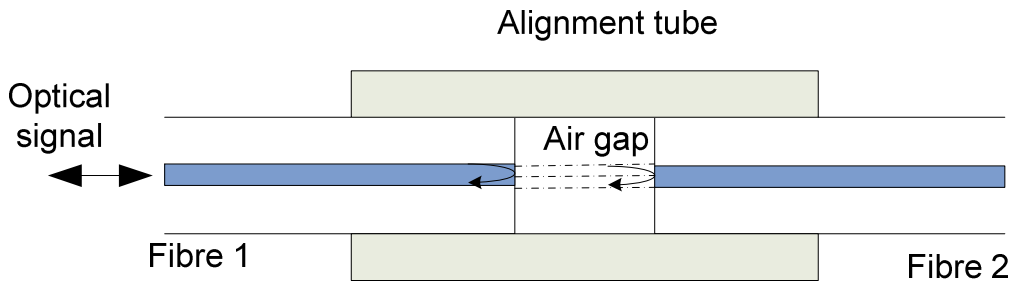

Figure 2.7 Schematic of extrinsic fibre Fabry-Perot interferometer

This extrinsic FFP interferometer typically uses an alignment tube for mechanical alignment and stability which is not suitable for applications where the sensor is to be embedded into structural material due to the outside alignment tube diameter, and the cavity length is also limited due to the coupling losses of the divergent light within the cavity.

Intrinsic FFP interferometers can be fabricated by defining in-fibre mirrors, such as forming a Fabry Perot cavity on the end of a fibre by splicing two fibres with different refractive index, as shown in figure 2.8. The earliest Intrinsic FFP interferometric sensor probably is the spliced TiO_2 thin film coated fiber Fabry-Perot interferometry sensor [2.50], and several other methods are also used to produce internal mirror, such as using vacuum deposition, magnetron sputtering, or e-beam evaporation [2.51, 2.52]. Because the cavity is defined within the fibre then the cavity length can be increased without the loss increasing. Its small size is also suitable for the embedded sensing applications.

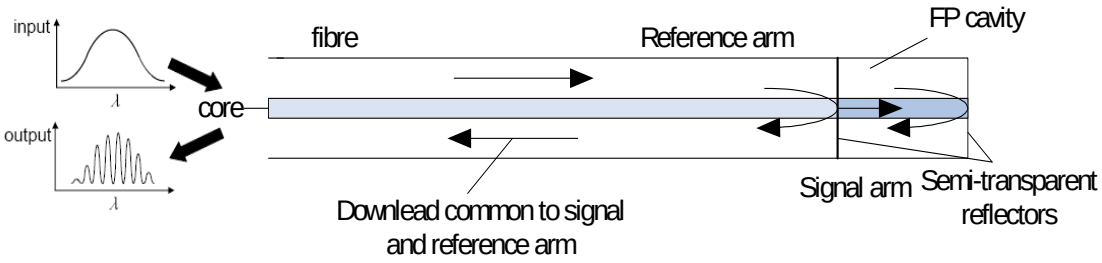

Fig.2.8 Schematic of intrinsic fibre Fabry-Perot interferometer on fibre end face

The incident light propagated in the fibre core is partly reflected at the first semi-transparent reflector which maybe a mirror between two fibres or an interface of two fibres with different refractive index. The transmitted light propagates in second fibre core and is again partly reflected at the second semi-transparent reflector which is typically the cleaved end face of second fibre. The reflected light signal from these two reflectors transmits in the same fibre and is guided into a detector. These two reflected beams are coherent with each other within the coherence length, which depends on the optical source and Fabry-Perot cavity length, to produce a fringe pattern in the light spectrum due to the optical path length difference, as shown in figure 2.8. The reflectivity is weak between different fibre-fibre interface and fibre-air interface which depends on the Fresnel equation, typically the reflectivity between two difference fibres interface is about 10% and about 2～3% between the fibre-air interface. The more detailed calculations for tellurite and germanate glass fibre Fabry-Perot will be given in Section 3.2.1 in Chapter 3. The interference fringe can be written as:

$$R = R_1 + R_2 + 2\sqrt{R_1 R_2}\cos\varphi \tag{2.20}$$

where R_1 and R_2 are the reflectivity of two semi-transparent reflectors, and φ is the phase difference related to the optical path length difference L between two reflected beams, which is given as:

$$\varphi = \frac{2\pi}{\lambda}\cdot n \cdot 2l = \frac{2\pi}{\lambda}\cdot nL \tag{2.21}$$

where l is the Fabry-Perot cavity length and n is the refractive index of the second fibre which forms the FFP cavity, nL is the optical path length difference between two reflected beams.

The FFP interferometer phase difference depends on the change in the optical path length of two reflected beams which is a result of a mechanical length change or a change in the refractive index of the light guiding medium. Typically, the refractive index of the guiding fibre is a function of temperature and strain which is known as the thermo-optic effect and the strain-optic effect respectively. Therefore the FFP interferometer phase difference is sensitive to the external parameters such as temperature, strain and pressure, and it can be made for variety of applications such as temperature or strain sensing elements.

Using equation (2.21), the FFP interferometer optical phase sensitivity to temperature and strain can be described by:

$$\frac{\partial \varphi}{\partial T} = \frac{2\pi}{\lambda}(n\frac{\partial L}{\partial T} + L\frac{\partial n}{\partial T})$$
$$\frac{\partial \varphi}{\partial \varepsilon} = \frac{2\pi}{\lambda}(n\frac{\partial L}{\partial \varepsilon} + L\frac{\partial n}{\partial \varepsilon}) \quad (2.22)$$

Here the discrimination between temperature induced phase shift and strain induced phase shift of FFP interferometer should be taken into account due to the cross-sensitivity, which refers to the unwanted sensitivity of a sensor to other parameters when it is intended to measure another parameter.

FFP interferometer sensor has advantages of simple structure, easy fabrication, small measurement volumes, the inherently high sensitivity associated with interferometric measurements and capability of high bandwidth measurements. For the work in this thesis, fibre Fabry-Perot interferometers formed by splicing mid-infrared glass fibres to a silica fibre downlead are used to investigate the thermal and strain response properties of tellurite or germanate glass fibres, and more details are described in chapter 3 and chapter 4.

2.4.2 Fibre Bragg grating sensor

A fibre Bragg grating sensor is a spectral sensor whose operating principle is based on modulation of the transmitted or reflected spectrum due to the effect from the measurand of interest.

Fabrication

The optical fibre Bragg grating was first fabricated by K. O. Hill et al in 1978, who discovered the photosensitivity in germanium doped silica fibre [2.53, 2.54] and found that the fibre refractive index will increase proportional to the square of the power when it is illuminated by ultraviolet (UV) light. A variety of optical configurations have been developed for grating fabrication as described in references [2.55, 2.56]. The most common techniques for generating the periodic spatial pattern of UV light generally fall into two main categories: the bulk optic interferometric configuration and the phase mask technique [2.57].

An interferometric setup which is used to generate a permanent modification of the refractive index of the fibre core is shown in figure 2.9. The expanded UV laser beam is split into two equal intensity beams and then are recombined via two mirrors to

generate a series of interference fringes. The fibre is placed within the periodic fringe pattern which results in a periodic refractive index profile.

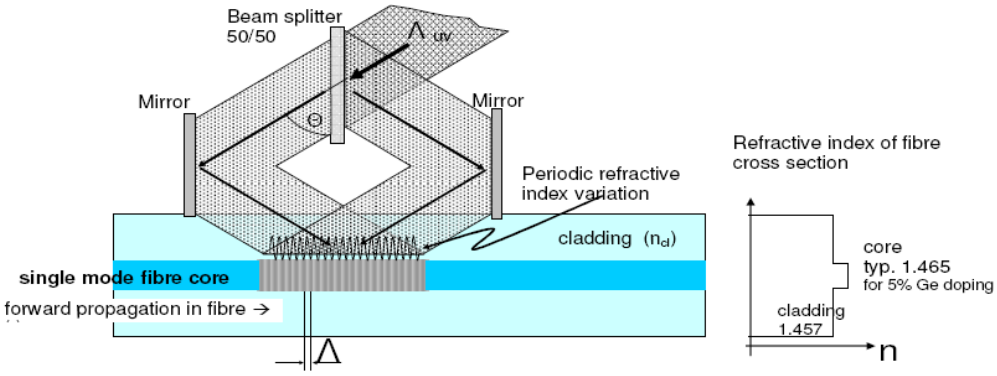

Fig.2.9 Interferometric technique for the Fibre Bragg grating writing [2.58]

Another technique for the fibre Bragg grating generation uses a phase mask. A phase mask is a diffractive optical element that can be used to form the required interference pattern, which is typically manufactured in fused silica with a square stepped profile with a particular spacing, as shown in figure 2.10. A significant advantage of the phase mask technique is that the Bragg wavelength only depends on the pitch of the phase mask and is independent of the laser wavelength. This single beam optical configuration is simpler and thus more stable than the interferometric scheme.

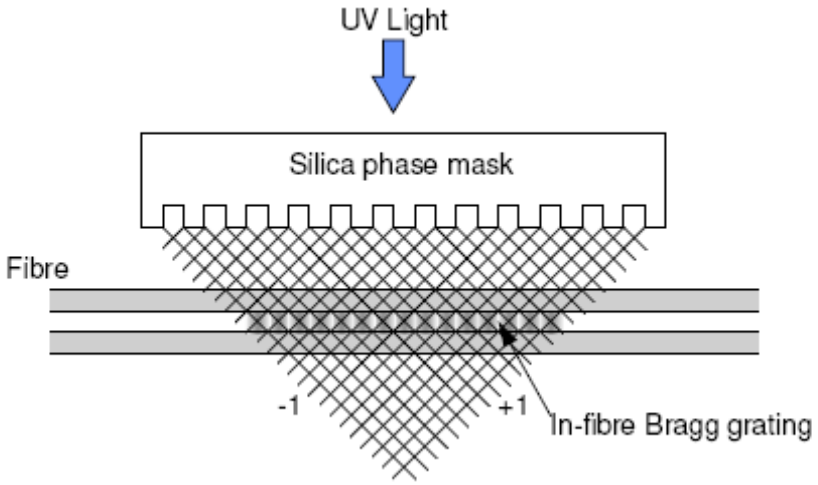

Fig.2.10 Phase mask technology for fibre Bragg grating writing using a UV laser [2.58]

The gratings used for the work in this thesis were fabricated in the tellurite and germanate glass fibres using *fs*-inscription through a custom-designed phase mask with a period of 1697.33nm at Aston University, Birmingham, UK, as shown in figure 2.11. Due to the high refractive indices of the tellurite and germanate glass fibers, the phase mask was chosen to inscribe 2nd order FBGs, grating period is around 424.33nm and 2nd order FBGs wavelength is calculated around 1500-1800 nm using equation $\lambda_B=2n_{eff}\Lambda$. The 800 nm *fs* laser power was from an amplified Ti:seapphire system with a repetition rate of 1 kHz and a maximum output energy of ~13 μJ per pulse. Using this technology, the 2nd order FBG resonances with transmission loss up to ~14dB have been achieved which were used to investigate the thermal and strain responses of these mid-IR glass fibres in the work of this thesis. More details of the germanate single core and tellurite multicore fibre (TZN-MCF) Bragg grating fabrication using *fs* laser and phase mask techniques are described in reference [2.59].

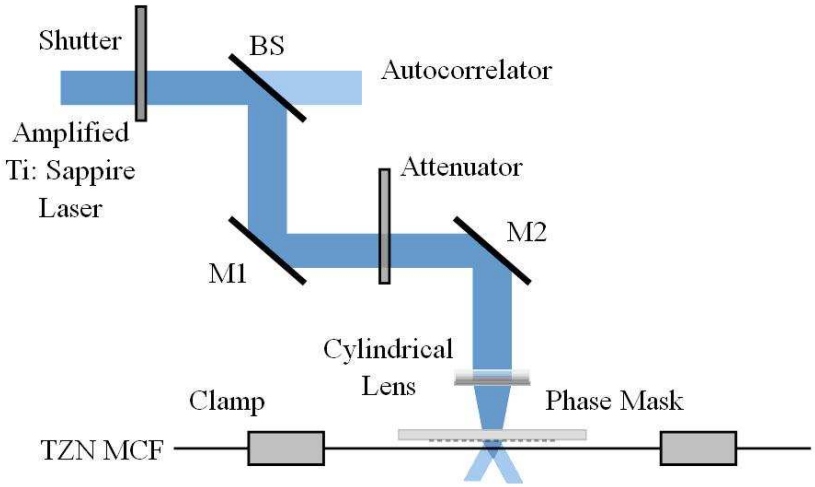

Fig. 2.11 Schematic diagram of FBG inscription system using *fs* laser and phase mask [2.59]

FBG sensor - principle

A fibre Bragg grating is a device with a periodic variation of the refractive index along the fibre axis, as shown in figure 2.12. This grating structure acts as a Bragg reflector that couples light from forward propagating core modes to backward propagating core modes over a narrow wavelength range centred at the Bragg

wavelength λ_B at which the incident light is reflected with maximum efficiency. The Bragg wavelength λ_B is a function of the spatial period of the index modulation Λ and the effective core refractive index n_{eff} of fibre mode in grating section, which satisfies with equation

$$\lambda_B = 2n_{eff}\Lambda \tag{2.23}$$

in which Λ is the period of index modulation, n_{eff} is the effective core refractive index which is approximately given by $n_{eff} = (n_{core} + n_{\mathrm{mod}\,ulatedcore})/2$, and typically the core refractive index modulation depth δn with order of 10^{-3} magnitude.

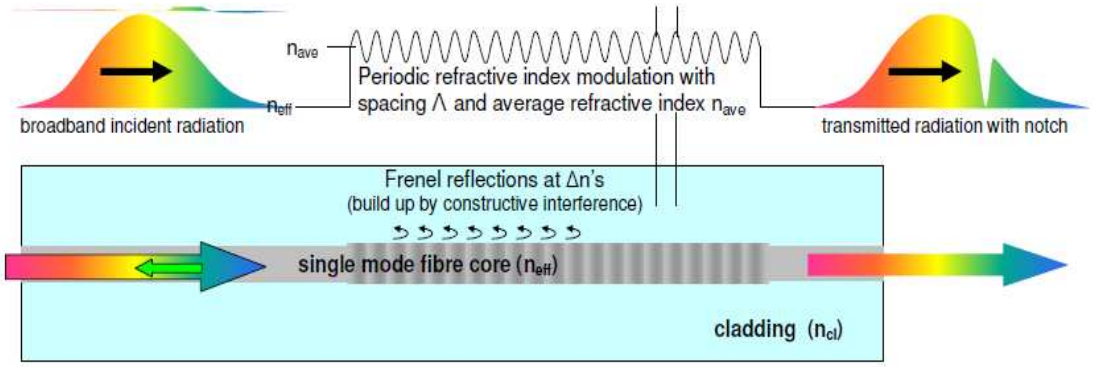

Fig.2.12 Principle of fibre Bragg grating [2.58]

According to equation (2.23), the centre wavelength of the spectrum returned from the grating depends on the the effective core refractive index and the period of index modulation. Both of these parameters can be modified by a number of measurands such as temperature, strain, or pressure, so optical fibre Bragg gratings have been developed as sensors for many applications such as aerospace, civil, marine and medical applications. The work in this thesis investigates the thermal and strain response properties of mid-infrared glass fibres using the fibre Bragg gratings, therefore only the grating response to temperature and strain are described in this thesis.

When the measurand is applied uniformly along the grating, its effect can be observed by measuring the Bragg wavelength change, which can be easily derived from equation (2.23) where the effective core refractive index and the index modulation period are dependent on the temperature T and strain $\varepsilon = \Delta L/L$ and are given as follows:

$$\Delta\lambda_B = 2(n_{eff}\frac{\partial\Lambda}{\partial T} + \Lambda\frac{\partial n_{eff}}{\partial T})\cdot\Delta T \tag{2.24}$$

$$\Delta\lambda_B = 2(n_{eff}\frac{\partial\Lambda}{\partial \varepsilon} + \Lambda\frac{\partial n_{eff}}{\partial \varepsilon})\cdot\Delta \varepsilon \tag{2.25}$$

The first term in equation (2.24) describes the contribution to the wavelength shift due to the thermal expansion to the grating period, and the second term describes the thermal sensitivity of grating wavelength due to the thermo-optic coefficient. The strain sensitivity of the Bragg wavelength in equation (2.25) consists of contributions from the physical change of grating period and from the change in the refractive index due to strain-optic effect. For a fused silica fibre, the wavelength normalized temperature and strain sensitivities are typically $8.883\times10^{-6}/^{o}$C and $0.798\times10^{-6}/\mu\varepsilon$ respectively at 1.55μm [2.60], which is equivalent to wavelength sensitivities of 13.8pm/^{o}C and 1.24pm/με respectively. Hence any measurand that induces temperature or strain in the fibre can be detected by measuring the grating wavelength shift of the reflected or transmitted spectra. Several techniques are developed for the wavelength shift monitoring, such as measuring the grating wavelength using a tuneable source [2.61], using an optical spectrum analyzer or a spectrometer to obtain the optical spectrum of the FBG signal [2.62, 2.63, 2.64], or broadband interferometric detection [2.65] and measurement with a wavelength dependent filter [2.66] where a broadband source is used. Here the discrimination between temperature induced and strain induced grating wavelength shift of fibre Bragg grating should be taken into account due to the cross-sensitivity.

For applications of optical fibre Bragg gratings in communication and sensing, it is important to know the strain and temperature coefficients accurately, therefore the thermal and strain responses of mid-infrared glass- tellurite and germanate glass fibre Bragg gratings are investigated and described in detail in this thesis work.

2.4.3 Optical fibre gas sensing techniques

The requirement for detecting flammable, explosive and hazardous gas species and concentration is becoming important for environmental, industrial, medical and safety reasons. Several gas detection techniques are well developed, such as dyes which change colour after exposure to gases such as hydrogen sulphide and carbon monoxide [2.67]; electrochemically active materials, such as tin oxide, which change conductivity

on exposure to a range of absorptive gas species [2.68], and catalytic interactions in materials such as palladium and platinum which are typically heated in a protected environment and become hotter still in the presence of the gases whose reactions they catalyse [2.69, 2.70]. However, spectroscopy is a particularly suitable technique to monitor chemical processes and chemical content because all molecular species have a characteristic absorption and emission spectrum which can give reliable identification of a particular molecular combination and also quantitative values of its concentration.

Spectroscopy technique

Spectroscopy is a technique that deals with interactions of matter with electromagnetic radiation in the form of absorption, emission and scattering of radiation energy [2.71]. Spectroscopic techniques have been widely used in gas sensing devices for industrial, environmental and safety monitoring [2.72, 2.73] because they can provide high resolution, sensitive and fast detection and quantification of important chemical species [2.74]. The principle of spectroscopic gas sensing comes from the absorption spectrum of electromagnetic radiation passed through the gas cell due to the gas molecules' own unique absorption spectrum.

Molecules are composed of two or more atoms held together through interaction of the electrons in the outermost orbital shells [2.75]. Typically the movement of molecules include: translation of the whole molecule, rotation of the molecule as a framework around its centre of mass and vibrations of individual atoms within the framework. [2.76]. The vibration of atoms can be excited by absorption of energy from electromagnetic radiation and the molecules' rotation will be induced when the energy absorbed is not enough for vibration excitation. These two types of motions contribute to the molecule absorption spectrum in the infrared region. The spectroscopic relationships with molecules' motions are complicated and have been described in many references [2.77, 2.78, 2.79], and here we will give a summarised description.

The transfer of energy from incident light to gas species which results in an increase of molecular motion is referred to as absorption. The energy gained by the molecule from light absorption excites the molecule to a higher vibration-rotational energy state, and the absorbed light wavelength determines the location of absorption bands in the spectrum.

For the absorption process in molecular vibration, a permanent dipole is essential for strong infrared absorption. In a molecule with different atoms, the vibration causes the electric charge distribution in the bond to change which makes the molecule behave like an oscillating dipole. This varying electric field due to vibration in the molecule interacts with the varying radiation electric field, and in this manner the energy can be transferred from the radiation to the molecule if the frequencies are equal. The molecular vibration frequency determines the absorption wavelength, while the absorption intensity is determined by the energy transfer efficiency from the radiation to the molecule which depends on the change in the dipole moment that occurs during vibration [2.75, 2.79]. For the absorption process in molecular rotation, when the molecule rotates in phase with the varying electric field from radiation (for non-rotating molecule), or the radiation electric field has a frequency equal to the first of the quantized angular frequencies of the rotating molecule to ensure they both move in phase all the time (for rotating molecule), the energy can be transferred from the radiation to the molecule [2.80]. The vibrational energies are typically on the order of a hundred times greater than the rotational energies [2.81]. The fundamental vibration modes of most of the gas species are located in the mid-infrared region, which offers high sensitivity compared to the near-infrared region for gas sensing.

Absorption spectroscopy based gas sensing devices usually include a radiation source, a gas cell for the light interaction with gas species, and a detector, as shown in figure 2.13. Typically a gas cell is a glass or stainless steel tube with transmission windows at both ends which should be clean and transparent for the light beam to travel in and out of the gas cell with low optical losses.

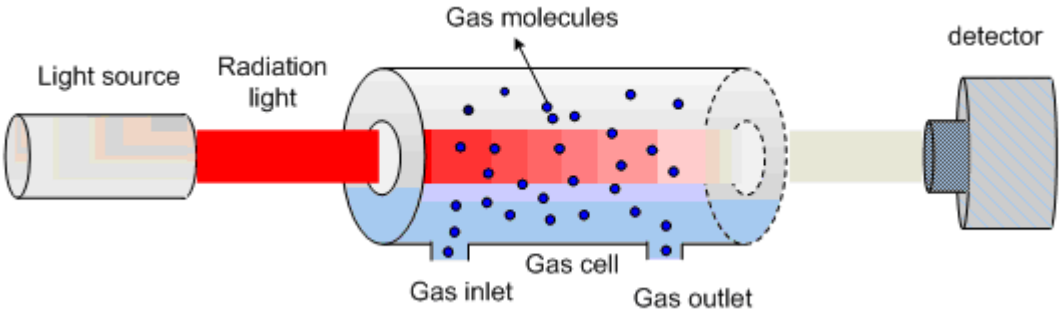

Fig.2.13 Schematic of absorption spectroscopy based gas sensing device

In order to improve the sensitivity, a longer optical interaction length with the gas species is required, and consequently a variety of spectroscopic detection techniques have been developed. Multipass absorption spectroscopy [2.82, 2.83] with a sensitivity of 0.7ppb/$Hz^{1/2}$ for nitric oxide (NO) detection have been achieved by use of a multipass cell with a 36m multiple passes path and 0.3L volume; figure 2.14 shows schematic of a typical multipass absorption spectroscopy. Another approach for achieving long optical path length and minimizing gas cell volumes is to use cavity ringdown spectroscopy (CRDS) [2.84, 2.85] or integrated cavity output spectroscopy (ICOS) [2.86, 2.87], which use a cavity that is created by positioning two highly reflective mirrors, in this manner effective optical path lengths of hundreds of metres can be realized. CRDS is a technique where absorption in the cavity is measured by determining the decay rate of light (cavity ringdown time). Figure 2.15 displays the schematic of a typical ringdown setup that produces an exponential decay of the transmitted light after termination of the laser coupling. Light absorption by the sample inside the cavity causes the light decay rate to increase linearly with respect to its absorption coefficient, which enables either the sample concentration or its absorption strength to be measured accurately. ICOS is a technique that measures absorption features by integrating the entire light signal transmitted through the cavity which is based on the excitation of a dense spectrum of transverse cavity modes and time averaging of the cavity output. Photoacoustic spectroscopy (PAS) has also been used for sensitive trace gas detection [2.88, 2.89], which is based on the generation of an acoustic wave in a gas cell resulting from the absorption of modulated light of appropriate wavelength by molecules, as shown in figure 2.16.

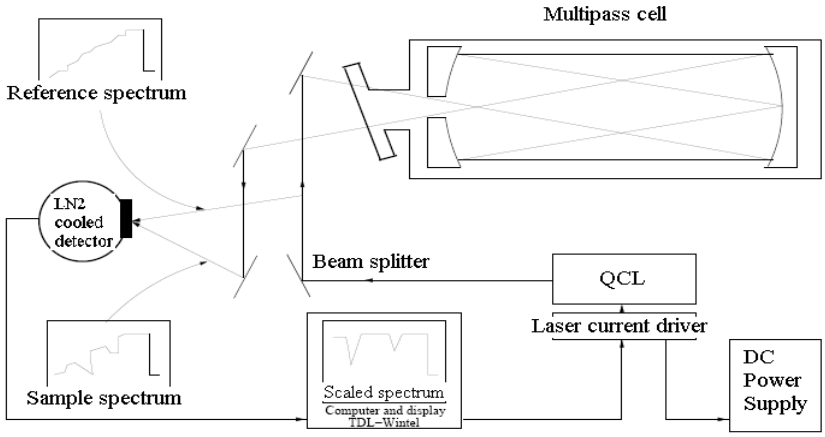

Fig.2.14 Schematic of a typical multipass absorption spectroscopy [2.90]

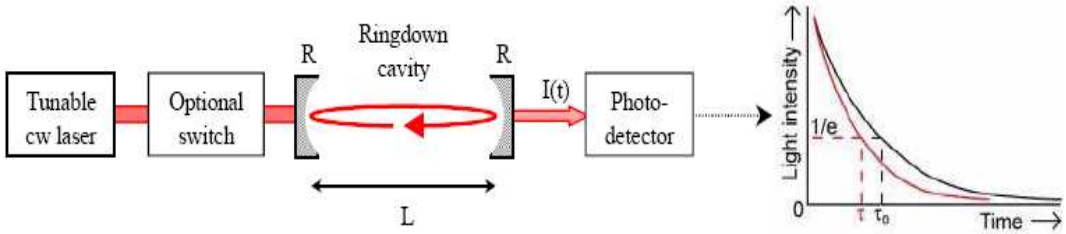

Fig.2.15 Schematic of a typical cavity ringdown absorption spectroscopy setup [2.84]

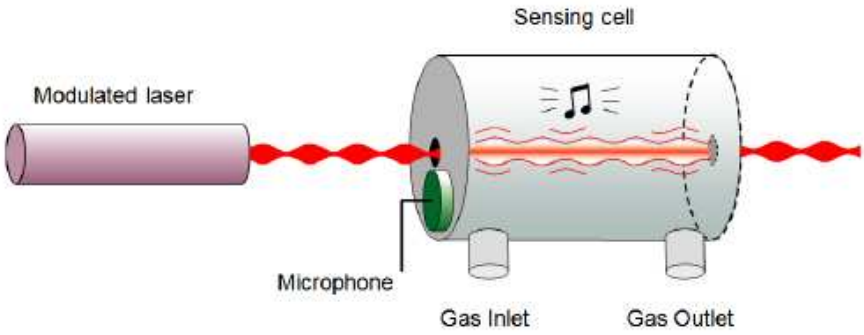

Fig.2.16 Principle schematic of a photoacoustic spectroscopy gas sensor

Besides these techniques, optical fibres have also been used in gas sensing devices which can deliver light to and from the gas sensing element over long distances, and offer potential for sensing applications in remote areas that are hazardous or difficult to access.

Optical fibre spectroscopy gas sensing techniques

Qualitative or quantitative detection of gaseous chemical species by spectroscopic techniques using optical fibre is a very important application area for fibre optic sensors. Detecting systems using the optical fibres can be divided into four categories which are based on the measurement of:

(1) Absorption spectra of the transmitted light;

(2) Reflection spectra;

(3) Emission spectra;

(4) Absorption spectra by using an evanescent wave (ATR-attenuated total internal reflection spectroscopy).

The configurations for each technique is shown in figure 2.17(a~d) respectively.

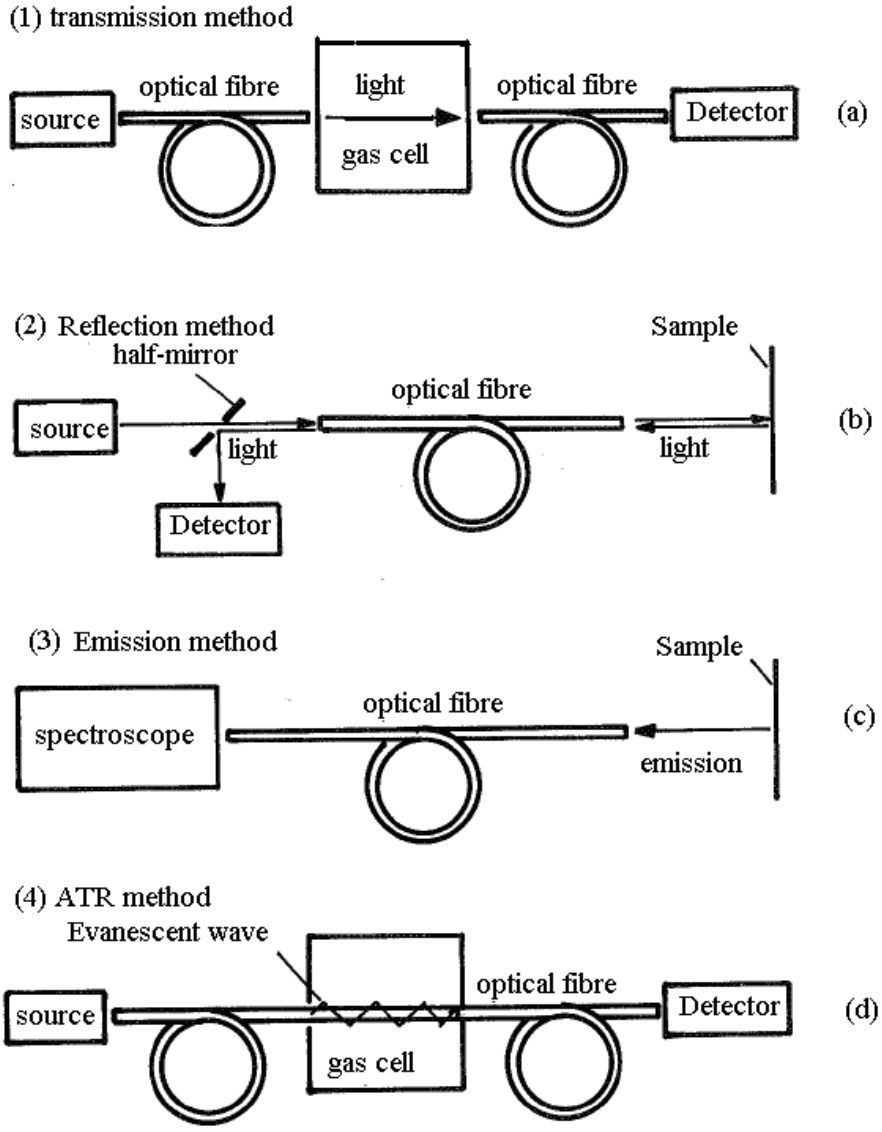

Fig.2.17 Schematics of techniques used for gas species detection [2.69]

Figure 2.17 (a, b) show the schematic of gas species detection system using the absorption spectrum of transmission light (a) or reflection light (b), figure (c) displays the optical fibre gas sensor configuration in which the intrinsic emission spectra of the molecules are used to detect the gas species. The optical fibres in these sensors are used to guide the light into and out the gas cell where the light can interact with the gas species under test. For these types of optical fibre gas sensors, the gas cell is typically relatively large which is not suitable for use in confined spaces, furthermore, the size of cell determines the minimum quantity of gas required which can be a limiting factor if only small gas samples are available. Therefore it is desirable to consider small gas cells which are capable of interrogation from a remote location.

Figure 2.17(d) shows configuration of an optical fibre evanescent field gas sensing method, where a single optical fibre is used as both sensor and a transmission line of optical signals, therefore gas detection can be done in a simple, flexible and possibly distributed way, which also opens the possibility of a substantial overall increase in the sensitivity by increasing the sensing fibre length thus the interaction length with detected gas species.

Optical fibre evanescent field gas sensing techniques

The evanescent wave is a well known effect which is experienced by light at boundaries with a refractive index change. For an optical fibre, in which although the light is guided in the inner core of higher refractive index by total internal reflection, part of the optical field enters and travels in the cladding area, as shown in figure 2.18. Typically the field strength decreases in an exponential way outside the core regardless of the fibre shape or modal distribution, and the actual penetration depth is related with the normalised frequency number (V value); the lower the value of V, the greater the evanescent wave penetration into the cladding.

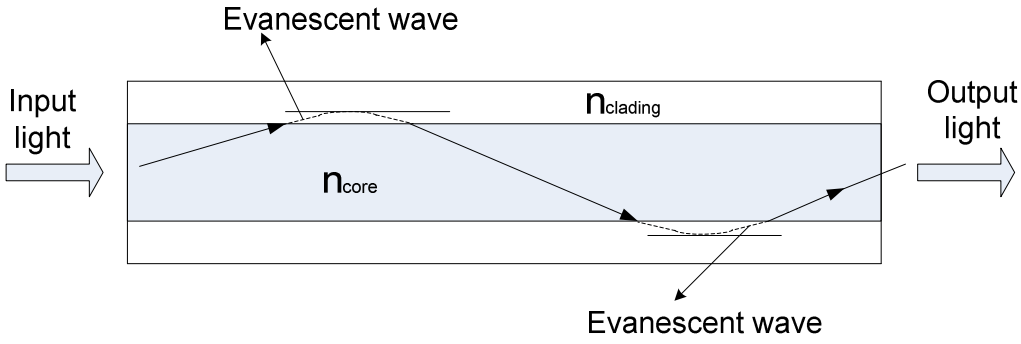

Fig.2.18 Evanescent wave propagation in optical fibre cladding

If the cladding is partly removed or ground down in the fibre fabrication process, the evanescent wave is able to interact with the measurand such as chemical species surrounding the optical fibre. The absorption of power from the evanescent wave and thus the guided light intensity due to the chemical species absorption provides the basis for many optical fibre evanescent field gas sensing schemes [2.110].

The interaction strength of the evanescent field with the detected gas species is one of the most important parameters which influences the sensitivity of optical fibre evanescent field gas sensing devices. The evanescent field penetration depth is also dependent on the geometry of the optical fibre. In order to increase the interaction strength of the evanescent field with the detected gas species, many type of fibre geometries have been developed and used for the gas species detection, such as D-shaped fibre [2.91, 2.92, 2.93], tapered fibre [2.94, 2.95, 2.96], macrostructure fibre or hollow core photonic bandgap fibre [2.97, 2.98, 2.99],as shown in figure 2.19. For a D-shaped fibre evanescent field gas sensor, bending may have a significant effect on the sensitivity. An increase of 30% (R=12cm) in the sensitivity occurs when the fibre is curved with its flat surface to the outside while a reduction in the sensitivity to zero can be found with the same amount of curvature in the opposite direction [2.100] because the electromagnetic fields in the fibre are affected by the geometrical deformation of the fibre axes. Hollow core photonic bandgap fibre offers advantages of higher light gas interaction strength because such fibres can guide over 99% [2.97] of the light outside the fibre material and into the hollow core, while the diffusion time of the gas into the sensing region such as the air core for hollow-core fibre should be taken into account

for sensor design. Recently, a tapered microstructured optical fibre with collapsed air-holes coated with gas-permeable thin films was used for gas sensing [2.101], as shown in figure 2.20. Using this type of sensing device, the sensor response time can be very fast since there is no need to fill the air-holes of the microstructured optical fibre (MOF) with the gas species, furthermore, the interaction length can be short without sacrificing the sensor sensitivity.

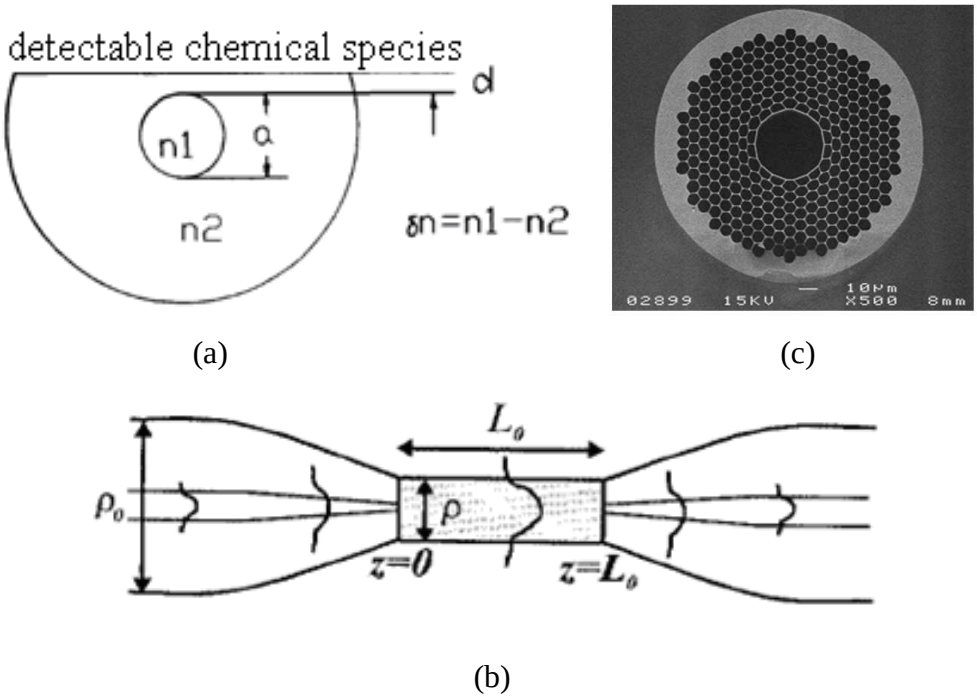

Fig.2.19 Different type of fibre geometries of D-shape (a), tapered (b) and hollow core photonic bandgap (c) as sensing elements in fibre evanescent field gas sensor

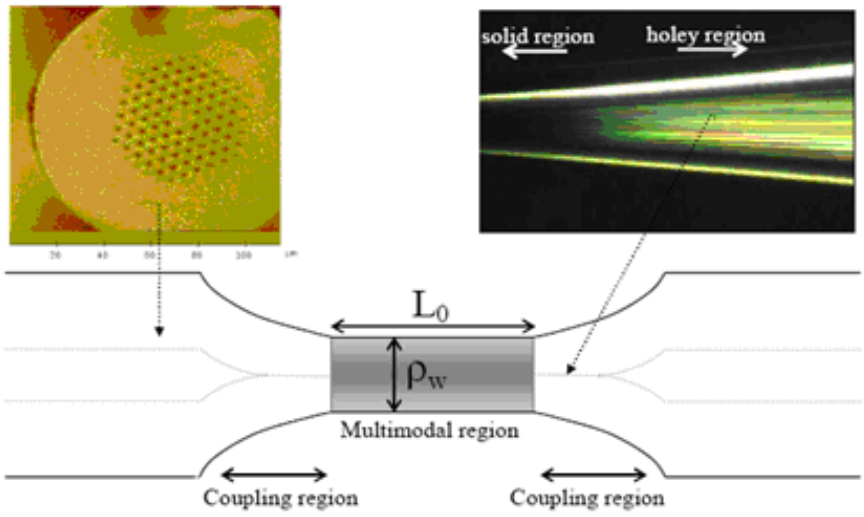

Fig.2.20 A tapered microstructured optical fibre with collapsed air-holes coated with gas-permeable thin films as sensing element for evanescent field gas sensor [2.101]

In most of these applications, the weak overtone absorption peaks in the near infrared wavelength (0.5~2μm) of gas species are used due to the limited silica transmission window, thus longer interaction lengths and high sensitivity techniques are required to make useful gas concentration measurements. Consequently mid-IR spectroscopy, by probing the gas species at the fundamental resonances, offers potential for enhanced sensitivity of gas sensing devices, and fibres made from tellurite or germanate glasses could be good options both as transmission line of optical signals and sensing elements due to their high transmission properties in the mid-infrared wavelength region. For the work in this thesis, the evanescent field gas sensing devices based on tellurite and germanate glass fibres with different type of geometries are modelled and investigated, and will be described in detail in chapter 5.

2.5 Mid-infrared Light Sources

As described in previous sections, the mid-infrared transmitting glasses-tellurite and germanate glass fibres offer much potential in the applications of remote and distributed flammable gas sensing devices at the fundamental vibrational absorption lines of gas species between 3 and 24 μm, thus the development of mid-infrared sources

suitable for use with optical fibres is the primary problem in the optical fibre gas sensing devices.

Thermal broadband sources such as a halogen lamp have been used in the hollow-core photonic bandgap fibre mid-infrared gas sensing devices [2.102], however due to the large emission area, it is difficult to efficiently couple to optical fibres with small core diameters of the order of 100μm.

The LED source has great potential for IR fibre sensors. The mid-infrared emitting InGaAs LEDs with a central wavelength of 3.36μm and a peak power of 1μW at room temperature have been applied to methane gas species detection [2.103]. However the efficient coupling from the LED source to fibre is still a big problem due to its wide divergence angle, and the power utilization is lower because of its broad spectrum compared with the selected gas absorption line.

Laser sources offer great potential for the mid-infrared gas sensing devices using spectroscopic techniques due to their advantages of high optical peak power and single frequency operation with good spectral purity and wide tunability in the mid-infrared region. The developed laser sources operating in the mid-infrared region include tuneable diode lasers [2.83], coherent sources based on difference frequency generation (DFG) [2.104] and optical parametric oscillators (OPO) [2.97, 2.105], quantum and interband cascade lasers [2.82, 2.86, 2.87, 2.88, 2.89, 2.106]. Lead salt diode lasers were the first lasers used for the spectroscopy gas sensing devices, which are typically large in size and require cooling to temperatures lower than 90K. DFG and OPO are mid-infrared wavelength conversion lasers based on difference frequency generation and optical parametric oscillators in bulk periodically poled crystals, such as $AgGaSe_2$ [2.107], $LiNbO_3$ [2.108], $AgGaS_2$ [2.109] and PPLN [2.105], which can produce mid-infrared coherent light using quasi-phase matching when pumped by lasers in the visible and near-infrared region. The quantum cascade lasers are based on the manufacture of a type of artificial semiconductor which comprises a periodic series of thin layers of varying material composition forming a superlattice. Because the laser emission is determined by the layer thicknesses and not the material [2.106], the quantum cascade lasers can be fabricated to operate at any of a very wide range of wavelengths from ~3μm to ~24μm.

For the work in this thesis, a compact nanosecond monolithic optical parametric oscillator using quasi-phase matching to generate mid-infrared light source is investigated for the gas sensing device modelling and will be described in chapter 5.

2.6 Conclusion

In this chapter, the basic optics of fibres, mid-infrared optical fibres, and sensing techniques based on optical fibres have been briefly reviewed. In the following chapters experimental measurement of germanate and tellurite glass fibre sensing properties and modelling in the application of gas sensing devices will be described in more detail.

2.7 References

[2.1] A. Ghatak, K. Thyagarajan. *Introduction to Fiber Optics.* Cambridge University Press, UK, 1998

[2.2] R. Van Boxel. *Thesis: Bragg gratings in photosensitive graded index polymer optical fibres*. Katholieke University Leuven, 2005

[2.3] J. A. Buck. *Fundamentals of Optical Fibres*. Wiley-Interscience, 1995

[2.4] A. W. Snyder, J. D. Love. *Optical Waveguide Theory.* Chapman and Hall, 1991

[2.5] D. Marcuse. *Theory of Dielectric Optical Waveguides.* Academic Press, 2nd edition, 1991

[2.6] C. Ysao. *Optical Fibre Waveguide Analysis*. Oxford Science Publications, 1992

[2.7] N. S. Kapany, and R. J. Simms. *Recent developments of infrared fiber optics*. Infrared Physics, Vol.5, pp.69, 1965

[2.8] T. Katsuyama, and H. Matsumura. *Infrared Optical Fibers.* IOP Publishing Ltd, Adam Hilger, Bristol, UK, 1989

[2.9] J. A. Harrington. *Infrared fibers and their applications.* SPIE Press, Bellingham, Washington USA, 2004

[2.10] T. Miyashita, and T. Manabe. *Infrared optical fibers.* IEEE Journal of Quantum Electronics, Vol.QE-18, No.10, pp.1432-1540, 1982

[2.11] S. Mitachi, Y. Ohishi, T. Miyashita. *A fluoride glass optical fiber operating in the Mid-Infrared wavelength range*. Journal of Lightwave Technology, Vol. LT-1, No.1, 1983

[2.12] T. Kanamori, Y. Terunuma, S. Takahashi, T. Miyashita. *Chalcogenide glass fibers for Mid-Infrared transmission*. Journal of Lightwave technology, Vol. LT-2, No.5, 1984

[2.13] T. M. Munro, Y. D. West, D. W. Hewak, N. G. R. Broderick, and D. J. Richardson. *Chalcogenide holey fibres*. Electronic Letters, Vol. 36, pp. 1998-2000, 2000

[2.14] J. M. Jewell, I. D. Aggarwal. *Structural influences on the hydroxyl spectra of barium gallogermanate glasses.* J.Non-Cryst Solids, Vol. 181, pp. 189-199, 1995

[2.15] I. D. Aggarwal, S. S. Bayya, G. D. Chin, J. S. Sanghera. *Vis-IR transmitting BGG glass windows*. Processings of DoD Electromagnetic Symposium, 2004

[2.16] S. S. Bayya, G. D. Chin, J. S. Sanghera, I. D. Aggarwal. *Germanate glass as a window for high energy laser systems.* Optics Express, Vol. 14, No. 24, pp. 11687-11693, Nov.2006

[2.17] E. Sayed, S. Yousef. *Characterization of oxyfluoride tellurite glasses through thermal, optical and ultrasonic measurements.* Journal of Physics D: Applied Physics, Vol. 38, pp. 3970-3975, 2005

[2.18] P. Klocek. *Handbook of Infrared Optical Materials*. Marcel Dekker Inc, New York, USA, 1991

[2.19] H. Li, J. Lousteau, W. N. MacPherson, X. Jiang, H. Y. Bookey, J. S. Barton, A. Jha, A. K. Kar. *Thermal phase sensitivity of tellurite and germanate optical fibers.* Optics Express, Vol. 15, No.14, pp. 8857- 8863, July, 2007

[2.20] I. Rabukhin. *Concentration dependences of elastooptic coefficients of germanate glasses containing lead and bismuth oxides.* Glass and Ceramics. Vol. 37, pp. 87-90, 1995

[2.21] A. Koike, N. Sugimoto. *Temperature dependences of optical path length in fluorine-doped silica glass and bismuthate glass*. Proc. SPIE 6116, 61160Y1-61160Y8, 2006

[2.22] S. M. Lima, W. F. Falco, E. S. Bannwart, L. H. C. Andrade, R. C. de Oliveira, J. C. S. Moraes, K. Yukimitu etc. *Thermo-optical characterization of tellurite glasses by thermal lens, thermal relaxation calorimetry and interferometric methods*. Journal of Non-Crystalline Solids, Vol. 352, pp. 3603-3607, 2006

[2.23] E. L. Adawy, R. E. L. Mallawany. *Elastic modulus of tellurite glasses*. Journal of Materials Science Letters, Vol. 15, pp. 2065-2067, 1996

[2.24] K. Ghatak, K. Thyagarajan. *Optical Electronics*. Cambridge University Press, 1989

[2.25] R. Hughes, R. Priest. *Thermally induced optical phase effects in fiber optic sensors*. Applied Optics, Vol. 19, pp. 1477-1483, 1980

[2.26] M. Fukuhara, A. Sanpei, K. Shibuki. *Low Temperature Elastic Moduli, Debye Temperature and Internal Dilational and Shear Frictions of Fused Quartz.* Journal of Materials Science Letters, Vol. 32, pp. 1207-1211, 1997

[2.27] R. RJ. Maier, W. N. MacPherson, J. S. Barton, J. DC. Jones, S. McCulloch, G. Burnell. *Temperature dependence of the stress response of fibre Bragg gratings*. Measurement Science & Technology, Vol. 15, pp. 1601 – 1606, 2004

[2.28] A. Bertholds, R. Daendliker. *Determination of the individual strain optic coefficients in single mode optical fibers*. Journal of Lightwave Technology, Vol. 6, No.1, pp. 17-20, 1988

[2.29] D. Cotter. *Observation of stimulated Brillouin scattering in low-loss silica fiber at 1.3μm*. Electronics Letters, Vol. 18. pp. 495-496, 1982

[2.30] A. Jha, S. Shen, M. Naftaly. *Structural origin of spectral broadening of 1.5-μm emission in Er^{3+}-doped tellurite glasses*. Physics Review B: Condense Materials, Vol. 62, No. 10, pp. 6215-6227, 2000

[2.31] A. Jha, J. Lousteau, G. Jose, S. Shen, Y. Wei, R. V. Penty, I. H. White, H. T. Bookey, A.K. Kar. *Rare-earth oxide doped single and multi-cores heavy metal oxide fibres for lasers and amplifiers*. ICTON 2008, Vol. 3, pp. 252-255, 2008

[2.32] H. T. Bookey, J. Lousteau, A. Jha, N. Gayraud, R. R. Thomson, N. D. Psaila, H. Li, W. N. MacPherson, J. S. Barton, A. K. Kar. *Multiple rare earth emissions in a multicore tellurite fiber with a single pump wavelength*. Optics Express, Vol. 15, pp. 17554-17561, 2007

[2.33] M. Reben, J. Wasylak. *Tellurite glasses for optical fibre fabrication*. Proceeding of SPIE, Vol. 7120, 712001, 2008

[2.34] D. Furniss, A.B. Seddon. *Towards Monomode proportioned fibre optic preforms by extrusion.* Journal of Non-Crystal Solids, Vol. 256&257, pp. 232-236, 1999

[2.35] V.V. Ravi Kanth Kumar, A.K. George, J.C. Knight, P. St. J. Russell. *Tellurite photonic crystal fiber*. Optics. Express, Vol. 11, pp. 2641-2645, 2003

[2.36] J. Lousteau, H.T. Bookey, X. Jiang, C. A. Hill, A. Kar, A. Jha. *Fabrication of Multicore Tellurite Glass Optical Fibres*. ICTON 2007, Rome, Paper WeB4.3

[2.37] W. N. MacPherson, M. J. Gander, J. S. Barton, J. DC. Jones, C. L. Owen, A. J. Watson, R. M. Allen. *Blast-pressure measurement with a high-bandwidth fibre-optic pressure sensor.* Measurement science and technology, Vol. 11, No. 2, 2000

[2.38] G.B. Hocker. *Fibre optic sensing of pressure and temperature*. Applied Optics, Vol. 18, 1979

[2.39] A. Cusano, A. Cutolo, J. Nasser, M. Giordano, A. Calabro. *Dynamic strain measurements by fibre Bragg grating sensor.* Sensors and actuators A: Physical, Vol. 110, No. 1-3, 2004

[2.40] Y. G. Zhan, H. W. Cai, R. H. Qu, S. Q. Xiang, Z. J. Fang, X. Z. Wang. *Fiber Bragg grating temperature sensor for multiplexed measurement with high resolution*. Optical engineering, Vol. 43, No. 10, 2004

[2.41] E. Udd. *Fiber optic smart structures*. Proceeding of the IEEE, Vol. 84, No. 1, pp. 60-67, 1996

[2.42] D. A. Jackson. *Recent progress in monomode fiberoptic sensors*. Measurement Science & Technology. Vol. 5, No. 6, pp. 621-638, 1994

[2.43] J. Dakin, B. Culshaw (ed). *Optical Fiber Sensors: Principles and Components*. Artech House, 1988

[2.44] B. Culshaw, J. Dakin (ed). *Optical Fiber Sensors. Vol. 2: Systems and Applications.* Artech House, 1989

[2.45] E. Udd (ed). *Fiber Optic Sensors: An Introduction for Scientists and Engineers.* John Wiley and Sons, 1991

[2.46] A. D. Kersey. *A review of recent developments in fiber optic sensor technology.* Optical Fiber Technology, Vol. 2, pp. 291-317, 1996

[2.47] D. A. Flavin, R. McBride, J. D. C. Jones. *Interferometric fiber-optic sensing based on the modulatin of group delay and first-order dispersion- application to strain-temperature measurand.* Journal of Lightwave Technology, Vol. 13, No. 7, pp. 1314-1323, 1995

[2.48] T. Liu, D. Brooks, A. martin, R. Badcock, B. Palph, G. F. Fernando. *A multi-mode extrinsic Fabry-Perot interferometric strain sensor.* Smart Materials & Structures, Vol. 6, No. 4, pp. 464-469, 1997

[2.49] S. C. Kaddu, S. F. Collins, D. J. Booth. *Multiplexed intrinsic optical fibre Fabry-Perot temperature and strain sensors addressed using white-light interferometry.* Measurement Science & Technology, Vol. 10, No. 5, pp. 416-420, 1999

[2.50] C. E. Lee. *Interferometric optical fibre sensors using internal mirrors.* Electronics Letters, Vol. 24, No. 4, pp. 193-194, 1988

[2.51] H. S. Choi. *High-performance fiber-optic temperature sensor using low-coherence interferometry.* Optics Letters, Vol. 22, No. 23, pp.1814-1816, 1997

[2.52] C. L. Chen. *Optical fiber Fabry-Perot sensors.* Applied Optics, Vol. 27, No. 3, pp. 547-551, 1988

[2.53] B. S. Kawasaki. *Narrow-band Bragg reflectors in optical fibers.* Optics Letters, Vol. 3, pp. 66-68, 1978

[2.54] K. O. Hill. *Photosensitivity on optical fiber waveguides: application to reflection filter fabrication.* Applied Physics Letters, Vol. 32, pp. 647-649, 1978

[2.55] I. Bennion, J. A. R. Williams, L. Zhang, K. Sugden, N. J. Doran. *UV-writtten in fiber Bragg gratings.* Optical and Quantum Electronics, Vol. 28, No. 2, pp.93-135, 1996

[2.56] A. Othonos. *Fiber Bragg gratings.* Review of Scientific Instruments, Vol. 68, No. 12, pp. 4309-4341, 1997

[2.57] Y. J. Rao. *In-fibre Bragg grating sensors.* Measurement Science & Technology, Vol. 8, No. 4, pp. 355-375, 1997

[2.58] R. R. J. Maier. Thesis*: Application of fibre Bragg gratings in sensor technology*. Heriot-Watt University, 2006

[2.59] R. Suo, J. Lousteau, H. Li, X. Jiang, K. Zhou, L. Zhang, W. N. MacPherson, H. T. Bookey, J. S. Barton, A. K. Kar, A. Jha, and I. Bennion. *Fiber Bragg gratings inscribed using 800nm femtosecond laser and a phase mask in single and multi-core mid-IR glass fibers.* Optics Express, Vol. 17, pp. 7540-7548, 2009

[2.60] G. M. H. Flockhart. *Thesis: Interferometric interrogation of optical fibre Bragg grating sensors for temperature independent strain measurement.* Heriot-Watt University, 2001

[2.61] G. A. Ball, W. W. Morey, P. K. Cheo. *Fiber laser source/analyser for Bragg grating sensor array interrogation.* Journal of Lightwave Technology, Vol. 12, No. 4, pp. 700-703, 1994

[2.62] M. G. Xu. *Optical in-fibre grating high pressure sensor*. Electronics Letters, Vol. 29, pp. 398, 1993

[2.63] W. W. Morey. *Evaluation of a fibre Bragg grating hydrostatic pressure sensor*. Proc. 8th OFS conference, Monterey, USA, 1992

[2.64] Cassidy. *Wavelength division multiplexed sensor network using Bragg fibre reflection gratings.* Electronics Letters, Vol. 28, pp. 1734, 1992

[2.65] D. A. Flavin, R. McBride, J. D. C. Jones. *Short optical scan interferometer interrogation of a fibre Bragg grating embedded in a composite*. Electronics Letters, Vol. 33, No. 4, pp. 319-321, 1997

[2.66] S. M. Melle, K. liu, R. M. Measures. *Practical fiber-optic Bragg grating strain gauge system.* Applied Optics, Vol. 32, No. 19, pp. 3601-3609, 1993

[2.67] F. Wolfbeis. *Fibre Optic Chemical Sensors and Biosensors*. CRC Press, Boca Raton, Florida, 1992

[2.68] J. Fraden. *Handbook of Modern Sensors: Physics, Designs, and Applications.* 3rd ed. AIP Press/Springer, New York, 2004

[2.69] J. G. Webster (ed). *The Measurement, Instrumentation and Sensors Handbook.* CRC Press, Boca Raton, Florida, 1999

[2.70] J. Janata. *Principles of Chemical Sensors.* Plenum Press, New York, 1989

[2.71] C. N. Banwell, E. M. McCash. *Fundamentals of Molecular Spectroscopy.* McGraw-Hill, London, 4th edition, 1994

[2.72] G. Stewart, G. Whitenett, P. Shields, J. marshall, B. Culshaw. *Design of fibre laser and sensor systems for gas spectroscopy in the near-IR.* Proc. Industrial and Highway Sensors Technology, Bellingham, WA, pp. 172-180, 2004

[2.73] J. Marshall, G. Stewart, G. Whitenett. *Design of a tunable L-band multi-wavelength laser system for application to gas spectroscopy.* Measurement Science and Technology, Vol. 17, pp. 1023-1031, 2006

[2.74] T. A. Blake, J. F. Kelly, T. L. Stewart, J. S. Hartman, S. W. Sharpe, R. L. Sams. *Absorption spectroscopy in hollow-glass waveguides using infrared diode lasers.* Proc. Diode Lasers and Applications in Atmospheric Sensing, pp. 216-232, 2002

[2.75] H. Gunzler, H. U. Germlich. *IR Spectroscopy: An Introduction.* Wiley-VCH, 2002

[2.76] K. E. Stine. *Modern Practices in Infrared Spectroscopy: Laboratory Manual*. Beckman.

[2.77] K. Kiss-Eross. *Analytical Infrared Spectroscopy*. Wilson & Wilson's Comprehensive Analytical Chemistry, Vol. VI, Elsevier Scientific Publishing, 1976

[2.78] D. N. Kendall. *Applied Infrared Spectroscopy*. Reinhold Publishing, New York, 1966

[2.79] J. E. Grooks. *The Spectrum in Chemistry.* Academic Press Inc., London, 1978

[2.80] J. H. V. D. Maas. *Basic Infrared Spectroscopy.* 2nd ed, Heyden & Son Ltd., 1972

[2.81] W. West. *Chemical Applications of Spectroscopy*. Technique of Organic Chemistry, Vol. 9, A. Weissberger, Ed., 2 ed: Interscience Publisher, Inc., 1968.

[2.82] D. D. Nelson, J. H. Shorter, J. B. McManus, M. S. Zahniser. *Sub-part-per-billion detection of nitric oxide in air using a thermoelectrically cooled mid-infrared quantum cascade laser spectrometer.* Applied Physics B, Vol. 75, pp. 343-350, 2002

[2.83] C. Roller, K. Namjou, J. D. Jeffers, M. Camp, A. Mock, P. J. McCann, J. Grego. *Nitric oxide breath testing by tunable diode laser absorption spectroscopy: application in monitoring respiratory inflammation*. Applied Optics, Vol. 41, pp. 6018-6029, 2002

[2.84] I. Debecker, A. K. Mohamed. *High-speed cavity ringdown spectroscopy with increased spectral resolution by simultaneous laser and cavity tuning.* Optics Express, Vol. 13, No. 8, pp. 2906-2915, 2005

[2.85] J. B. Dudek, P. B. Tarsa, A. Velasquez, M. Wladyslawski, P. Rabinowitz, K. K. Lehmann. *Trace moisture detection using continuous-wave cavity ring-down spectroscopy.* Analytical Chemistry, Vol. 75, No. 17, pp. 4599-4605, 2003

[2.86] M. L. Silva, D. M. Sonnenfroh, D. I. Rosen, M. G. Allen, A. O'Keefe. *Integrated cavity output spectroscopy measurements of nitric oxide levels in breath with a pulsed room-temperature quantum cascade laser.* Applied Physics B, Vol. 81, pp. 705-710, 2005

[2.87] Y. A. Bakhirkin, A. Kosterev, C. Roller, R. F. Curl, F. K. Tittel. *Mid-infrared quantum cascade laser based off-axis integrated cavity output spectroscopy for biogenic nitric oxide detection.* Applied Optics, Vol. 43, No. 11, pp. 2257-2266, 2004

[2.88] A. Kosterev, G. Wysocki, Y. Bakhirkin, S. So, R. Lewicki, M. Fraser, F. Tittel, R. F. Curl. *Applications of quantum cascade lasers to trace gas analysis.* Applied Physics B, Vol. 90, pp.165-176, 2008

[2.89] A. Elia, C. D. Franco, P. M. Lugara, G. Scamarcio. *Photoacoustic spectroscopy with quantum cascade lasers for trace gas detection.* Sensors, Vol. 6, pp. 1411-1419, 2006

[2.90] P. S. Kroon, A. Hensen, H.J. J. Jonker, M. S. Zahniser, W. H. Van't Veen, A. T. Vermeulen. *Suitability of quantum cascade laser spectroscopy for CH_4 and N_2O eddy covariance flux measurements.* Biogeosciences, Vol. 4, pp. 715-728, 2007

[2.91] W. Jin, G. Stewart, M. Wilkinson, B. Culshaw, F. Muhammad, S. Murray, J. O. W. Norris. *Compensation for surface contamination in a D-fiber evanescent wave methane sensor.* Journal of Lightwave Technology, Vol. 13, No. 6, pp.1177-1183, 1995

[2.92] G. Stewart, W. Jin, B. Culshaw. *Prospects for fibre-optic evanescent-field gas sensors using absorption in the near-infrared.* Sensors and Actuators B, Vol. 38-39, pp.42-47, 1997

[2.93] G. Stewart, J. Norris, D. F. Clark, B. Culshaw. *Evanescent-wave chemical sensors – a theoretical evaluation.* International Journal of Optoelectronics, Vol. 6, No. 3, pp. 227-238, 1991

[2.94] H. Tai, H. Tanaka, T. Yoshino. *Fiber-optic evanescent-wave methane-gas sensor using optical absorption for the 3.392-μm line of a He-Ne laser*. Optics Letters, Vol. 12, No. 6, pp. 437-439, 1987

[2.95] J. Villatoro, D. M. Hernandez, E. Mejia. *Fabrication and modelling of uniform-waist single-mode tapered optical fiber sensors.* Applied Optics, Vol. 42, No. 13, pp. 2278-2283, 2003

[2.96] C. D. Singh, Y. Shibata, M. Ogita. *A theoretical study of tapered, porous clad optical fibers for detection of gases.* Sensors and Actuators B, Vol. 92, pp. 44-48, 2003

[2.97] N. Gayraud, l. W. Kornaszewski, J. M. Stone, J. C. Knight, D. T. Reid, D. P. Hand, W. N. MacPherson. *Mid-infrared gas sensing using a photonic bandgap fiber.* Applied Optics, Vol. 47, pp. 1269-1277, 2008

[2.98] G. Pickrell, W. Peng, A. Wang. *Random-hole optical fiber evanescent-wave gas sensing*. Optics Letters, Vol. 29, No. 13, pp.1476-1478, 2004

[2.99] J. B. Jensen, L. H. Pedersen, P. E. Hoiby, L. B. Nielsen, T. P. Hansen, J. R. Folkenberg. *Photonic crystal fiber based evanescent-wave sensor for detection of biomolecules in aqueous solutions.* Optics Letters, Vol. 29, No. 17, pp. 1974-1976, 2004

[2.100] F. A. Muhammad, H. S. Al-Raweshidy. *Analysis of curved D-fiber for methane gas sensing.* IEEE Photonics Technology Letters, Vol. 7, No, 5, pp. 538-539, 1995

[2.101] V. P. Minkovich, D. M. Hernandez. *Microstructured optical fiber coated with thin films for gas and chemical sensing.* Optics Express, Vol. 14, No. 18, pp. 8413-8418, 2006

[2.102] N. Gayraud, J. M. Stone, W. N. MacPherson, J.D. Shephard, R. R. J. Maier, J. C. Knight, D. P. Hand, J. D. C. Jones. *Mid-infrared gas sensing using a photonic bandgap fiber.* In Proc. Inter. Conf. Optical Fiber Sensors (OFS-18), pp. ThA5, Mexico, 2006

[2.103] S. McCabe, B. D. MacCraith. *Novel mid-infrared LED as a source for optical fibre gas sensing.* Electronics Letters, Vol. 29, no, 19, pp. 1719-1720, 1993

[2.104] K. Fradkin, A. Arie, A. Skliar, G. Rosenman. *Tunable midinfrared source by difference frequency generation in bulk periodically poled $KTiOPO_4$.* Applied Physics Letters, Vol. 74, No. 7, pp. 914-916, 1999

[2.105] K. A. Tillman, D. T. Reid. *Monolithic optical parametric oscillator using chirped quasi-phase matching.* Optics Letters, Vol. 32, No. 11, pp. 1548-1550, 2007

[2.106] G. Duxbury, N. Langford. *Quantum cascade lasers bring sensitivity and speed to infrared gas sensing.* Spectroscopy Europe, Vol. 18, No, 5, pp. 18-23, 2006

[2.107] U. Simon, Z. Benko, M. W. Sigrist, R. F. Curl, F. K. Tittel. *Design considerations of an infrared spectrometer based on difference-frequency generation in $AgGaSe_2$.* Applied Optics, Vol. 32, pp. 6650-6655, 1993

[2.108] M. Seiter, D. Keller, M. W. Sigrist. *Broadly tunable difference-frequency spectrometer for trace gas detection with noncolinear critical phase-matching in $LiNbO_3$.* Applied Physics B: Lasers and Optics, Vol. 67, No. 3, pp.351-356, 1998

[2.109] K. P. Petrov, S. Waltman, U. Simon, R. F. Curl, F. K. Tittel, E. J. Dlugokencky, L. Hollberg. *Detection of methane in air using diode-laser pumped difference-frequency generation near 3.2 μm.* Applied Physics B: Lasers and Optics, Vol. 61, No. 6, pp. 553-558, 1995

[2.110] G. M. H. Flockhart. Thesis*: Interferometric Interrogation of Optical Fibre Bragg Gratng Sensors for Temperature Independent Strain Measurement*. Heriot-Watt University, 2001

Chapter 3

Tellurite and Germanate Glass Fibre Characterization: Thermal Properties

3.1 Introduction

Tellurite and germanate glass fibers have potential for applications both in fundamental research [3.1, 3.2, 3.3] and in optical device fabrication [3.4]. The high refractive index and optical nonlinearity, resistance to corrosion, low melting temperature and good transmission properties in the visible to infrared region (0.35-6μm) [3.5, 3.6] make them promising candidates for many linear and nonlinear optical devices [3.1]. Applications may include bio/chemical and gas sensing [3.7, 3.8], nonlinear optical signal processing [3.6], Raman amplification or mid-infrared continuum generation [3.9, 3.10]. Section 2.3.1 indicated that tellurite glasses can be used to fabricate optical amplifiers and lasers, because they are capable of incorporating large concentrations of rare-earth ions [3.11] with their relatively low phonon energy (750-780cm^{-1}) compared with other oxide glasses such as silicate (1100cm^{-1}) and phosphate (1200cm^{-1}) glasses. These properties also make tellurite glass an ideal candidate for optical fiber and planar waveguide fabrication [3.12]. Among these applications, the thermo-optical properties of fibres are important parameters which are required to model, design and operate fibre lasers, amplifiers and sensors. Thus investigating the characteristics of tellurite and germanate glass fibre such as dispersion and thermal response are useful and important for both optical component design and sensor applications.

The aim of this chapter is to investigate the chromatic dispersion characteristics and the thermal sensing properties of tellurite and germanate glass fibres. Section 3.2 describes an asymmetric fusion splicing technique which is used for the splicing of

tellurite or germanate glass fibre with silica fibre. Sections 3.3 describes the refractive index and chromatic dispersion measurement of tellurite and germanate glass fibres using low-coherence interferometry which is based on dispersive Fourier transform spectroscopy. In section 3.4, the thermal responses of tellurite and germanate glass fibres are investigated by measuring the phase sensitivity to temperature of a fibre Fabry-Perot (FFP) cavity, which is formed by splicing these soft glass fibres to a single mode silica fibre. The temperature coefficients normalized to the fibre length L as $\frac{1}{L}\frac{d\phi}{dT}$ rad m^{-1} K^{-1} of these two material fibres have been obtained over a temperature range 280K to 320K, and contributions from the thermal expansion, thermal optical effects and electronic polarizability are discussed. Then the thermal responses of FBGs in tellurite and germanate glass fibres fabricated by Aston University are described in section 3.5, which are consistent with the results described in section 3.4.

3.2 Tellurite and Germanate Glass Fibre Handling: Cleaving and Splicing

Tellurite glass (mol%): $75TeO_2$-$15ZnO$-$10Na_2O$ and germanate glass (mol%): $56GeO_2$-$31PbO$-$9Na_2O$-$4Ga_2O_3$ fibers were manufactured using rotational casting and extrusion by colleagues in Leeds University. Fibre diameter was 130±20 μm with a core diameter of 80±13 μm (multimode) and 10±1.5 μm (single mode), as shown in figure 3.2 and figure 3.4. This fibre can not be cleaved using a standard fibre cleaver because they are too fragile, therefore the fibres were cleaved by hand using a diamond scribe.

3.2.1 Asymmetric Splicing Method

In the field of fibre optics, joining of optical fibres is a well-known and widely practiced technique. The most common method for splicing two standard fused silica fibres is based on the fusion of the adjacent ends of the optical fibres that are to be joined. The fibres are brought close to each other and are aligned so that their cores are coaxial with each other. Heat is transferred to both fibre ends by an electric arc or heated-filament positioned on either sides of the axis of the two optical fibres. This heat is sufficient to soften the glass at the end of each of the two fibres to be joined .The optical fibres are then brought into contact and the temperature is lowered below the

softening and glass transition temperatures to form a permanent bond between the fibres [3.13]. This techniques can be used to fuse fibres that have the same or very similar material compositions, and has been optimised commercially for fused silica fibres. Typical splicing losses are lower than 0.1dB per splice for singlemode fused silica fibres.

In our experiment, we want to splice the tellurite or germanate glass fibre with the silica fibre. These two types of fibres have different glass compositions and substantially different softening temperatures. Typically tellurite or germanate glass has a much lower softening temperature (approximately 320^{o}C and 480^{o}C respectively) than silica (~ 1200 ^{o}C). The mismatch between the softening temperatures is too great for a conventional splice approach, but the asymmetric configuration, as shown in figure 3.1, is suitable for splicing lower temperature soft glass fibre to silica fibre.

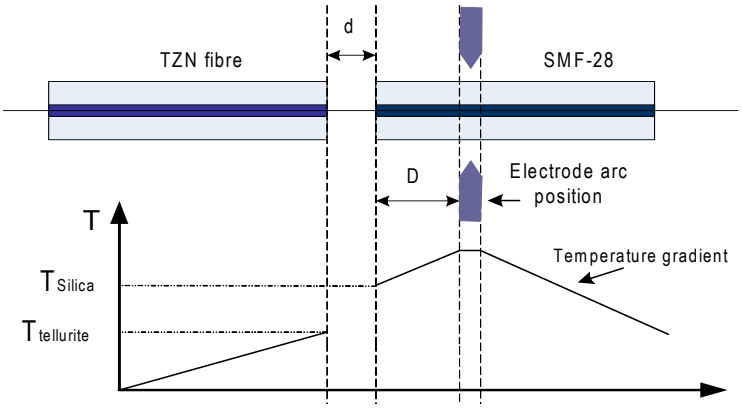

Fig.3.1 Configuration of asymmetric fusion splicing method for soft glass fibre with silica fibre

In this technique, the arc electrodes are displaced a distance D along the silica fiber from the gap between the two fibres to be spliced. With a reduced arc power setting, this asymmetric configuration does not soften the silica fibre, but sufficient heating occurs to heat the tellurite or germanate glass fibre above its softening temperature. In this condition, the silica end of the fibre junction is hotter than the tellurite or germanate glass fibre end. This temperature gradient serves to melt the tellurite or germanate glass fibre on contact with the silica fibre thereby making a good splice when the fibres are moved towards one another.

In our experiment, a manual BFS-50 Single Mode Fusion Splicer was used. The electrode arc was aligned over the silica fibre, and displaced from the end face of the silica fibre by a distance of around 600μm. The gap between two fibres was 16μm,

which further increased the temperature gradient between two fibres and providted a more uniform heating to the tellurite or germanate fibre. By optimising the splicing parameters, such as arc current and arc time, the tellurite or germanate single mode and multimode fibre were spliced to the silica fibre using this asymmetric fusion splicing method, as shown in figure 3.2. The splicing settings using manual BFS-50 Single Mode Fusion Splicer are given in table 3.1.

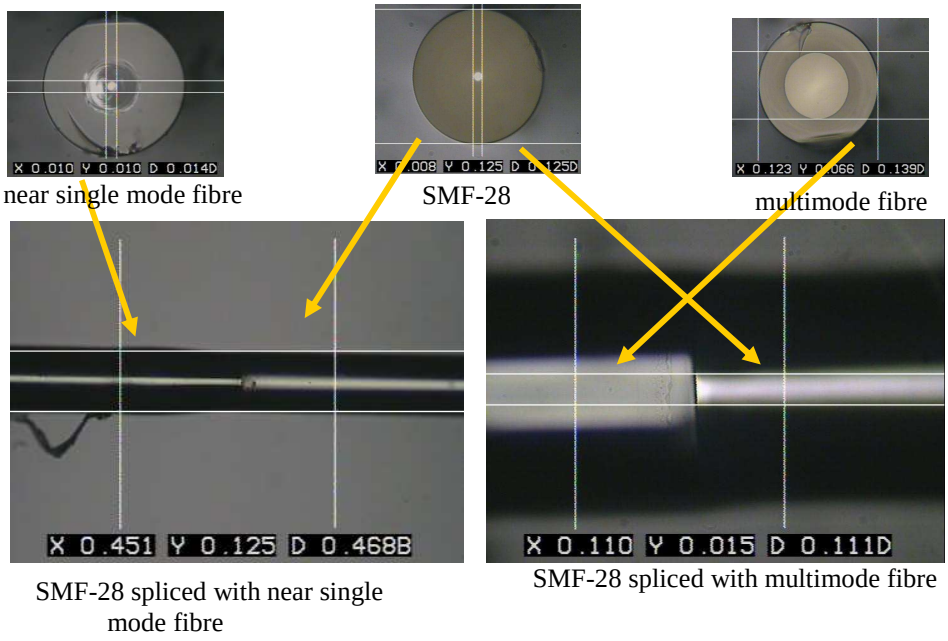

Fig.3.2. Splicing figure of tellurite near single mode and multimode fibre with SMF-28

Table 3.1 BFS-50 Single Mode Fusion Splicer settings for tellurite or germanate glass fibre splicing with fused silica fibre

Initial speed with current	10µm/s @ 5mA
Final speed with current	10µm/s @ 5mA
Overrun distance with time	7µm @ 0.4s
Heater temperature	80^{o}C
Heater time	10s

In order to verify the splicing effect of this asymmetric method, the splicing loss and the attenuation of tellurite fibre were measured using cut-off technique, as shown in figure 3.3.

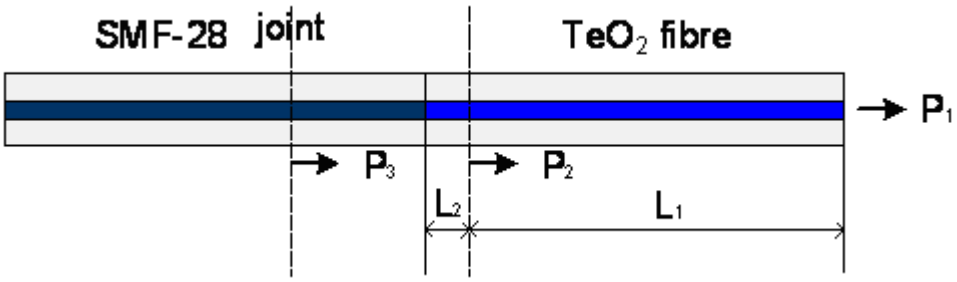

Fig.3.3. Principle of splicing loss measurement

The light is coupled into the silica fibre and tellurite fibre. At first, we measure the output power P_1 from tellurite fibre, then cut it down near the splicing joint with L_1 length and measure the output power P_2; after that, we cut down the fibre again near the splicing joint in the silica fibre side, and measure the output power P_3. Considering the reflection from tellurite fibre to air, from silica fibre to tellurite fibre, and from silica fibre to air, the splicing loss and attenuation of tellurite fibre will be obtained from the fibre attenuation calculation equation (2.17).

The reflection from tellurite fibre to air, silica fibre to tellurite fibre and silica fibre to air are calculated as follows [3.36]:

$$R_{tzn\text{-}air}=[(n_{tzn}-n_{air})/(n_{tzn}+n_{air})]^2=11.11\% \quad (3.1)$$

$$R_{silica\text{-}tzn}=[(n_{silica}-n_{tzn})/(n_{silica}+n_{tzn})]^2=3.11\% \quad (3.2)$$

$$R_{silica\text{-}air}=[(n_{silica}-n_{air})/(n_{silica}+n_{air})]^2=2.78\% \quad (3.3)$$

where the refractive index of tellurite glass fibre is measured to be 2.03 in section 3.3.3.

Using equation (2.17) and considering the reflection between two medias, the splicing loss of tellurite glass multimode and near single mode fibre with SMF-28 at 1550nm was calculated to be 0.53dB and 0.67dB respectively. The attenuation of tellurite glass multimode and single mode fibre with 20~30cm lengths was also measured using the cut-off technique with values about 10dB/m and 15dB/m respectively and shows good consistent from sample to sample in the measurement.

The measurement values show that the splicing loss of tellurite near single mode fibre with silica fibre is a little bigger than that of tellurite multimode fibre, the

reason for that maybe comes from the alignment accuracy in the splicing processing because the single mode tellurite fibre also has a smaller core of about 10μm, which causes the cladding light existence after splicing. Thus more accurate alignment is required in the splicing process of two single mode fibres.

3.3 Chromatic Dispersion and Refractive Index Measurement

Fibre chromatic dispersion characteristics are important for high-speed transmission systems and dispersion compensation and management, therefore an accurate knowledge of fibre dispersion is essential for new special linear and nonlinear optical devices.

Measurements of dispersion in optical fibres are typically based on pulse broadening. By measuring the time taken for the peak of the pulse to propagate through a known length of optical fibre, the delay time or group delay can be found at a central frequency of a pulse [3.14, 3.15], and the dispersion of the fibre then can be obtained through differentiation of the group delay. This method requires a short optical pulse laser source and a longer length of fibre because the pulse broadening is a function of fibre length and the effect is very small.

In our experiment, a low-coherence Michelson interferometer and Dispersion Fourier Transform Spectroscopy (DFTS) technology [3.16, 3.17] are used to measure the group velocity dispersion in short lengths of tellurite and germanate glass optical fibre. Unlike long (kilometre) lengths of fibre, where the group velocity dispersion can be measured in the time domain by pulse broadening, in shorter (~1m) lengths of fibre the higher time resolution of interferometry is needed. The dispersive Fourier transform spectroscopy (DFTS) we use is sensitive enough to measure the group velocity dispersion of fibres as short as a few millimetres [3.18, 3.19].

3.3.1 Theory

Group Velocity and Material Dispersion

As shown in 2.2.2, when a temporal pulse propagates through a homogeneous medium, it propagates with a group velocity v_g given by the equation

$$v_g = \frac{d\omega}{dk} \tag{3.4}$$

where $k(\omega) = \frac{\omega}{c} n(\omega)$ represents the propagation constant and $n(\omega)$ represents the frequency-dependent refractive index. Thus

$$\frac{1}{v_g} = \frac{dk}{d\omega} = \frac{d}{d\omega}(\frac{\omega}{c} n(\omega)) = \frac{1}{c}(n(\omega) + \omega \frac{dn}{d\omega}) \tag{3.5}$$

Usually one expresses the group velocity in terms of free space wavelength λ_0, which is related to the frequency following the relation $\lambda_0 = \frac{2\pi c}{\omega}$, therefore

$$\omega \frac{dn}{d\omega} = \frac{2\pi c}{\lambda_0}[\frac{dn}{d\lambda_0}(-\frac{2\pi c}{\omega^2})] = -\lambda_0 \frac{dn}{d\lambda_0} \tag{3.6}$$

therefore equation (3.5) can be written as

$$\frac{1}{v_g} = \frac{1}{c}[n(\lambda_0) - \lambda_0 \frac{dn}{d\lambda_0}] \tag{3.7}$$

Thus, the time taken by a pulse to traverse length L of fibre is given by

$$\tau = \tau(\lambda_0) = \frac{L}{v_g} = \frac{L}{c}[n(\lambda_0) - \lambda_0 \frac{dn}{d\lambda_0}] \tag{3.8}$$

If the source is characterized by spectral width $\Delta\lambda_0$, then each wavelength component will traverse with a different group velocity, resulting in temporal broadening of the pulse. This broadening is given by

$$\Delta\tau = \frac{d\tau}{d\lambda_0}\Delta\lambda_0 = -\frac{L}{c}\lambda_0 \frac{d^2 n}{d\lambda_0^2}\Delta\lambda_0 = -\frac{L}{c}(\lambda_0^2 \frac{d^2 n}{d\lambda_0^2})(\frac{\Delta\lambda_0}{\lambda_0}) \tag{3.9}$$

in which the quantity $(\lambda_0^2 \frac{d^2 n}{d\lambda_0^2})$ is dimensionless. The above broadening is referred to as material dispersion and occurs when a pulse propagates through any dispersive medium. Since material dispersion as given by equation (3.9) is proportional to the spectral width $\Delta\lambda_0$ and also to the length L traversed in the medium, it is usually specified in units of picoseconds per kilometer (length of the fibre) per nanometer (spectral width of the source) as follows:

$$D_m = \frac{\Delta\tau}{L\Delta\lambda_0} = -\frac{1}{\lambda_0 c}(\lambda_0^2 \frac{d^2 n}{d\lambda_0^2}) \times 10^9 (ps/km.nm) \tag{3.10}$$

where λ_0 is measured in micrometers and c=3×10^5 km/s.

Equation 3.10 can also be written as

$$D_m = -\frac{2\pi c}{\lambda_0^2}\frac{d^2\beta}{d\omega^2} \tag{3.11}$$

When $\frac{d^2\beta}{d\omega^2}$ >0, it is a positive dispersion and the frequency at a fixed position z increases linearly with time (a positive linear chirp); on the other hand, $\frac{d^2\beta}{d\omega^2}$ <0, it is a negative dispersion, and the pulse frequency will decrease with time as it passes an observer at z (a negative chirp). So the definition of dispersion derived from $\frac{d^2\beta}{d\omega^2}$ has a sign opposite to the definition from D(λ) in equation 3.11, and we should be aware of which one of the two parameters is being considered when the sign of the dispersion is stated.

Dispersive Fourier Transform Spectroscopy

Low coherence interferometric techniques have been reported for reflectivity and group delay measurements [3.20] and for differential phase measurements [3.21]. The measurement technique used for group delay measurements is based on a Michelson interferometer; complex reflectivity measurements of optical fibres have also been demonstrated using a low coherence interferometric technique known as dispersive Fourier transform spectroscopy (DFTS) [3.22]. This technique is an adaptation of Fourier transform spectroscopy. Fourier transform spectroscopy is a measurement technique whereby spectra are collected based on measurements of the coherence of a radiative source, using time-domain or space-domain mesurements of the electromagnetic radiation or other type of radiation. The dispersive sample to be measured is placed in one arm of the interferometer; as the optical path difference is scanned, interference fringes are recorded when the arms are balanced to within the coherence length of the illuminating source. However there is no longer a unique zero optical path difference for each wavelength in the source spectrum as in FTS, but the dispersion of the sample introduces a wavelength dependent phase term. The amplitude of the transmission or reflection of the sample can also be wavelength dependent. Therefore the interferogram is no longer symmetric with a maximum at the zero optical path difference point as in FTS, but is now asymmetric due to the wavelength dependent transmission or reflection amplitude and the dispersion of the sample. The

interferogram is therefore encoded with the complex transmission or reflection spectrum of the sample and direct measurements of the amplitude and phase of the spectra can be obtained by Fourier transformation of the recorded interferogram as a function of the OPD [3.23]. The magnitude of the Fourier transform provides the amplitude spectrum and argument provides the phase measurement. This is an established spectroscopic measurement technique and has been extensively reviewed by Parker [3.24]. Examples of recent applications of this technique include dispersion measurement of water from 0.45μm to 1.3μm [3.17] and group velocity dispersion of photonic crystal fibre [3.18].

The advantages of this technique are similar to Fourier transform spectroscopy: reflection DFTS provides simultaneous measurement of the amplitude and phase reflection coefficient of the material being measured. The dispersion of the sample is directly encoded in the recorded interferogram and can be obtained by using a complex Fourier transform. This technique will be investigated in a low-coherence Michelson interferometer to measure the dispersion of optical fibre in this section 3.3.

DFTS can be setup as follows: Consider a low coherence source with spectrum $G(\omega)$ launched into a Michelson interferometer, where a beamsplitter amplitude divides the broadband light to a reference and measurement arm with amplitude transmission coefficients $T_R(\omega)$and $T_M(\omega)$, respectively. These beams propagate in each arm and are reflected back along their paths by the end-mirrors; they recombine at the beamsplitter and are directed to a photodetector.

Scanning one arm by the addition of a variable delay τ, we obtain an interferogram at the photodetector when the path lengths are balanced to within the coherence length of the source. In the case where there is no detected sample in one interferometer arm and the transmission coefficients are identical between the interferometer arms, a symmetric interferogram is produced as all the Fourier components of the recombining beams are in phase. Replacing the end-mirror in the measurement arm with a sample, no longer produces a symmetric interferogram. The interferogram no longer has a unique position corresponding to zero optical path difference as the sample introduces a frequency dependent optical path imbalance and thus produces an asymmetric interferogram as follows:

$$I(\tau) = I_R + I_M + 2\,\mathrm{Re}[\Gamma_{RM}(\tau)] \tag{3.12}$$

where the mutual coherence function $\Gamma_{RM}(\tau)$ is

$$\Gamma_{RM}(\tau) = \frac{1}{2\pi}\int_{-\infty}^{+\infty} T_R^*(\omega) T_M(\omega) G(\omega) \exp(j\omega\tau) d\omega \tag{3.13}$$

The complex cross-spectral density

$$S_{RM}(\omega) = T_R^*(\omega) T_M(\omega) G(\omega) \tag{3.14}$$

can thus be obtained from the inverse Fourier transform of the interferogram. Its phase gives the phase difference between the interferometer arms as a function of ω, from which the difference in dispersion between the arms can be obtained.

In the following sections, we will use the low-coherence Michelson interferometer and DFTS technology to measure the chromatic dispersion and refractive index of tellurite and germanate glass optical fibres.

3.3.2 Low-Coherence interferometer experimental setup

The experimental arrangement for the shorter length fibre dispersion measurement is shown in figure 3.4, which was previously set up and used in earlier experiments by a lab colleague.

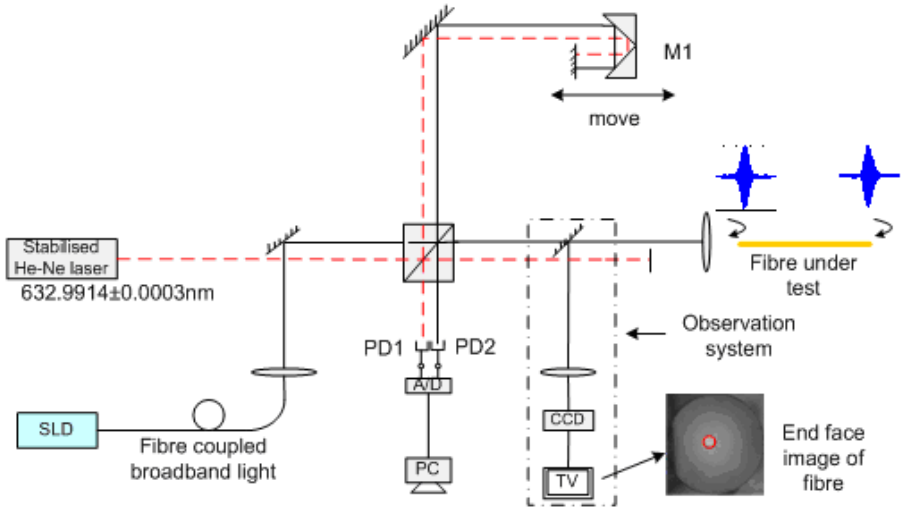

Fig.3.4 Configuration of low-coherence interferometer: HeNe laser with stabilized frequency for calibration measurement

The broadband light is launched into a Michelson interferometer via singlemode fibre to ensure good spatial filtering. The light is divided into the measurement arm and reference arm by an unpolarising glass cube. The fibre under test is placed in the measurement arm. From figure 3.5 (a) the tellurite singlemode fibre image, it was seen

that the fibre core was not accurately located in the fibre centre, which needs accurate alignment for broadband light coupling into the core maximally each time. To address this problem, an observation system was designed, which was formed by a lens with focal length of 200mm, a CCD camera and display screen. When the test fibre was adjusted to a position where the light is effectively coupled into it which is justified using the detector and oscilloscope, the fibre image position on the display screen was recorded at the same time. According to the recorded fibre image position on the display screen, we can easily adjust the test fibre position each time to get maximum light coupling effect.

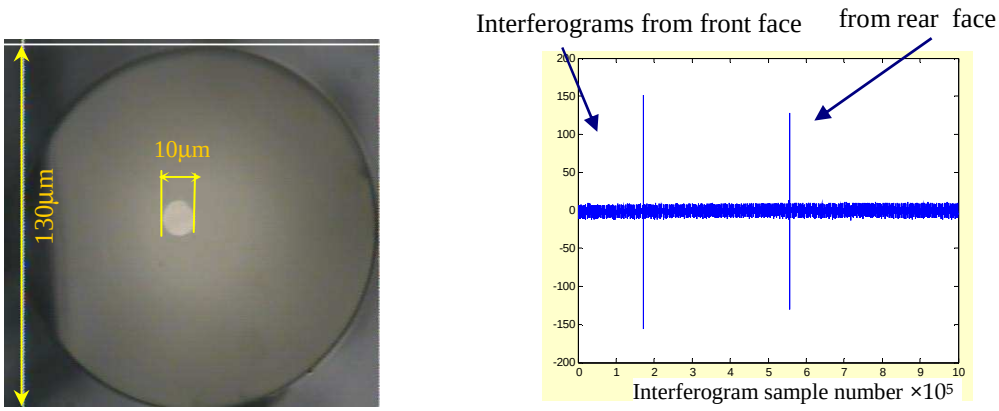

(a) (b)

Fig. 3.5 Tellurite singlemode fibre surface image (a) and interferograms from the fibre front and rear face (b)

The interferometer is balanced when the scanning path length is equivalent to the path length of the front face of the fibre, and an interferogram is recorded; a second peak in the interferogram is observed when the scanning path length is equivalent to the path length to the rear face of the fibre, as shown in figure 3.5 (b). In this case the interferogram is modified by the fibre dispersion. Comparing these two interferograms (front face and back face) allows the dispersion to be measured [3.18], and the separation of these two interferograms gives the effective refractive index of the fibre sample.

A HeNe laser beam with a stable mean frequency [3.25] propagated parallel to the beam from the broadband light source, and was used to calibrate the scan to obtain broadband light interferograms sampled at even intervals of group delay, regardless of

fluctuations in the scan speed. The optical path difference calibration can be performed by simultaneously sampling a reference monochromatic interferogram as well as the low coherence interferograms, as shown in figure 3.6.

3.3.3 Refractive index measurement

As introduced above, the separation of two interferograms from front and rear face of fibre can be used to measure the effective refractive index of fibre. The principle diagram for the fibre refractive index measurement is shown in figure 3.6.

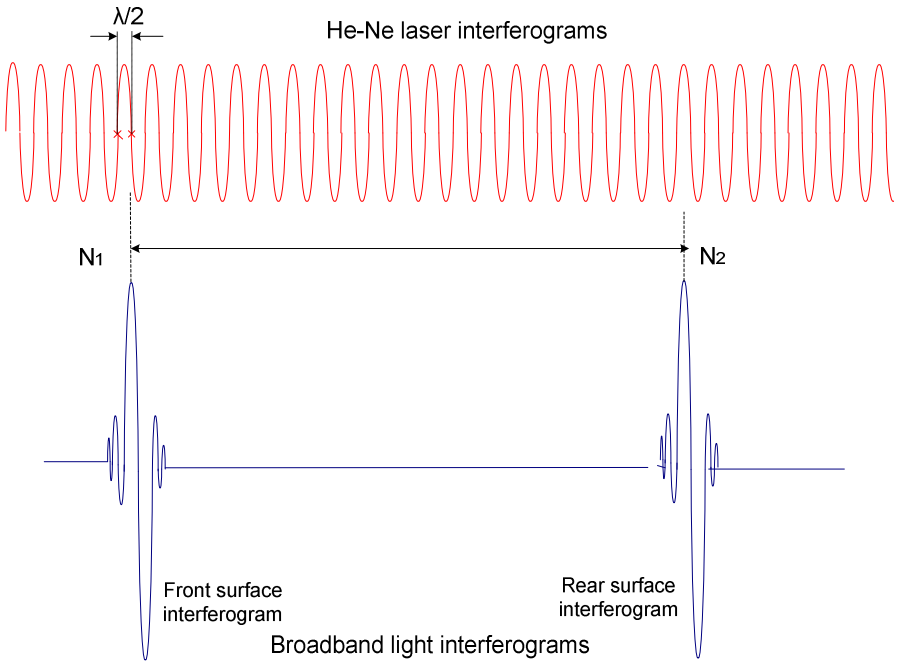

Figure 3.6 Measurement principle of fibre refractive index using HeNe laser interferograms and broadband light interferograms from front and rear fibre faces

Over the whole optical path difference scan, the high coherence interferogram as reference and the low coherence interferogram are sampled simultaneously at photodiodes PD1 and PD2, then the optical path difference from front and rear face of test fibre can be obtained according to the HeNe laser interferograms, which is equal to the effective optical path of broadband light travelling in the test fibre.

The moving distance of M1 is L, thus the optical path difference from front face and rear face of test fibre equals to $2n_{air}L$, which can be obtained from HeNe laser interferograms,

$$2n_{air} \cdot L = (N_2 - N_1) \times \frac{\lambda}{2} \tag{3.15}$$

where N_1 and N_2 are the zero crossing numbers of HeNe laser interferograms corresponding with the broadband light interferograms from front and rear face of test fibre. The fibre length l is measured by travelling micrometer with accuracy of 0.02mm, and the main error comes from the reading accuracy for this fibre length measurement. The effective optical path of broadband light in test fibre equals to $2n_{fibre}l$. According to $2n_{fibre}l=2n_{air}L$, the effective refractive index of test fibre can be obtained from

$$n_{fibre} = \frac{(N_2 - N_1)}{2l} \cdot \frac{\lambda}{2} \tag{3.16}$$

Using this method, the refractive indices of tellurite and germanate glass optical fibres were measured to be 2.03±0.01 and 1.83 ± 0.01 at 1550nm wavelength, respectively. The refractive index of tellurite bulk glass was also measured with the value of 2.08 ±0.01. The measurement error comes from the fibre length measurement which was read through the travelling micrometer and the accuracy of HeNe laser interferograms numbers corresponding with the broadband light interferograms from front and rear fibre surfaces.

3.3.4 Dispersion Measurement

Using the low-coherence interferometer and DFTS technology, the dispersion of tellurite single mode fibre was measured.

First, the dispersion of SMF-28 silica fibre was measured to verify the setup validity. Figure 3.7 shows the interferograms from SMF-28 fibre and phase change over wavelength.

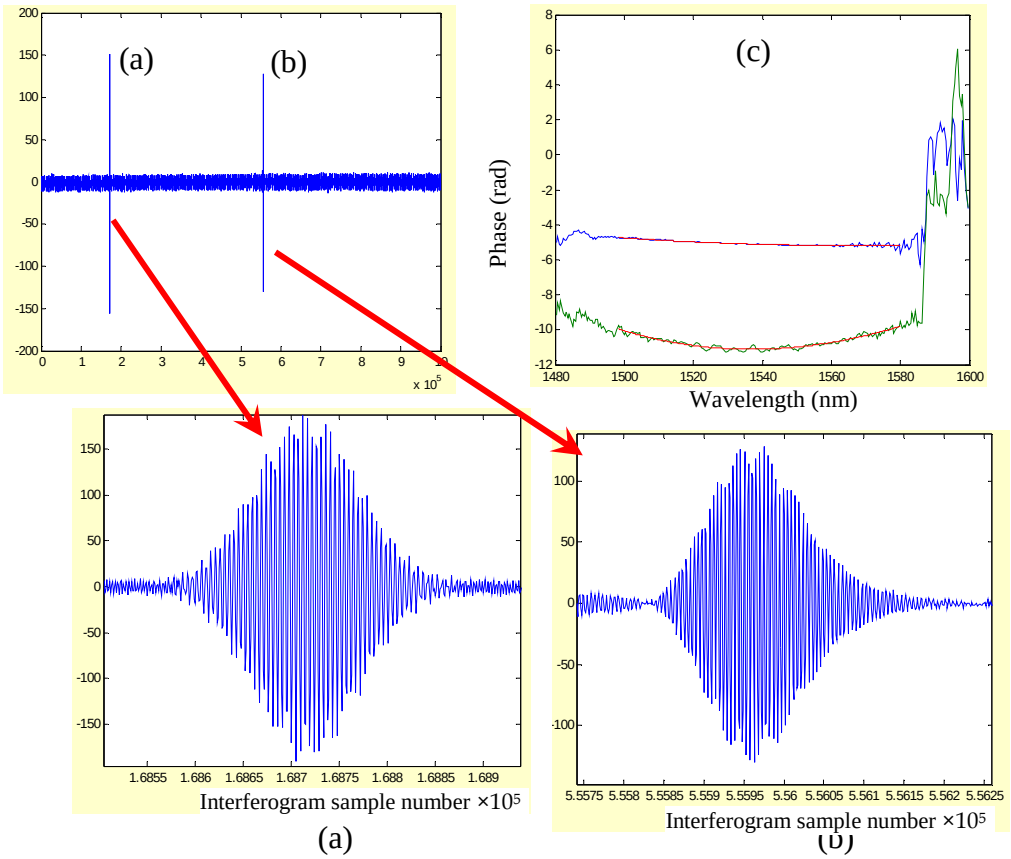

Fig. 3.7 Interferograms from SMF-28 fibre and phase change over wavelength

Figure 3.7 shows the difference of interferograms from the front (a) and rear faces (b) of SMF-28 fibre. The low coherence interferograms from the rear face are asymmetric because of the fibre dispersion. Comparing these two interferograms and analysing the data using the scientific programming language Matlab, the plot of phase change over wavelength (as shown in figure 3.7 (c)) is obtained and which gives the dispersion of SMF-28 fibre, at 1538.3nm is 14.4ps.nm^{-1}.km^{-1}. This experimental measurement value is consistent with the value of 15.39ps.nm^{-1}.km^{-1} from data sheet [3.34], which verified the validity of our experiment setup. The Matlab language code for the signal processing to get the dispersion of the fibre being measured by fourier transform the interferograms is shown in appendix A.

Using the low coherence interferometer, the dispersion of tellurite singlemode fibre at 1538.3nm wavelength was measured to be 101±2 ps.nm^{-1}.km^{-1}, the interferogram from the rear face of fibre and plot of phase change over wavelength are shown in figure 3.8.

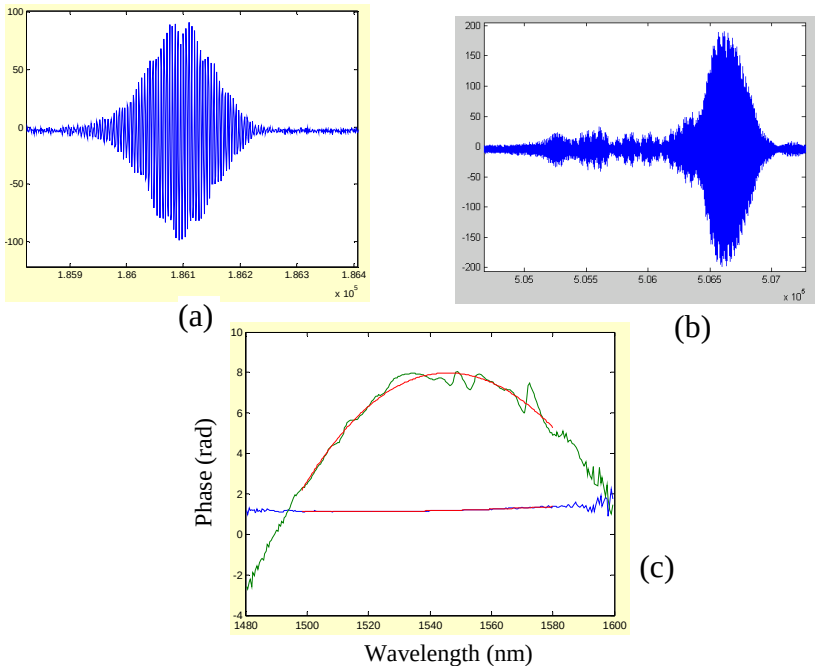

Figure 3.8 Interferograms from front (a) and rear faces (b) of tellurite fibre and plot of phase change over wavelength (c)

Figure 3.9 are the interferograms from the rear face of germanate multimode fibres with length of 41mm and 64mm. The different path lengths amongst the many modes lead to a more complex interferogram, therefore the dispersion of multimode germanate glass fibre can not be deduced using this technique.

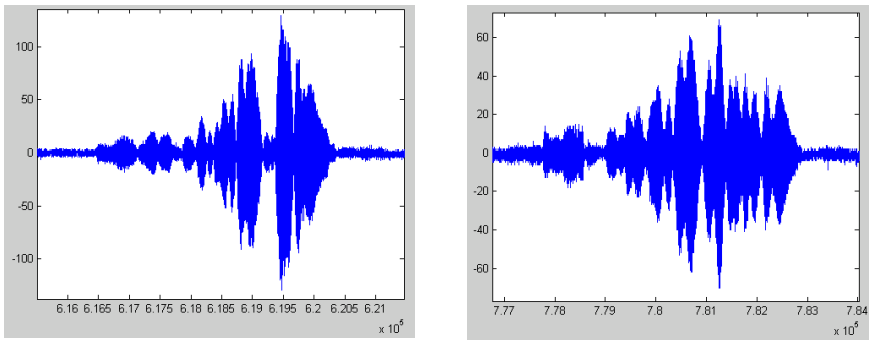

Figure 3.9 Interferograms from back face of germanate multimode fibre with length of 41mm (left) and 64mm (right)

3.3.5 Discussion

Using the low-coherence Michelson interferometer and dispersive Fourier transform spectroscopy (DFTS), the effective refractive index and group velocity dispersion of tellurite and germanate fibres were measured, results as table 3.2. Results show that the tellurite fibre has a relatively large refractive index of 2.03, which is about 40% higher than that of silica fibre 1.46. This high refractive index character offers potential of tellurite glass fibre for stimulated Brillouin amplifiers since the Brillouin scattering coefficient is proportional to the material refractive index raised to the power of 7 [3.26].

Table 3.2 Refractive index and dispersion results of tellurite and germanate fibres

Fibre	Refractive index	Dispersion
SMF 28	1.46 ± 0.01	$14.4\ ps.nm^{-1}.km^{-1}$
Tellurite single mode fibre	2.03 ± 0.01	$101 \pm 2 ps.nm^{-1}.km^{-1}$
Tellurite glass bulk	2.08 ± 0.01	-
Germanate multimode fibre	1.83 ± 0.01	-

3.4 Thermal Sensing Properties of Tellurite and Germanate Glass Fibres

In section 2.4.1 we described that for interferometric sensors the external parameter affects the phase of the light within the fibre and the sensor's output can be measured by detecting the intensity variations. By measuring the temperature-dependent phase change of light propagating through a fibre due to the temperature shift we can investigate the fibre thermal sensing property.

In this section, the thermal sensing properties of tellurite and germanate glass optical fibre are investigated using a fibre Fabry-Perot interferometer. The thermal responses are obtained by measuring the phase sensitivity to temperature of fibre Fabry-Perot (FFP) interferometers formed by splicing tellurite or germanate fibres to singlemode silica fibre. The temperature coefficients normalized to the fiber length L as $\frac{1}{L}\frac{d\phi}{dT}$ rad m^{-1} K^{-1} of these two material fibers have been obtained over a temperature range 280K to 320K, and contributions from the thermal expansion, thermal optical effects and electronic polarizability are discussed in detail. The thermal sensing

properties of these two material fibres were also investigated by measuring the wavelength shift of FBGs in these fibres, and compared with the values from the FFP interferometers.

3.4.1 Fabrication of tellurite or germanate fibre Fabry-Perot cavities

Short length tellurite or germanate FFP cavities were formed by splicing these glass fibres to singlemode silica fibre using an asymmetric fusion splicing method as described in section 3.2. Using a manual BFS-50 Single Mode Fusion Splicer, the tellurite or germanate multimode and singlemode fibres were spliced to the silica fiber with a splice loss of less than 0.53dB, determined by a cut-back technique. Thus the fibre Fabry-Perot cavity was formed between the cleaved end face and the step change in index at the splice, as shown in figure 3.10. Using the refractive index values of tellurite and germanate glass fibres indicated in table 3.2, the expected Fresnel reflection coefficients are calculated to be about 11.11% on the cleaved end face and 3.11% on the splicing face for tellurite FFP cavity, 8.6% on the cleaved end face and 1.6% on the splicing face for germanate FFP cavity respectively. These Fresnel reflection coefficients will in turn determine the visibilities of the FFP cavities expected in the experiment.

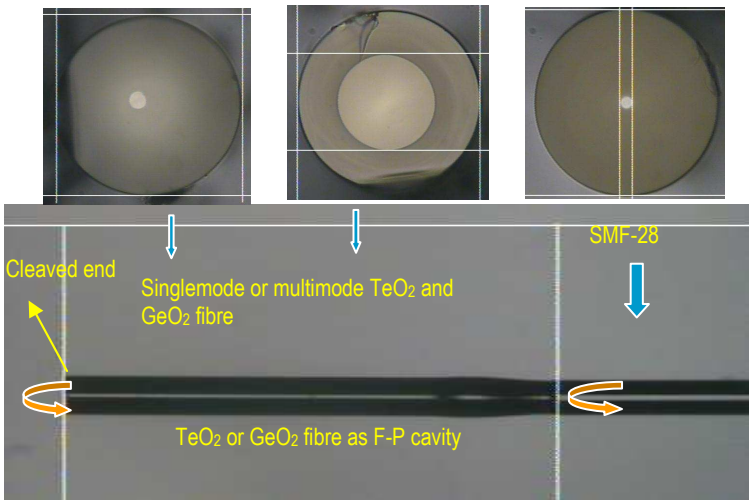

Fig.3.10 Tellurite or germanate fibre Fabry-Perot cavity formed by splicing them with single mode silica fibre

3.4.2 Fabry-Perot interferometer principle and setup

The experiment setup is shown in figure 3.11, with the tellurite (or germanate) fiber spliced to the silica fibre downlead acting as a low finesse Fabry-Perot interferometer.

Broadband light from an erbium-doped amplified spontaneous emission (ASE) source was coupled into the FFP by a 2×2 single-mode fiber coupler. Part of the incident radiation is reflected by the interface between silica and tellurite fibre at the splice, the rest being coupled into the tellurite fibre and a portion reflected by the fibre end face to interfere with the light reflected from the splice. The interferogram is observed using a commercial wavelength meter. Figure 3.12 shows the broadband source spectrum and interference fringes observed. The visibility of fringes of tellurite FFPs is evaluated about 65%.

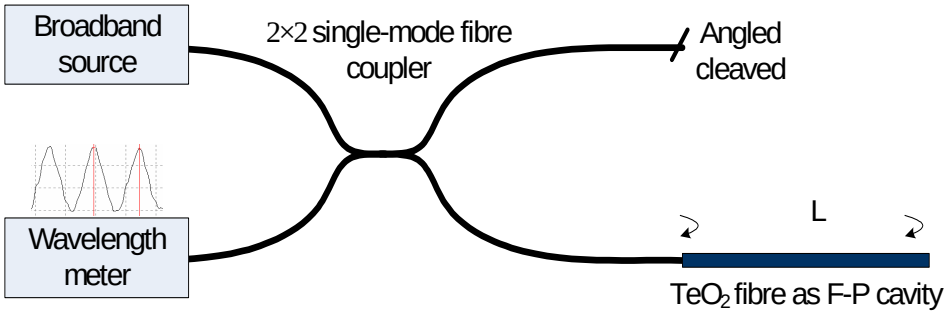

Fig.3.11 Scheme for thermal response experiment of tellurite and germanate fiber Fabry-Perot cavity

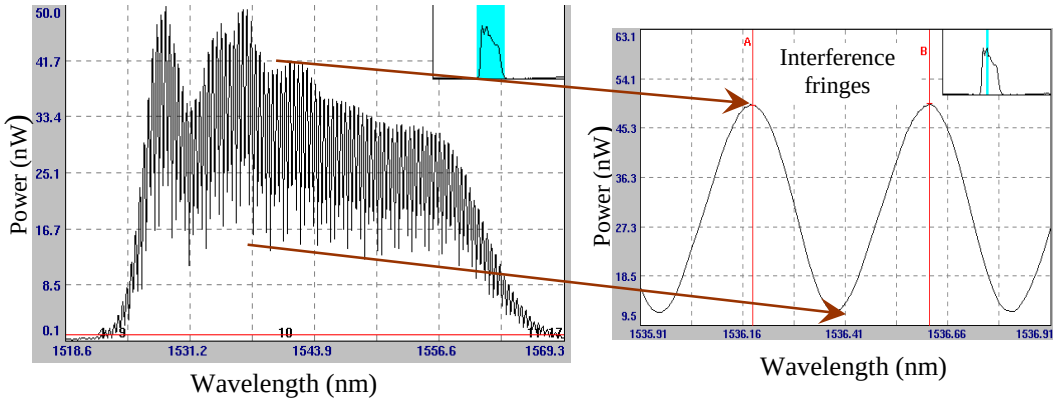

Fig.3.12 ASE source spectrum showing interference fringes of fiber Fabry-Perot cavity

The phase of the interference fringes is given by

$$\varphi = \frac{2\pi}{\lambda} \cdot 2nl \tag{3.17}$$

and the free spectral range [FSR] is expressed in wavelength terms in equation (3.18)

$$FSR \quad = \Delta\lambda \; = \; \frac{\overline{\lambda^2}}{2\,nl} \tag{3.18}$$

where n is the refractive index of the core of tellurite or germanate fibre, $\overline{\lambda}$ is the mean wavelength and *l* is the FFP cavity length. The sensitivity of the phase to temperature is used to determine the thermal response of tellurite and germanate fibre. A fringe shift was observed as the temperature of the fibre was increased, as shown in figure 3.13, caused by changes in the fibre's physical length and core refractive index. Each fringe represents a 2π phase change, thus the phase sensitivity to temperature dφ/dT can be inferred from the slope of the temperature-phase plot.

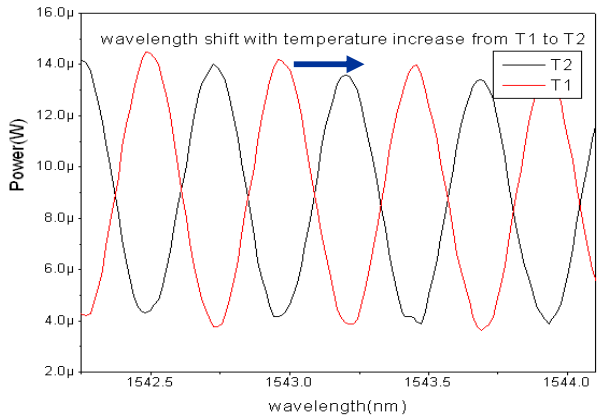

Fig.3.13 Interference fringe shift as temperature is altered

In the experiment, two tellurite single mode and multimode FFPs were fabricated with lengths of 1.42 mm and 8.36 mm respectively. Their free spectral ranges were measured from the reflection spectra using the wavelength meter, and were found to be 0.410 nm and 0.076 nm respectively, as shown in figure 3.14.

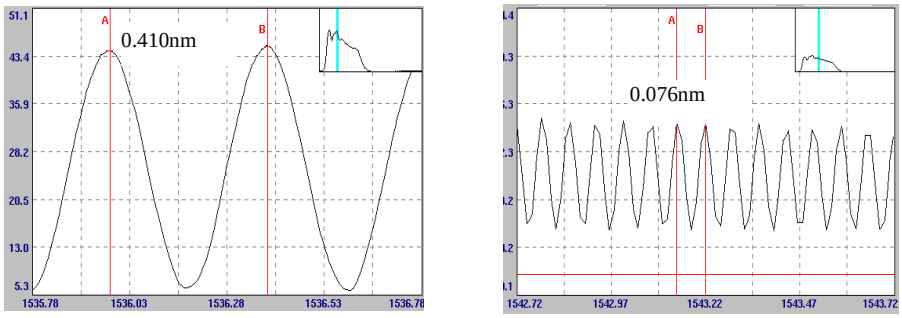

(a) (b)

Fig.3.14. Comparisons of fringes and FSRs for two FFPs of different lengths, (a): 1.42mm, (b): 8.36mm

As well as the direct measurement from the spectrum, the FSR can also be obtained from equation (3.18), provided the FFP length and refractive index are known. Using the refractive index 2.03 for tellurite fibre which was measured independently by a low-coherence interferometer as in section 3.3.3, the FSRs of the FFPs 1.42 mm and 8.36 mm in length were calculated to be 0.411 nm and 0.070 nm respectively, which compares well with the measured values of 0.410 nm and 0.076 nm. Hence the measured free spectral ranges of two different length FFPs were consistent with the values expected from independent determination of the core refractive indices. This consistency also verified the validity of the experiment setup and proved that the light was effectively coupled into the core of singlemode tellurite fibre from the silica fibre splice. From figure 3.14, it also can be seen that it is easier to resolve small spectral changes from a shorter FFP cavity for a given spectrometer resolution, and a short length also ensures a uniform heating effect over the whole length of the test fibre.

Using equation (2.22), the phase sensitivity to temperature of a fibre Fabry-Perot cavity is given by

$$\frac{1}{L}\cdot\frac{d\varphi}{dT}=\frac{2\pi}{\lambda}\left(n\cdot\frac{1}{L}\cdot\frac{dL}{dT}+\frac{dn}{dT}\right)=\frac{2\pi}{\lambda}(n\cdot\alpha+\beta) \qquad (3.19)$$

where $\alpha=(1/L)(dL/dT)$ is the thermal expansion coefficient, and $\beta=dn/dT$ is the thermo-optic coefficient, L equals to double FFP lengths ($2l$) for the reflection case.

When the temperature of fibre is changed, the interference fringes shift as a result of the change in length and refractive index. To determine the sensitivity of the phase to temperature, the FFP was placed in the centre of a temperature controlled plate for uniform heating. The plate was heated/cooled via two cascaded Peltier elements driven from a LFI-3500 series temperature controller. An erbium ASE source with a

total output power of 30mW and a spectral bandwidth of around 35 nm (as shown in figure 3.12) was used. The temperature was varied from 280 K to 320 K at intervals of 1K~2K, and a settling time around 6 minutes was required to allow the plate and FFP to reach thermal equilibrium. At each temperature set-point, the wavelength position of one interference fringe peak was recorded and the temperature was measured at the same time. The fringe shifts were observed and recorded by a WA-7600 wavemeter. Each fringe represents a 2π-phase change, thus phase sensitivity to temperature $d\varphi/dT$ can be inferred from the slope of the temperature-phase plot.

3.4.3 Results

A 1.42 mm length of tellurite singlemode FFP was used to determine the sensitivity of interferometric phase to temperature. By recording the wavelength shift of one interference fringe peak as a function of temperature, and dividing it by the free spectral range expressed in wavelength, a plot of a temperature-phase was obtained and $d\varphi/dT$ was inferred from the slope as shown in figure 3.15(a).

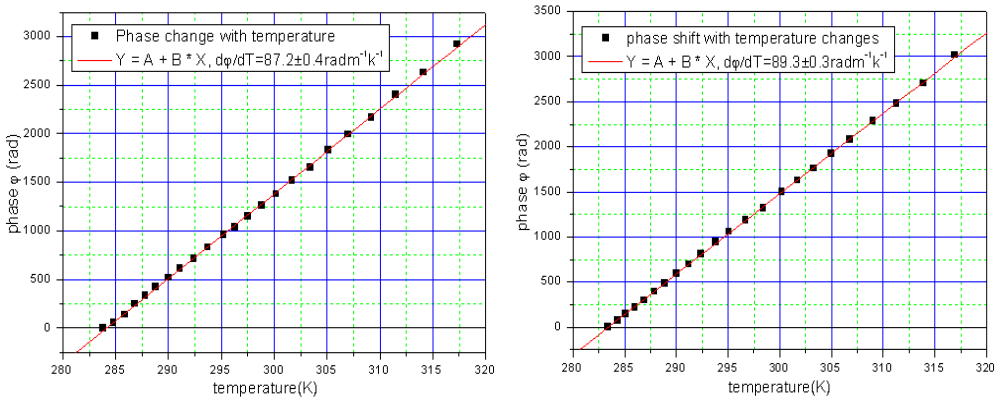

(a) (b)

Fig.3.15. Phase sensitivity to temperature of tellurite singlemode (a) and multimode (b) glass optical fibre at 1536nm wavelength

Figure 3.15(a) shows that phase appears to be linearly proportional to the temperature, and the temperature sensitivity of the tellurite optical fiber was measured to be $d\varphi/dT$=87.2± 0.4 rad m^{-1} K^{-1} at a central wavelength of 1536 nm. In order to verify that the experiment setup was valid and the result meaningful, we repeated the experiment and obtained confirmatory results from a 1.38 mm long multimode tellurite FFP. Temperature sensitivity was dφ/dT=89.3± 0.3 rad m^{-1} K^{-1} at central wavelength of

1536 nm, as shown in figure 3.15(b). These two results show good consistency with each other, and both are bigger than 51.9 rad m^{-1} K^{-1} for silica fibre at 1550nm wavelength [3.27].

Using the same setup and measurement method, the thermal phase sensitivity of germanate fibres 2.88 mm and 1.28 mm in length were measured to be 112.8± 0.5 rad m^{-1} K^{-1} and 116.5± 0.4 rad m^{-1} K^{-1} respectively at central wavelength of 1536 nm, which also showed good consistency with each other, as displayed in figure 3.16 (a, b).

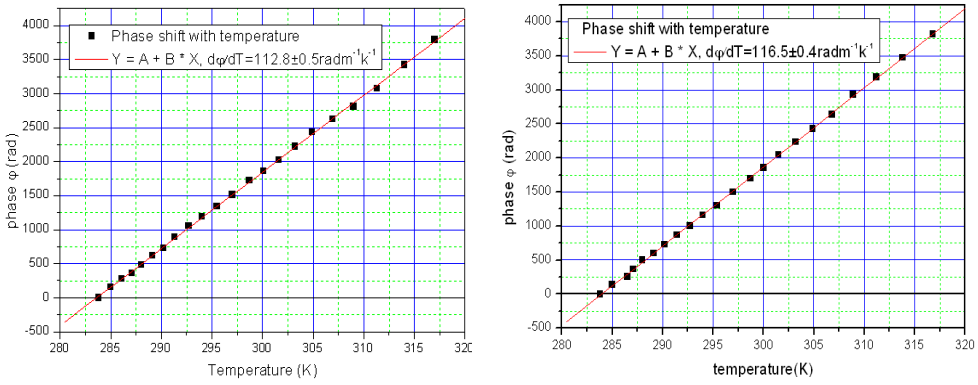

(a) (b)

Fig.3.16 Phase sensitivity to temperature of germinate glass multimode optical fibre with length of 2.88mm (a) and 1.28mm (b)

3.4.4 Discussions

From equation 3.15, it can be seen that the phase sensitivity to temperature is determined by two terms: the first factor describes the contribution from the thermal expansion coefficient, which is normally positive for optical fibre glasses, and the second factor is the contribution from the thermo-optic coefficient.

For tellurite glass fiber, the temperature sensitivity of the optical phase was measured to be about 87.2 rad m^{-1} K^{-1}. Using the value of refractive index n=2.03 measured by the low-coherence interferometer, and the thermal expansion coefficient $\alpha=1.86\times10^{-5}$ $m.K^{-1}$ which was measured using a Dynamic Mechanical Analyser in Leeds University, we find that thermal expansion contributes around 154 rad m^{-1} K^{-1} to the thermal phase sensitivity of tellurite fiber. This implies that the thermo-optic coefficient β of tellurite glass fibre should be negative, reducing the effect of thermal expansion. In this case the experimental result implies that $\beta=-16.4\times10^{-6}$ K^{-1}.

In order to understand the sign of thermo-optic coefficient β, we can use the expression (3.20) which is given by differentiating the Lorentz-Lorenz equation [3.28]

$$\frac{dn}{dT} = \frac{(n^2 - 1)(n^2 + 2)}{6n}(\zeta - 3\alpha) \tag{3.20}$$

in which ζ is the temperature coefficient of the electronic polarizability, α is the thermal expansion coefficient.

Equation 3.20 shows that the thermo-optic coefficient depends on two terms; the first describes the contribution from the thermal expansion coefficient and the second describes the contribution from the temperature dependence of the electronic polarizability. These two terms compete with one another to give positive or negative values of thermo-optic coefficient since the term $(n^2-1)(n^2+2)/6n$ is always positive.

Using equation (3.20), and $\zeta=40.9\times10^{-5}$ K^{-1} at 1550 nm wavelength for tellurite glass ($75TeO_2$-$20ZnO$-$5Na_2O$) [3.29, 3.30], the thermo-optic coefficient of tellurite glass is calculated to be -23.3×10^{-6} K^{-1}, which agrees reasonably well with the negative value of -16.4×10^{-6} K^{-1} from our experimental measurement. The difference between these two β values may be due to the slightly different glass compositions being compared, and also due to the changes in the glass structure during fiber drawing and the stresses induced during the preform fabrication processes [3.31] from bulk glass to fibre.

For the germanate glass fibre, using equation 3.19 and the value of refractive index n=1.83, thermal expansion coefficient $\alpha=10.9\times10^{-6}$ K^{-1}, and thermo-optic coefficient $\beta=9.0\times10^{-6}$ K^{-1} [3.32] for BGG glass with composition of GeO_2-Ga_2O_3-BaO which hold the same main composition GeO_2 compared with our germanate glass fibre GeO_2-PbO-Na_2O-Ga_2O_3, the thermal sensitivity of the optical phase was calculated to be 118.4 rad m^{-1} K^{-1}, which agrees well with our experimental measurement of 116.5 rad m^{-1} K^{-1}.

3.5 Thermal Responses of FBGs in Germanate and Tellurite Fibres

The thermal sensing properties of germanate and tellurite glass fibres were also investigated by measuring the thermal responses of fibre Bragg gratings (FBGs) manufactured in these soft glass fibres by our colleagues in Aston University.

Fibre Bragg grating structures were inscribed in single-core germanate and three-core tellurite glass fibres using 800nm femtosecond laser and phase mask techniques [3.33] at Aston University. The measured thermal responsivities of the 2nd and 3rd order Bragg resonances of germanate fibre at 1540 nm and 1033 nm were 24.71 and 16.80 pm/°C, respectively. The thermal responsivities of tellurite fibre three cores were measured as 20.21, 18.61 and 19.25 pm/°C at wavelength 1676nm, respectively. The wavelength shifts of the Bragg resonances in germanate and tellurite fibres versus the temperature changes are shown in figure 3.17.

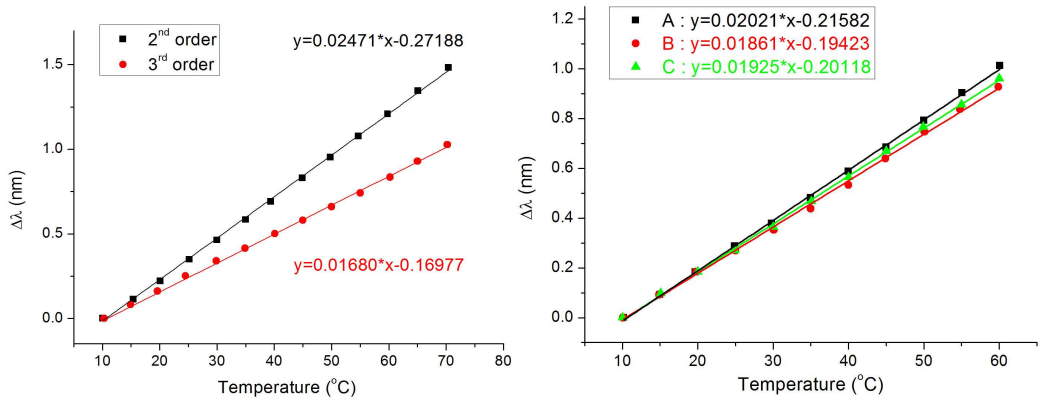

(a) (b)

Fig. 3.17 The wavelength shift of (a) the 2nd and 3rd order resonances of the germanate fibre at~1540 and 1033nm and (b) the 2nd order resonances of the three cores of the three-core tellurite fibre at ~1677nm against temperature change

According to equation (2.23), (2.24), the thermal sensitivity of a fibre Bragg grating can be expressed as:

$$\frac{\Delta\lambda}{\Delta T} = \lambda_B\left(\alpha + \frac{\beta}{n_{eff}}\right) \tag{3.21}$$

where $\alpha = \frac{1}{\Lambda}\frac{d\Lambda}{dT}$ is the thermal expansion coefficient, and $\beta = \frac{dn}{dT}$ is the thermo-optic coefficient.

Combined with the phase sensitivity to temperature of a fibre Fabry-Perot cavity which is described in equation (3.19), the normalized thermal sensitivity of the fibre from F-P interferometer and FBGs can be expressed as:

$$\frac{\lambda}{2n\pi}\cdot\left(\frac{1}{2l}\cdot\frac{d\varphi}{dT}\right) = \frac{1}{\lambda_B}\cdot\left(\frac{\Delta\lambda}{\Delta T}\right) = \alpha + \frac{\beta}{n} \tag{3.22}$$

Using equation (3.22), the normalized thermal sensitivity of germanate fibre from F-P interferometer and FBG measurement is 15.56×10^{-6}/°C and 16.04×10^{-6}/°C, respectively. For tellurite glass fibre, the normalized thermal sensitivity from F-P interferometer and FBG measurement is about 10.76×10^{-6}/°C and 11.34×10^{-6}/°C, respectively. The consistence of the thermal sensitivity results of tellurite and germanate glass fibres from F-P interferometer and FBG measurement verifies the validity of experimental measurement, and the experimental thermal responses of the tellurite and germanate glass fibres are also in reasonable agreement with values calculated using published data for fibre with similar compositions [3.30, 3.32].

3.6 Conclusion

We have described the dispersion character and thermal sensing property of tellurite and germanate glass fibres through experimental measurement. The fibre refractive index and group velocity dispersion have been measured using the low-coherence Michelson interferometer and dispersion Fourier transform spectroscopy technique. An asymmetric fusion splicing technique is described and applied for the splicing of tellurite or germanate glass fibre with silica fibre due to their lower melting temperatures. Then the thermal sensitivity of these two material fibres were investigated by measuring the phase change to temperature of fibre Fabry-Perot interferometers formed by splicing tellurite or germanate glass fibre to singlemode silica fibre using the asymmetric splicing method. Their temperature coefficients of interferometric phase have been measured to be 89.3± 0.3 rad m^{-1} K^{-1} (tellurite) and 116.5± 0.4rad m^{-1} K^{-1} (germanate) at the mean wavelength of 1536nm in the range 280K to 320K. The core refractive indices (2.03 and 1.83) were consistent with the measured free spectral ranges. The thermal sensitivity results of these two material fibres from the F-P interferometer were in good agreement with the values obtained by measuring the wavelength shift to temperature of FBGs on tellurite or germanate glass fibres. The contributions from the thermal expansion coefficient and thermo-optic coefficient to the fibre thermal sensitivity were analysed, and found to be broadly consistent with values for bulk glasses, verifying the negative value of thermo-optic coefficient of tellurite glass fibre which can be attributed to its higher thermal expansion coefficient compared with germanate fibre. Tellurite and germanate glass fibre characterizations and thermal sensing properties compared with fused silica fibre are summarized and shown in table

3.3. From table 3.3, we can conclude that the thermal responses of germanate glass fibre is about 30% larger than that of tellurite glass fibre even though tellurite fibre has a higher thermal expansion coefficient however this effect is offset by the negative thermal optic term. Compared with fused silica fibre, the thermal reponses of tellurite and germanate glass fibres are both higher than that of fused silica fibre. For tellurite fibre the thermal response is about 20% larger than fused silica fibre, while for germanate fibre it is nearly 80% larger than fused silica fibre. Therefore tellurite or germanate glass fibres would be advantages as thermal sensing elements.

Table 3.3 Tellurite and germanate glass fibre characterizations and thermal sensing properties

				Tellurite	Germanate	Fused silica @1550nm
Optical measurement	Refractive index @ 1550nm			2.03	1.83	1.44 [3.27]
	Dispersion *(ps.nm^{-1} .km^{-1})*			101 ± 2	-	15.4 [3.34]
	Thermal response	F-P cavity *(1/L)(dϕ/dT) (rad/m.K)*		89.3± 0.3 @ 1540nm	116.5± 0.4 @ 1540nm	51.9 [3.27]
		FBG $d\lambda_B/dT$ *(pm/K)*		~19 @ 1676nm	~24.7 @1540nm	~13.8 [3.27]
		Normalized thermal response *(/K)*	F-P	10.76×10^{-6}	15.56×10^{-6}	8.89×10^{-6} [3.27]
			FBG	11.34×10^{-6}	16.04×10^{-6}	8.883×10^{-6} [3.27]
Calculation	Thermal expansion coefficient α *(m/K)*			1.86×10^{-5}	10.9×10^{-6}	0.55×10^{-6} [3.34]
	Thermal optic coefficient β *(/K)*			-23.3×10^{-6} [3.30]	9.0×10^{-6} [3.32]	11.6×10^{-6} [3.35]
	F-P cavity *(1/2l)(dϕ/dT) (rad/m.K)*			~60 @1550nm	~118 @1550nm	~50 @1550nm
	FBG $d\lambda_B/dT$ *(pm/K)*			~12 @1676nm	~24.4 @1550nm	~13.5 @1550nm
	Normalized thermal sensitivity *(/K)*			$\sim7.2\times10^{-6}$	$\sim15.8\times10^{-6}$	$\sim8.72\times10^{-6}$

3.7 References

[3.1] K. S. Abedin. *Stimulated Brillouin scattering in single-mode tellurite glass fiber.* Optics Express, Vol. 14, No. 24, pp. 11766-11772, 2006

[3.2] G. Ghosh. *Sellmeier coefficients and chromatic dispersions for some tellurite glasses.* Journal of American Ceramic Society, Vol. 78, pp. 2828-2830, 1995

[3.3] S. H. Kim, T. Yoko, S. Sakka. *Linear and nonlinear optical properties of TeO_2 glass.* Journal of American Ceramic Society, Vol. 76, No. 10, pp. 2486-2490, 1993

[3.4] J. S. Wang, E. M. Vogerl, E. Snitzer. Tellurite *glass: a new candidate for fiber devices.* Optical Materials, Vol. 3, pp. 187-203, 1994

[3.5] S. Shen, A. Jha, X. Liu, M. Naftaly, K. Bindra, H. J. Bookey, A. K. Kar. *Tellurite glasses for broadband amplifiers and integrated optics.* Journal of American Ceramic Society, Vol. 86, No. 6, pp. 1391-1395, 2002

[3.6] K. S. Bindra, H. T. Bookey, A. K. Kar, B. S. Wherrett, X. Liu, A. Jha. *Nonlinear optical properties of chalcogenide glasses: observation of multiphoton absorption.* Applied Physics Letter, Vol. 79, No. 21, pp. 1939-1941, 2001

[3.7] T. Uemura, K. Nishida, M. Sakakida, K. Ichinose, S. Shimode, M. Shichiri. *Non-invasive blood glucose measurement by Fourier transform infrared spectroscopic analysis through the mucous membrane of the lip: application of a chalcogenide optical fiber system.* Frontiers Medical & Biological Engineering, Vol. 9, pp. 137-153, 1999

[3.8] J. Mulrooney, J. Clifford, C. Fitzpatrick, E. Lewis. *Detection of carbon dioxide emissions from a diesel engine using a mid-infrared optical fibre based sensor.* Sensors and Actuators A: Physical., Vol. 136, pp. 104-110, 2007

[3.9] A. Mori, H. Masuda, K. Shikano, M. Shimizu. *Ultra-wide-band tellurite-based fiber Raman amplifier*. Journal of Lightwave Technology, Vol. 21, pp. 13100-13106, 2003

[3.10] A. Céreyon, B. Champagnon, V. Martinez, L. Maksimov, O. Yanush, V. N. Bogdanov. *$xPbO\text{-}(1\text{-}x)GeO_2$ glasses as potential materials for Raman amplification*. Optical Materials, Vol. 28, pp. 1301-1304, 2006

[3.11] A. Jha, S. Shen, M. Naftaly. *Structural origin of spectral broadening of 1.5-μm emission in Er3+-doped tellurite glasses.* Physics Review B: Condensed Matter, Vol. 62, No. 10, pp. 6215-6227, 2000

[3.12] V. V. Ravi Kanth Kumar, A. K. George, J. C. Knight, P. St. J. Russell. *Tellurite photonic crystal fiber*. Optics Express. Vol. 11, No. 20, pp. 2641-2645, 2003

[3.13] S. Jiang, J. Wang. *Method of fusion splicing silica fiber with low-temperature multi-component glass fiber*. United States Patent, Patent No. US 6, 705, 771 B2, Mar. 2004

[3.14] L. G. Cohen, P. Kaiser, C. Lin. *Experimental techniques for evaluation of fiber transmission loss and dispersion.* Proceeding of IEE, Vol. 68, pp. 1203-1209, 1980

[3.15] T. Kanada, D. L. Franzen. *Single-mode fiber dispersion measurements using optical sampling with a mode-locked laser diode*. Optics Letters, Vol. 11, No. 5, pp. 330-332, 1986

[3.16] D. Mogilevtsev, T. A. Birks, P. St. J. Russell. *Group-velocity dispersion in photonic crystal fibres.* Optics Letters, Vol. 23, No. 21, pp. 1662-1664, 1998

[3.17] A. G. V. Engen, S. A. Diddams, T. S. Clement. *Dispersion measurements of water with white-light interferometry*. Applied Optics, Vol. 37, No. 24, pp.5679-5686, 1998

[3.18] M. J. Gander, R. McBride, J. D. C. Jones, D. Mogilevtsev, T. A. Birks, J. C. Knight, P. St. J. Russell. *Experimental measurement of group velocity dispersion in photonic crystal fibre*. Electronics Letters, Vol. 35, No. 1, pp. 63-64, 1999

[3.19] L. G. Cohen, J. Stone. *Interferometric measurements of minimum dispersion spectra in short lengths of single-mode fibre.* Electronics Letters, Vol. 18, No. 13, pp. 564-566, 1982

[3.20] M. Volanthen, H. Geiger, M.J. Cole, R.I. Laming, J.P. Dakin. *Low-coherence technique to characterize reflectivity and time-delay as a function of wavelength within a long-fiber grating.* Electronics Letters, Vol. 32, No. 8, pp. 757-758, 1996

[3.21] I. Petermann, B. Sahlgren, J. Skaar, P.Y. Fonjallaz, R. Stubbe. *Phase distribution measurement of fibre Bragg gratings with white light interferometry.* ECOC'98, Madrid, pp. 399-400, 20-24 September, 1998

[3.22] T. Kitagawa, K. Hattori, M. Yamada, M. Horiguchi, R.K. Hickernell. *Direct dispersion measurement of highly-erbium-doped optical amplifiers using a low coherence reflectometer coupled with dispersive Fourier spectroscopy*. Electronics Letters, Vol. 28, No. 20, pp. 1889-1891, 1992

[3.23] R.J. Bell. *Introductory Fourier Transform Spectroscopy*. Academic Press, New York and London, 1992

[3.24] T.J. Parker. *Dispersive Fourier-transform spectroscopy*. Contemporary Physics, Vol. 31, No. 5, pp. 335-353, 1990

[3.25] *Stabilised HeNe laser systems, Model SL02/1,* SIOS Meβtechnnik GmbH, Armstrong optical, UK

[3.26] D. Cotter. *Observation of stimulated Brillouin scattering in low-loss silica fiber at 1.3μm*. Electronics Letters, Vol.18, pp. 495-496, 1982

[3.27] Gordon. M. H. Flockhart. Thesis: *Interferometric interrogation of optical fibre Bragg grating sensors for temperature independent strain measurement.* Heriot-Watt University, 2001

[3.28] L. Prod'homme. *A new approach to the thermal change in the refractive index of glasses*. Physics and Chemistry of Glasses, Vol. 1, No. 4, pp. 119-122, 1960

[3.29] A. Koike, N. Sugimoto. *Temperature dependences of optical path length in fluorine-doped silica glass and bismuthate glass*. Proceeding of SPIE 6116, 61160Y1-61160Y8, 2006

[3.30] S. M. Lima, W. F. Falco, E. S. Bannwart, L. H. C. Andrade, R. C. de Oliveira, J. C. S. Moraes, K. Yukimitu. *Thermo-optical characterization of tellurite glasses by thermal lens, thermal relaxation calorimetry and interferometric methods.* Journal of Non-Crystalline Solids, Vol. 352, pp. 3603-3607, 2006

[3.31] T. Nakai, N. Norimatsu, Y. Noda, O. Shinbori, Y. Mimura. *Changes in refractive index of fluoride glass fibers during fiber fabrication processes.* Applied Physics Letters, Vol. 56, No. 3, pp. 203-205, 1990

[3.32] S. S. Bayya, G. D. Chin, J. S. Sanghera, I. D. Aggarwal. *Germanate glass as a window for high energy laser systems.* Optics Express, Vol. 14, pp. 11687-11693, 2006

[3.33] R. Suo, J. Lousteau, H. Li, X. Jiang, K. Zhou, L. Zhang, W. N. MacPherson, H. T. Bookey, J. S. Barton, A. K. Kar, A. Jha, and I. Bennion. *Fiber Bragg gratings inscribed using 800nm femtosecond laser and a phase mask in single and multi-core mid-IR glass fibers*. Optics. Express, Vol. 17, pp. 7540-7548, 2009

[3.34] Heraeus. *Transparent and opaque fused silica (Datasheet)*. Heraeus Quartz Fused Products Ltd, Surrey KT 14, 7 LE

[3.35] T. Toyoda, M. Yabe. *The temperature-dependence of the refractive-indexes of fused silica and crystal quartz*. Journal of Physics D-Applied Physics, Vol. 16, No. 5, pp. L97-L100, 1983

[3.36] Hecht, Eugene. *Optics* (2nd ed.). Addison Wesley, 1987

Chapter 4

Tellurite and Germanate Glass Fibre Characterisation: Strain Sensitivities

4.1 Introduction

Fibre optic strain sensors have advantages such as insensitivity to electromagnetic field, light weight and minimal intrusiveness compared with conventional strain gauges [4.1, 4.2, 4.3]. This offers great potential for strain monitoring in engineering structures [4.4, 4.5, 4.6, 4.7]. Among these applications, the strain response property of the sensing element is important for the overall sensitivity. The aim of this chapter is to investigate the tellurite and germanate glass fibre strain sensitivity using an interferometric technique as introduced in section 2.4.1. First we investigate the strain sensing properties of tellurite and germante glass fibre using a fibre Fabry-Perot (FFP) interferometer, which is formed by splicing two single mode silica fibres on both sides of tellurite or germanate fibre using an asymmetric splicing method as described in section 3.2. The optical phase sensitivity to strain and Young's modulus of these fibres are obtained through this optical measurement and the mechanical measurement. Then we describe the strain characterization of fibre Bragg grating (FBG) on germanate glass fibre. The measured strain sensing properties of tellurite and germante glass fibre using FFP and FBG show good consistency with each other and compare well with the predicted value from theoretical calculation in section 4.4.

4.1.1 Strain-optic effect

In this section we describe the strain-optic effect in which an applied stress results in the variation of the refractive index of the medium.

The effect of the strain on the optical properties of the medium is described in terms of changes in the index ellipsoid. The index ellipsoid of a medium in the absence of strain is written as [4.8]:

$$\frac{x^2}{n_1^2}+\frac{y^2}{n_2^2}+\frac{z^2}{n_3^2}+\frac{2yz}{n_4^2}+\frac{2zx}{n_5^2}+\frac{2xy}{n_6^2}=1 \tag{4.1}$$

where n_i refers to the refractive indices in different directions of a medium.

If *(x,y,z)* corresponds to the principal axis system, then the index ellipsoid will be simplied to

$$\frac{x^2}{n_1^2}+\frac{y^2}{n_2^2}+\frac{z^2}{n_3^2}=1 \tag{4.2}$$

where n_1, n_2, n_3 are the principal indices of refraction.

In general, a change of refractive index produced by strain is a change in the shape, size and orientation of the index. This change is most conveniently specified by giving the changes in the coefficients of $\Delta(1/n^2)$.

The components of the strain tensor are defined by the following equations:

$$\varepsilon_1=\varepsilon_{xx}=\partial u/\partial x,\varepsilon_2=\varepsilon_{yy}=\partial v/\partial y,\varepsilon_3=\varepsilon_{zz}=\partial w/\partial z$$

$$\begin{aligned}\varepsilon_6&=\varepsilon_{xy}=(\partial u/\partial y)+(\partial v/\partial x)=\varepsilon_{yx}\\ \varepsilon_4&=\varepsilon_{yz}=(\partial v/\partial z)+(\partial w/\partial y)=\varepsilon_{zy}\\ \varepsilon_5&=\varepsilon_{xz}=(\partial u/\partial z)+(\partial w/\partial x)=\varepsilon_{zx}\end{aligned} \tag{4.3}$$

where *u, v, w* represent the displacements along the *x, y* and *z* directions respectively. The first three components ε_1 ε_2 ε_3 define normal strain. They represent change in length per unit length in the three directions specified by the *x, y* and *z* axes. The other three components ε_4 ε_5 ε_6 represent shear strains.

If we neglect the higher-order terms in the strains, on application of mechanical strain, the changes in the coefficient of $\Delta(1/n^2)$ is given by

$$\Delta(1/n^2)_i=\sum_{j=1}^{6}p_{ij}\varepsilon_j;i=1,\cdots\cdots,6 \tag{4.4}$$

where p_{ij} represent the strain optic coefficients. Therefore, the $\Delta(1/n^2)$ are a measure of the relative distortion of the index due to the applied strain.

The form of the strain optic coefficient can be derived from consideration of the symmetry of the medium. For an isotropic material, this can be displayed as

$$p=\begin{bmatrix} p_{11} & p_{12} & p_{12} & 0 & 0 & 0 \\ p_{12} & p_{11} & p_{12} & 0 & 0 & 0 \\ p_{12} & p_{12} & p_{11} & 0 & 0 & 0 \\ 0 & 0 & 0 & (p_{11}-p_{12})/2 & 0 & 0 \\ 0 & 0 & 0 & 0 & (p_{11}-p_{12})/2 & 0 \\ 0 & 0 & 0 & 0 & 0 & (p_{11}-p_{12})/2 \end{bmatrix} \tag{4.5}$$

Thus there are only two independent components p_{11} and $p_{12.}$

If we consider a longitudinal strain ε in the z direction, the strain tensor can be written as

$$\varepsilon_j=\begin{bmatrix} -\mu\varepsilon \\ -\mu\varepsilon \\ \varepsilon \\ 0 \\ 0 \\ 0 \end{bmatrix} \tag{4.6}$$

where μ is the Poisson's ratio, with $\mu = \Delta L_{trans}/\Delta L_{long}$, which is the ratio of transverse over longitudinal extension.

Hence using equation (4.5) and equation (4.6) in equation (4.4), we obtain the change in the refractive index in the *x* and *y* directions as following:

$$\Delta(\frac{1}{n^2})_{x,y} = \varepsilon(1-\mu)p_{12} - \mu\varepsilon p_{11} \tag{4.7}$$

Light propagating in the *z* direction, therefore sees a change in the refractive index of

$$\Delta n = -\frac{1}{2}n^3[\varepsilon(1-\mu)p_{12} - \mu\varepsilon p_{11}] \tag{4.8}$$

4.1.2 Young's modulus

Young's modulus (also called elastic modulus) is a fundamental concept in mechanical and material science. It is known that Young's modulus, E, is a measure of the stiffness of a given material in solid mechanics, which is defined as the ratio of the uniaxial stress over the uniaxial strain in the range of stress in which Hooke's Law

holds [4.9]. Typically Young's modulus can be experimentally measured from the slope of a stress-stain curve created when a tensile testing experiment is conducted on a sample of the material, and which is used in our work to determine the tellurite or germanate glass Young's modulus by a FFP interferometer, as in section 4.2. The Young's modulus of any material which obeys Hooke's law is given by the ratio of stress ($\sigma = F/S$) to strain ($\varepsilon = \Delta l/l$) as:

$$E = \frac{\sigma}{\varepsilon} = \text{constant} \tag{4.9}$$

4.2 Tellurite and Germanate Fibre Strain Phase Sensitivity Using F-P Interferometer

In section 2.4.1 we described an interferometric technique that can be used to measure the strain in a fibre by measuring the change in the optical path length by means of observing an optical interference pattern. There are a number of interferometric techniques which are capable of measuring the strain dependent phase change. In this section, we describe a fibre Fabry-Perot interferometer to investigate the tellurite and germanate glass fibre phase sensing to strain and their Young's modulus.

4.2.1 FFP interferometer principle and setup

FFP cavities were formed by splicing singlemode silica fibres onto both ends of the tellurite or germanate glass fibres using an asymmetric fusion splicing technique as introduced in section 3.2. This technique was also used in the tellurite or germanate glass fibre thermal sensing property measurement in section 3.3. In that section, a short length FFP cavity with 1~2mm length was used in order to get the uniform heating effect, and interference occurs between the light reflected from the splicing interface with the light reflected from the soft glass fibre cleaved end. While for the strain sensing measurement, two single mode silica fibre are spliced with the soft glass fibre on both ends in order to stretch the soft glass fibre easily. In addition, a relatively longer FFP cavity with length of 4~11mm was used for the strain response measurement compared with the thermal sensing measurement, in order to reduce the influence of the glass material character variation and the neck formation at the gap as shown in figure 3.10, which are caused during the splicing process.

The experiment setup is shown in figure 4.1.

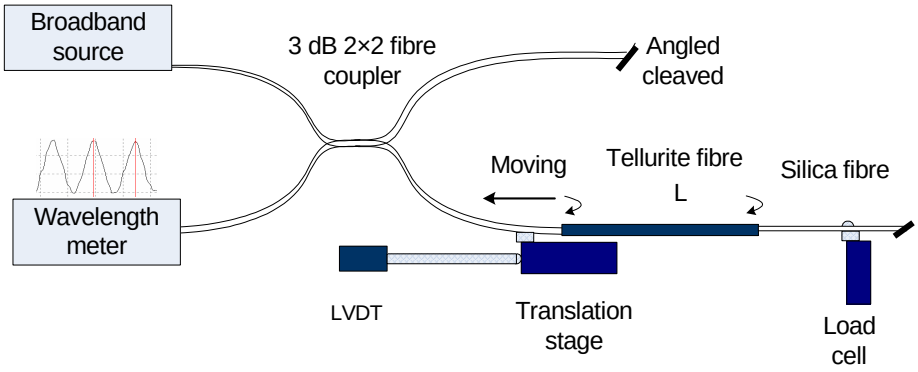

Fig.4.1 Scheme for strain response experiment of tellurite fiber Fabry-Perot cavity

Broadband light from an erbium-doped ASE source was coupled into the FFP by a 2×2 single-mode fibre coupler. The phase of the interference fringes is given by:

$$\phi = \frac{2\pi}{\lambda} \times 2nL \tag{4.10}$$

where n is the refractive index of the core of germanate or tellurite fibre, λ is the mean wavelength and L is the FFP cavity length. The sensitivity of the optical phase to strain is used to determine the strain response of germanate and tellurite fibre.

In the experiment, the germanate and tellurite fibre samples to be strained were configured as a low finesse FFP interferometers with silica fibres spliced on both sides as shown in figure 4.1. The fibre Fabry-Perot cavities were formed between the splices with the step change in index from silica to tellurite or germinate fibres. Using the refractive index values of tellurite and germanate glass fibres indicated in table 3.2, the expected Fresnel reflection coefficients are calculated to be about 3.11% on the splicing face for tellurite FFP cavity, and 1.6% on the splicing face for germanate FFP cavity respectively. These Fresnel reflection coefficients are one of the parameters which determine the visibilities of the FFP cavities expected in the experiment and splicing quality also affects the fringes visibilities.

One side of silica fibre without buffer was attached by glue (no slippage was observed during the experiments due the glue hardness) to a Melles-Griot Nanostepper translation stage which was used to longitudinally strain the germanate or tellurite fibres. A precision displacement sensor (LVDT-Linear Variable Differential Transformer, TESA TRONIC TTD 20, Swiss TESA Made) with ~1μm resolution was used to

measure the movement independently. The other end of silica fibre without buffer was glued to a 2 kg load cell to directly monitor the load applied to the soft glass fibre and a strain gauge amplifier circuit was used to demodulate the load cell. In this manner it was possible to measure the phase shift per unit displacement caused by stretching the germanate or tellurite fibre through the translation stage movement. An erbium amplified spontaneous emission (ASE) source with a total output power of 30mW and a spectral bandwidth of around 35nm was used. At each movement set-point, the wavelength position of one interference fringe peak was recorded and the displacement was measured using LVDT at the same time. The fringe shifts were observed and recorded by a WA-7600 wavemeter.

The amplifier output versus strain is assumed to be linear with the form of:

$$V_i = m_i \cdot \Delta x_i + c_i \tag{4.11}$$

where V_i is the amplifier output, m_i is the gradient of the output versus the Nanostepper displacement Δx_i, and c_i is the intercept. In the case of zero strain $\Delta x_i=0$, $V_i=0$, therefore the intercept $c_i=0$.

As the load cell deflects slightly with applied load and we want to take this effect into account, the load cell deflection with the strain gauge amplifier output was calibrated. We measured the amplifier output V_i versus different load cell deflection Δz to obtain the gradient m_0, which shows the relationship of the load cell deflection Δz with the amplifier output V. The load cell elongation with the amplifier output was calibrated with the value of dimensions gradient m_i $(96.5\pm0.6)\ mV/\mu m$.

The load cell was calibrated by clamping different length of silica fibre without buffer between the load cell and the Nanostepper and measuring the amplifier output versus displacement. The Nanostepper displacement Δx_i in equation (4.11) is the sum of the load cell deflection Δz and the change in fibre length Δl_i. For a single mode silica fibre with given length l_i, the strain added on the load cell can be written as

$$\frac{\Delta l_i}{l_i} = \frac{1}{l_i}(\Delta x_i - \Delta z) = \frac{1}{l_i}\left(\frac{V_i}{m_i} - \frac{V_i}{m_0}\right) = \frac{1}{l_i}\left(\frac{1}{m_i} - \frac{1}{m_0}\right) \cdot V_i \tag{4.12}$$

where m_i is the gradient of the output versus the Nanostepper displacement Δx_i with different silica fibre length l_i, m_0 is the calibrated constant of the load cell elongation with the amplifier output, V_i is the amplifier output of different silica fibre length l_i. By determining m_i from lines of best fit to the load cell output versus the Nanostepper displacement for different silica fibre length l_i, and combining with the load cell

elongation constant m_0, the load cell output to the applied strain using silica fibre was calibrated with the constant of (383±3)$\mu\varepsilon/V$.

The elongation of the tellurite or germanate glass fibre in the strain response measurement with the load cell output then can be obtained from the difference of Nanostepper displacement with the silica fibre elongation and load cell deflection.

4.2.2 Optical measurement results

Using the experimental setup shown in figure 4.1, the phase sensitivity to strain of the tellurite or germanate glass fibre was measured. By recording the wavelength shift of one interference fringe peak as a function of displacement, and dividing it by the free spectral range expressed in wavelength, the plot of germanate and tellurite fibre phase-displacement were obtained and the phase change per unit length elongation of the fibre were derived from the slope of the phase to displacement as shown in figure 4.2 (a) for germanate fibre and figure 4.3 (a) for tellurite fibre. From the measurements of the displacement and the applied force, the Young's modulus of germanate and tellurite fibre were inferred as the gradient of applied stress multiplied by length versus displacement (the ratio of stress to strain as described in equation 4.9), as shown in figure 4.2(b) and figure 4.3(b), in which the elongation displacement of the tellurite or germanate glass fibre in the strain response measurement and Young's modulus measurement were obtained from the difference of Nanostepper displacement with the silica fibre elongation and load cell deflection.

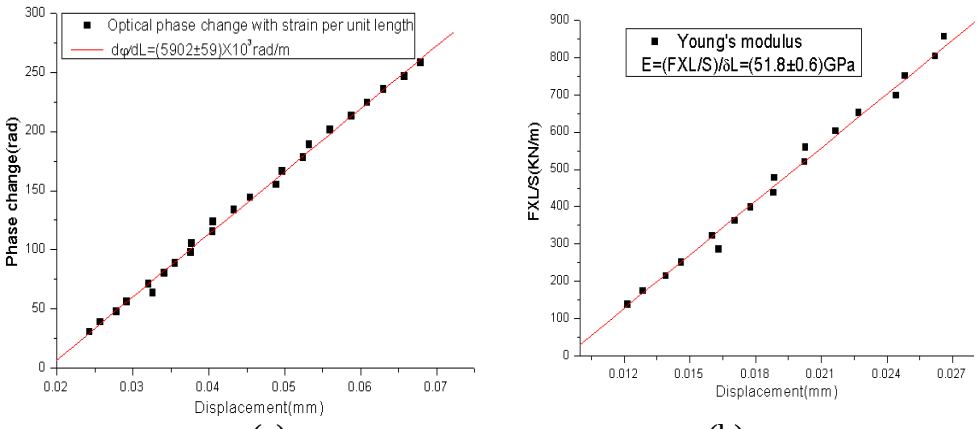

(a) (b)

Fig.4.2 Optical phase change versus elongation of germanate fibre at ~1540nm (a) and (applied stress×fibre length) versus fibre elongation, Young's modulus is equal to the slope of the linear fit (b).

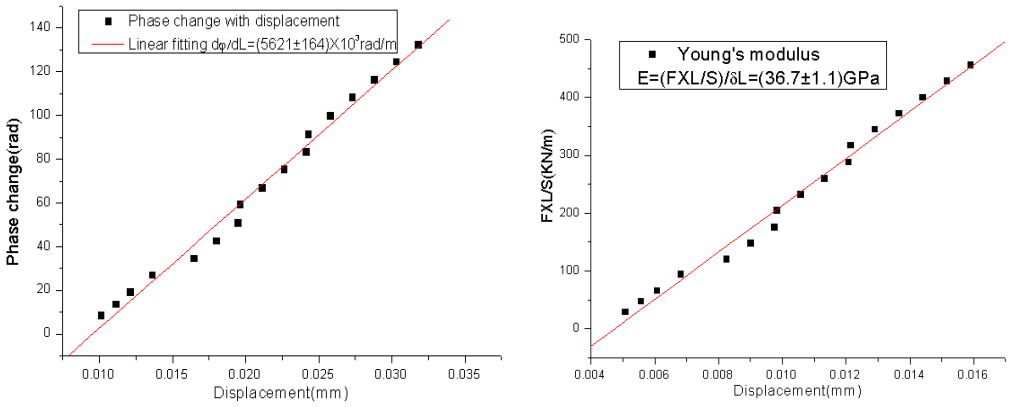

Fig. 4.3 Optical phase change versus elongation of tellurite fibre at ~1540nm (a) and (applied stress×fibre length) versus fibre elongation, Young's modulus is equal to the slope of the linear fit (b).

In the experiment, several lengths of tellurite and germanate glass fibres were used to measure their strain phase response and Young's modulus, and the results are shown in table 4.1 and table 4.2 for tellurite and germanate glass fibre, respectively.

Table 4.1 Tellurite glass fibre strain phase response and Young's modulus with different lengths

Tellurite fibre length	dφ/dL (rad/m)	E=(F×L/S)/dL (GPa)
Length 3.78mm	$(5899\pm142)\times10^3$	37.2±0.9
Length 5.14mm	$(5906\pm116)\times10^3$	40.6±1.1
Length 9.16mm	$(5314\pm59)\times10^3$	34.2±0.4
Length 7.54mm	$(5621\pm164)\times10^3$	36.7±1.1
Length 11.44mm	$(5986\pm138)\times10^3$	37.5±1.3
Average	$(5600\pm200)\times10^3$	37±3

Table 4.2 Germanate glass fibre strain phase response and Young's modulus with different lengths

germanate fibre length	dφ/dL (rad/m)	E=(FXL/S)/dL (GPa)
Length 8.52mm	$(6194\pm46)\times10^3$	52.7±0.5
Length 8.76mm	$(5902\pm59)\times10^3$	51.8±0.6
Length 7.44mm	$(6455\pm53)\times10^3$	54.6±0.5
Average	$(6100\pm300)\times10^3$	53±2

Table 4.1 and table 4.2 show that measurement results of tellurite (germanate) glass fibre strain sensitivity and Young's modulus with different fibre lengths were roughly consistent with each other within the error of about 10%. The average values of the strain sensitivity and Young's modulus for germanate fibre were $(6100\pm300)\times10^3$ rad/m at 1540nm and (53±2)GPa respectively, for tellurite fibre were $(5600\pm200)\times10^3$ rad/m and (37±3)GPa respectively.

4.2.3 Mechanical measurement of Young's modulus

The Young's modulus of tellurite and germanate glass fibre were also obtained using a directly mechanical measurement. The soft glass fibre being measured was glued to the translation stage and load cell directly without light coupled into it. The fibre was stretched through the translation stage movement and moving displacement was measured using the LVDT. Recording the load cell output each time with the translation stage displacement and using equation 4.9, the Young's modulus of tellurite and germanate glass fibre were obtained from the best linear fitting of the load cell output versus the displacement as shown in figure 4.4, and the results with different measurement lengths are shown in table 4.3 and table 4.4 with average values of (38±3) GPa for tellurite and (58±2) GPa for germanate glass fibre respectively, which are roughly consistent with the values from the optical measurement.

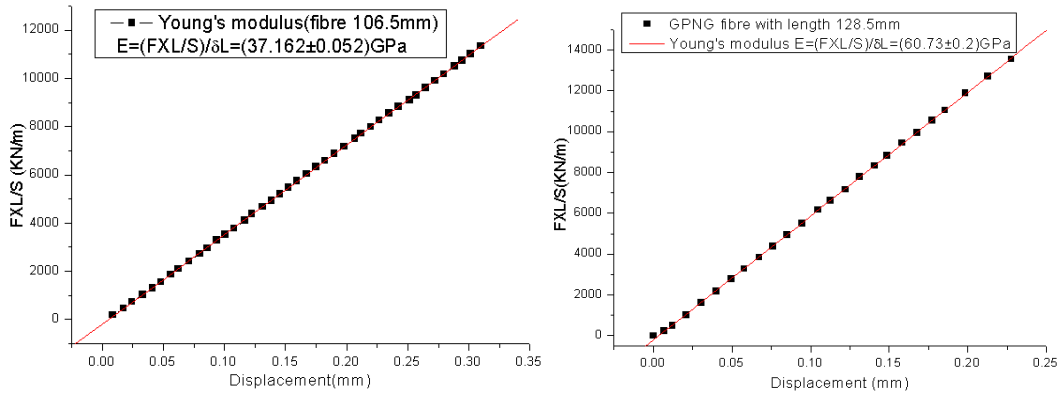

Fig.4.4 Young's modulus of tellurite (a) and germanate (b) glass fibre from direct mechanical measurement

Table 4.3 Tellurite glass fibre Young's modulus with different lengths

Tellurite fibre length	E=(F×L/S)/dL (GPa)
Length 87mm	40.69±0.08
Length 143mm	41.2±0.2
Length 150mm	35.16±0.04
Length 106.5mm	37.16±0.05
Average	38 ±3

Table 4.4 Germanate glass fibre Young's modulus with different lengths

Germanate fibre length	E=(F×L/S)/dL (GPa)
Length 127mm	55.4±0.2
Length 128.5mm	60.7±0.2
Average	58±2

4.2.4 Discussion

The optical phase sensitivity to strain of tellurite and germanate glass fibre were measured as $(5600\pm200)\times10^3$ rad/m $(6100\pm300)\times10^3$ rad/m respectively at 1540nm wavelength by a Fabry-Perot interferometer. Young's modulus of tellurite and germanate were obtained with value of 37GPa and 53GPa respectively using the FFP interferometer, which are roughly consistence with the value of 38GPa and 58GPa from the direct mechanical measurement.

In the mechanical measurement of tellurite glass fibre Young's modulus, we found that the error from the setup is small with value of about 0.1% for each

measurement, while the repeatable measurement using different length fibre shows the result with relatively larger error of about ±8%, the reason may be that the diameter of the fibre being measured is not uniform with length which comes from the fibre drawing process. Figure 4.5 shows the tellurite fibre surface image from different part of the fibre with diameter of 125μm and 134μm respectively.

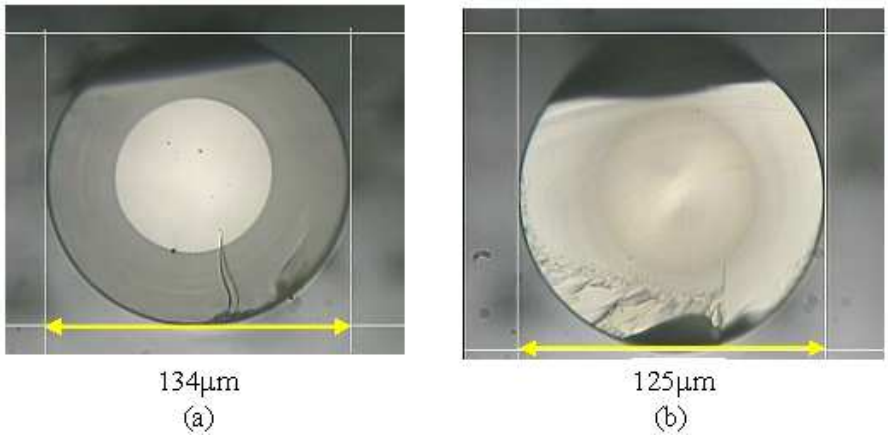

Fig.4.5 Tellurite glass fibre surface image from different part with diameter of 134μm (a) and 125μm (b)

According to equation (4.9), the Young's modulus of the fibre can be obtained from the ratio of stress to strain as following

$$E = \frac{\sigma}{\varepsilon} = \frac{F/S}{\Delta l/l} = \frac{F \cdot l}{S} \cdot \frac{1}{\Delta l} = \frac{F \cdot l}{\pi r^2} \cdot \frac{1}{\Delta l} \tag{4.13}$$

which shows that the Young's modulus is inversely proportional to the square of the fibre radius. Using equation 4.13, the error of the fibre Young's modulus which is caused by the fibre diameter difference with 125μm and 134μm is estimated to be about ±7%. This is a likely explanation for the difference in Young's modulus measurement results.

4.3 Strain Characterization of FBG in Germanate Glass Fibre

Extensive published results indicate that fibre Bragg gratings are promising fibre optic strain sensors. Equation 2.23 states that the centre wavelength of the spectrum returned from the grating depends on the effective refractive index and the refractive periodicity of the grating. Both of these two parameters are influenced by changes in

strain in the fibre. In this section, we describe the strain response of FBG on germanate glass fibre.

4.3.1 FBG fabrication

The FBG structure was produced by colleagues at Aston University. The FBG structure was inscribed in the germanate glass fibre with a core diameter of ~8μm surrounded by a cladding of ~126 μm diameter (as shown in figure 4.6) using 800nm femtosecond (*fs*) laser with peak power intensity in the order of 10^{11} W/cm^2 through a custom-designed phase mask with a period of 1697.33 nm. Due to the high refractive index of the germanate glass fibre, the phase mask was used to *fs*-inscribe 2nd order FBGs around 1500-1800 nm.

The 2nd order Bragg grating spectrum in the germanate fibre at 1540.42 nm with the strength of 6.5 dB and a very weak 3rd order spectrum at 1033.74 nm with the strength of 1.2 dB are shown in figure 4.7. In the following sections, the strain response of the FBG on germanate fibre is measured using the 2nd order Bragg grating spectrum at 1540.42nm wavelength.

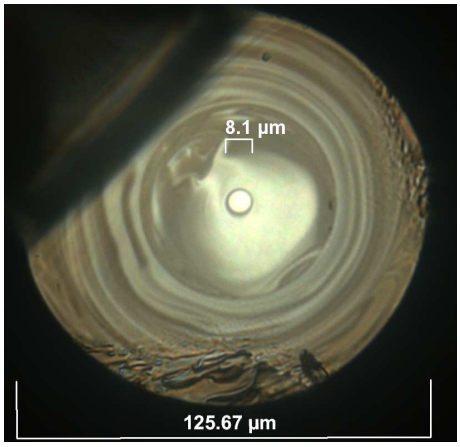

Fig. 4.6 Microscopy images of the cross-sections of germanate single-core fibre

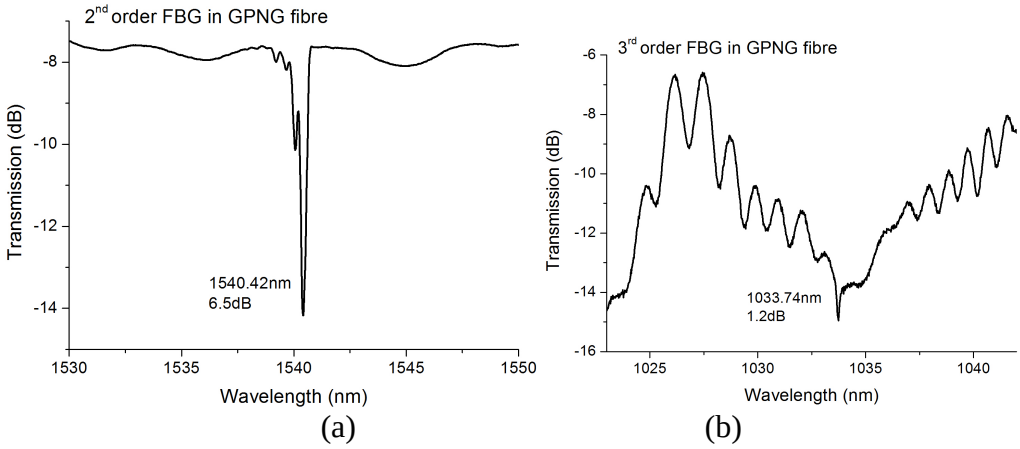

Fig. 4.7 (a) 2nd at 1540.42nm and (b) 3rd order at 1033.74nm FBG spectrums of the grating made in germanate fibre

4.3.2 Experimental work

The germanate glass fibre with FBG was spliced with two single mode silica fibre on two ends. A superluminescent LED source with a central wavelength at 1550nm and a spectral bandwidth of around 45nm was used, as shown in figure 4.8. Using the SLED source, the germanate fibre Bragg grating 2nd order spectrum at 1540nm with 0.7nm bandwidth was observed and recorded by a WA-7600 wavemeter, as shown in figure 4.9.

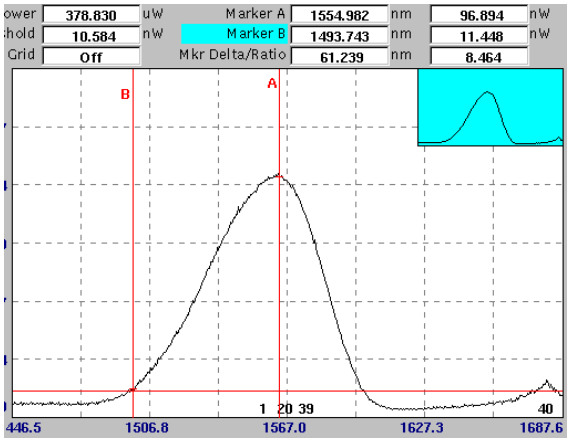

Fig.4.8 Superluminescent LED source spectrum with 45nm bandwidth

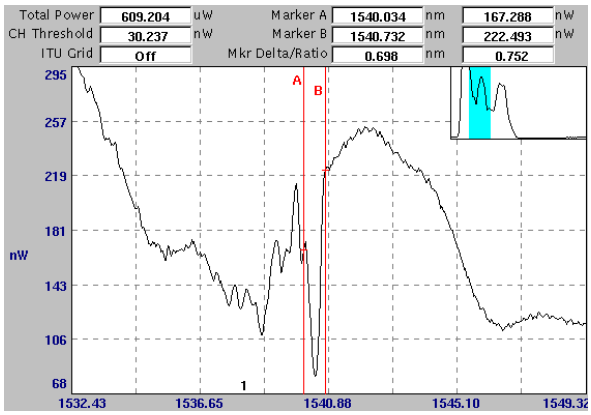

Fig.4.9 2nd order FBG spectrum with central wavelength at 1540.392nm

The experimental setup is shown in figure 4.10. The germanate fibre with FBG was spliced with two single mode silica fibre on both ends. SLED source was coupled into the germanate fibre Bragg grating through the single mode silica fibre. One side of silica fibre without buffer was attached by glue (no slippage was observed during the experiments due to the glue hardness) to a Melles-Griot Nanostepper translation stage which was used to longitudinally strain the germanate fibre Bragg grating. A precision displacement sensor (LVDT) with ~1μm resolution was used to measure the movement independently. The other end of silica fibre without buffer was glued to a 2 kg load cell to directly monitor the load applied to the soft glass fibre and a strain gauge amplifier circuit was used to demodulate the load cell. In this manner it was possible to measure the wavelength shift per unit displacement caused by stretching the grating through the translation stage movement. At each movement set-point, the central wavelength position of the 2nd order grating spectrum was recorded in transmission and the displacement was measured using LVDT at the same time. The wavelength shifts were observed and recorded by a WA-7600 wavemeter.

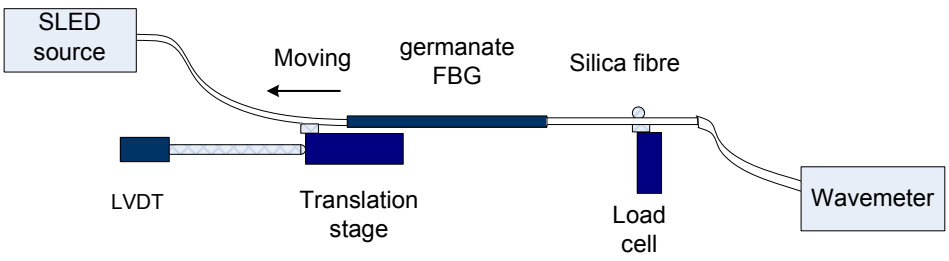

Figure 4.10 FBG on germanate fibre strain response measurement setup

4.3.3 Result

The strain sensitivity of germanate fibre Bragg grating was measured by applying longitudinal strain on it. The strain sensitivity of the 2nd order germanate fibre Bragg resonance at 1540nm was measured to be 1.234±0.003 pm/με, as shown in figure 4.11. In order to verify the measurement validity, the other similar germanate fibre grating strain reponse was also measured with the value of 1.246±0.004 pm/με, these results shows good consistency with each other.

The average strain sensitivity and normalized strain sensitivity of the 2nd order germanate fibre Bragg resonance at 1540 nm were measured to be (1.24±0.04) pm/με and 0.805×10^{-6} /με respectively. Compared with the normalized strain sensitivity result of 0.791×10^{-6} /με from strain applied to the germanate fibre configured as a Fabry-Perot interferometer, it can be seen that the strain responses of germanate glass fibre from the FBG and Fabry-Perot interferometer measurement were consistent with each other with only 1.5% difference in the normalized strain sensitivity.

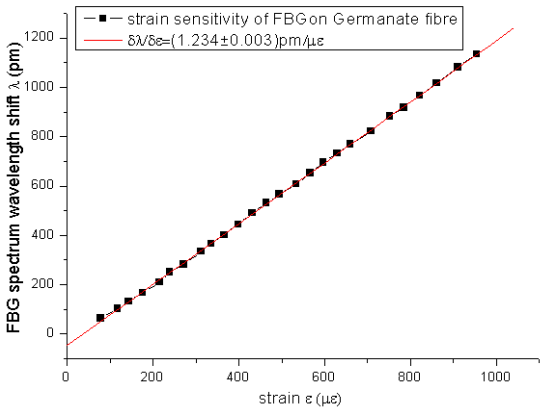

Fig. 4.11 The germanate FBG strain sensitivity at ~1540nm with the value of 1.234±0.003 pm/με

4.4 Theoretical Evaluation of Tellurite and Germanate Glass Fibre Strain Sensitivity

In section 4.2 and 4.3, we described the strain sensitivity of germanate and tellurite glass fibre using the FFP interferometer and germanate fibre Bragg grating. Using a first order theory of elasticity and the photoelastic effect, and assuming that the fibre is elastic and mechanically homogeneous, the strain phase sensitivity of germanate

or tellurite FFP interferometer and the strain response of germanate fibre Bragg grating are theoretically analysed and calculated in this section; the predicted values of germanate and tellurite glass fibre strain response from theoretical calculation using published data for fibres of similar compositions are also compared with the values from our experimental measurement.

4.4.1 Strain phase sensitivity of FFP interferometer

The phase of the light wave after going through the fibre Fabry-Perot interferometer is

$$\phi = 2\pi nL/\lambda = \beta \cdot L \tag{4.14}$$

where β is the propagation constant of the mode in the fibre.

Strain the fibre in the longitudinal direction by an amount ε changes this phase by an amount:

$$\Delta\phi = \beta\Delta L + L\Delta\beta \tag{4.15}$$

The first term represents the physical change of length produced by the strain ε, which is simply written as

$$\beta\Delta L = \frac{2n\pi}{\lambda}\varepsilon L \tag{4.16}$$

The second term is a product of two effects: the stress-optic effect where the strain changes the refractive index of the fibre; and a waveguide mode dispersion effect due to the change in fibre diameter D produced by the longitudinal strain; which can be rewritten as

$$L\Delta\beta = L\frac{d\beta}{dn}\Delta n + L\frac{d\beta}{dD}\Delta D \tag{4.17}$$

Although $\beta = n_{eff}k_0$, where n_{eff} is the effective index which lies between the core and cladding indices, due to the difference of these two values typically only have the order of 1%, thus

$$\frac{d\beta}{dn} = \frac{\beta}{n} = k_0 = \frac{2\pi}{\lambda} \tag{4.18}$$

The second term in equation (4.17) represents the change in the waveguide mode propagation constant due to a change in fibre diameter; this effect is normally negligible because of its relatively small magnitude.

Combining equations (4.16), (4.17) and (4.18) into equation (4.15), we get

$$\Delta\phi = \beta\Delta L + L\Delta\beta = \frac{2n\pi}{\lambda}\varepsilon L + \frac{2\pi}{\lambda}L\Delta n \tag{4.19}$$

This shows that the optical phase change with axial strain is modified due to changes in the physical length of fibre L and the refractive index Δn.

For a homogeneous isotropic medium, the change of the optical indices in the *x* and *y* directions due to longitudinal strain in the *z* direction is given in equation (4.7), and equation (4.8) shows index change of the light propagating in the *z* direction. Therefore, the phase change per unit strain per unit fibre length expresses as

$$\frac{\Delta\phi}{\varepsilon L} = \frac{\Delta\phi}{\Delta L} = \frac{2n\pi}{\lambda} - \frac{1}{2}\cdot\frac{2n\pi}{\lambda}\cdot n^2\left[(1-\mu)p_{12} - \mu p_{11}\right] = \frac{2n\pi}{\lambda}\cdot\left\{1 - \frac{1}{2}n^2\left[(1-\mu)p_{12} - \mu p_{11}\right]\right\} \tag{4.20}$$

where p_{11} and p_{12} are the dimensionless strain optic coefficients, μ is the Poisson's ratio of the fibre material.

4.4.2 Strain sensitivity of fibre Bragg grating

The fibre Bragg grating wavelength is given by:

$$\lambda_B = 2n_{eff}\cdot\Lambda \tag{4.21}$$

where Λ is the FBG's grating period, n_{eff} is the grating's average refractive index.

Equation (4.21) shows that the Bragg grating wavelength depends on the effective refractive index and the refractive periodicity of the grating. Assuming an isothermal condition, when a longitudinal strain ε is applied to the grating, the wavelength shift upon strain changes can be expressed as:

$$\Delta\lambda_B = 2\left[\Delta n\cdot\Lambda + n\cdot\Delta\Lambda\right] \tag{4.22}$$

If we define *l* as the fibre Bragg grating length, given that the path-integrated longitudinal strain is $\varepsilon = \Delta l/l$, and assume $\Delta\Lambda/\Delta l = \Lambda/l$, then we get the change of the refractive periodicity of the grating to be

$$\Delta\Lambda = \frac{\Delta l}{l}\cdot\Lambda = \varepsilon\cdot\Lambda \tag{4.23}$$

Combined with equation (4.8), the change in the optical index due to the path integrated longitudinal strain for a homogeneous isotropic medium, the FBG's grating wavelength shift upon path integrated longitudinal strain expresses as

$$\Delta\lambda_B = \varepsilon\cdot\lambda_B\cdot\left\{1 - \frac{1}{2}\cdot n^2\left[(1-\mu)p_{12} - \mu p_{11}\right]\right\} \tag{4.24}$$

Then the strain sensitivity of FBG on germanate fibre can be written as

$$\frac{\Delta\lambda_B}{\varepsilon} = \lambda_B \cdot \left\{1 - \frac{1}{2} \cdot n^2 \left[(1-\mu)p_{12} - \mu p_{11}\right]\right\} \tag{4.25}$$

4.4.3 Strain sensitivity theoretical evaluation

The strain responses were calculated by using parameters of materials with compositions similar to germanate or tellurite glass fibres. Combined with equation (4.20) and (4.25), the normalized strain sensitivity of the fibre from FBGs and F-P interferometer can be expressed as:

$$\frac{1}{\beta} \cdot \frac{\Delta\phi}{\Delta L} = \frac{1}{\lambda_B} \cdot \frac{\Delta\lambda_B}{\varepsilon} = 1 - \frac{1}{2} \cdot n^2 \left[(1-\mu)p_{12} - \mu p_{11}\right] \tag{4.26}$$

where β is the propagation constant of the mode in the fibre, ε is the longitudinal strain applied to the fibre, μ is Poisson's ratio, p_{11} and p_{12} are the strain-optic coefficients. Using p_{11}=0.225, p_{12}=0.235 and μ=0.232 for germanate glass with composition (mol%) of 30PbO-10Bi_2O_3-60GeO_2 from [4.10], the optical phase change with strain of F-P interferometer and strain sensitivity of FBG at 1540nm can be calculated as 6318×10^3 rad/m and 1.270 pm/με, respectively. The normalized strain sensitivity of germanate glass fiber at 1540nm can be derived with the value of 0.8243×10^{-6} /με, which is 4% higher than the value from experimental measurement. From the above calculation, the experimental strain responses of germanate fibre is in good agreement with values calculated using published data for fibre with similar compositions, and the small difference between these experimental and predicted values may be due to the slightly different glass compositions being compared. Table 4.5 gives the strain properties of germanate and tellurite fibre from optical measurement and theoretical calculation.

Table 4.5 Strain properties of germanate and tellurite fibre from optical measurement and theoretical calculation compared with fused silica fibre

			Germanate fibre @1.54μm	Tellurite fibre @1.54μm	Fused silica @1.55μm
Optical measurement	F-P cavity dϕ/dL (rad/m)		6100×10^{3}	5600×10^{3}	
	FBG $d\lambda_B/\varepsilon$ (pm/με)		1.24	-	1.15 [4.17]
	Normalized strain sensitivity (/με)	F-P	0.817×10^{-6}	0.676×10^{-6}	-
		FBG	0.805×10^{-6}	-	0.74×10^{-6} [4.17]
	Young's modulus (GPa)		53	37	-
Calculation	μ		0.282 [4.10]	0.233 [4.8]	0.17 [4.13]
	p_{11}		0.225 [4.10]	0.0074 [4.8]	0.113 [4.14]
	p_{12}		0.235 [4.10]	0.187 [4.8]	0.252 [4.14]
	dϕ/dL (rad/m)		6318×10^{3}	6018×10^{3}	$\sim4600\times10^{3}$
	$d\lambda_B/\varepsilon$ (pm/με)		1.270	1.090	∼1.24
	Normalized strain sensitivity (/με)		0.8243×10^{-6}	0.7080×10^{-6}	$\sim0.803\times10^{-6}$
	Young's modulus (GPa)		63.64 [4.11]	37.15 [4.12]	72.4 [4.15, 4.16]

From Table 4.5, we conclude that the Fabry-Perot experiments show that the phase change per unit length per unit strain (dϕ/dL) in tellurite fibre is 8.2% smaller than in the germanate fibre; this proportion is consistent with values calculated using published data for fibres of similar compositions, although the absolute values from experiments are ~6.6% lower than those derived from published properties. The difference between these experimental and predicted values may be due to the slightly different glass compositions being compared. Even though tellurite fibre has a higher refractive index, its effect is offset by a larger strain-optic term, which reduces the phase change under strain. However, if we consider the phase change per unit length per unit stress ($\frac{1}{E}\frac{d\phi}{dL}$), the smaller Young's modulus of tellurite fibre compared to germanate leads to a larger response by a factor in the ratio of the measured moduli (53/37) i.e. ~1.4. Hence tellurite fibre would be advantageous as a load sensing element.

4.5 Conclusion

In this chapter, we measured the strain response and Young's modulus of tellurite and germanate glass fibres using fibre Fabry-Perot interferometer and fibre

Bragg grating techniques. The optical phase sensitivity to strain and the normalized strain sensitivity of germanate glass fibre were measured as $(6100\pm300)\times10^3$ rad/m and 0.817×10^{-6} /με respectively at 1540nm by a Fabry-Perot cavity interferometer, which is consistent with the value of 0.805×10^{-6} /με from 2nd order fibre Bragg grating measurement. The Young's modulus was measured to be 53GPa. The strain sensitivity and Young's modulus of tellurite fibre were measured as $(5600\pm200)\times10^3$ rad/m and 37GPa respectively using an FFP interferometer. The strain response of tellurite and germanate glass fibre were also theoretically evaluated, and all the experimental measurement results are in reasonable agreement with values calculated using available published data for glasses of similar compositions.

Compared with fused silica fibre, as shown in table 4.5, it can be seen that the phase change per unit length per unit strain (dϕ/dL) in germanate and tellurite fibre are about 30% larger than that in fused silica fibre, moreover, if we consider the phase change per unit length per unit stress ($\frac{1}{E}\frac{d\phi}{dL}$), the smaller Young's modulus of tellurite fibre compared to fused silica leads to a larger response by a factor of nearly 1.9, then the phase change per unit length per unit stress in tellurite fibre is about 2.5 times of that in fused silica fibre. Therefore tellurite and germinate glass fibres show potential as load sensing element.

4.6 References

[4.1] C. D. Butter, G. B. Hocker. *Fibre optics strain guage*. Applied Optics, Vol. 17, No. 18, pp. 2867-2869, 1978

[4.2] R. M. Measures. *Advances toward fiber optic based smart structures*. Optical Engineering, Vol. 31, No. 1, pp. 34-47, 1992

[4.3] S. F. Masri, M. S. Agbabina, A. M. Abdelghaffar, M. Higazy, R. O. Claus, M. J. Devries. *Experimental-study of embedded fiber-optic strain-gauges in concrete structures*. Journal of Engineering Mechanics- ASCE, Vol. 120, No. 8, pp. 1696-1717, 1994

[4.4] N. Fürstenau, D. D. Janzen, W. Schmidt. *In-flight strain measurements on structurally integrated composite plates using fiber-optic interferometric strain gauges*. Smart Materials & Structures, Vol. 2, pp. 147-156, 1993

[4.5] M. Schmidt, N. Fürstenau, W. Bock, W. Urbanczyk. *Fiber-optic polarimetric strain sensor with three-wavelength digital phase demodulation*. Optics Letters, Vol. 25, No. 18, pp. 1334-1336, 2000

[4.6] R. L. Idriss, M. B. Kodindouma, A. D. Kersey, M. A. Davis. *Multiplexed Bragg grating optical fiber sensors for damage evaluation in highway bridges*. Smart Materials & Structures, Vol. 7, No. 2, pp. 209-216, 1998

[4.7] I. J. Read, P. D. Foote. *Sea and flight trials of optical fibre Bragg grating strain sensing systems.* Smart Materials and Structures. Vol. 10, pp. 1085-1094, 2001

[4.8] A. Ghatak, K. Thyagarajan. *Optical Electronics*. Cambridge University Press, Cambridge, 1989

[4.9] W. F. Magie. *A source book in physics*. McGraw-Hill, New York/London, 1935

[4.10] I. Rabukhin. *Concentration dependences of elastooptic coefficients of germanate glasses containing lead and bismuth oxides*. Glass and Ceramics, Vol. 37, pp. 87-90, 1995

[4.11] S. S. Bayya, G. D. Chin, J. S. Sanghera, I. D. Aggarwal. *Germanate glass as a window for high energy laser systems*. Optics Express, Vol. 14, pp. 11687-11693, 2006

[4.12] E. L. Adawy, R. E. L. Mallawany. *Elastic modulus of tellurite glasses*. Journal of Materials Science Letters, Vol. 15, pp. 2065-2067, 1996

[4.13] N. Lagakos, J. A. Bucaro, J. Jarzynski. *Temperature-induced optical phase shifts in fibers*. Applied Optics, Vol. 20, pp. 2305-2308, 1981

[4.14] A. Bertholds, R. Daendliker. *Determination of the individual strain optic coefficients in single mode optical fibers*. Journal of Lightwave Technology, Vol. 6, No. 1, pp. 17-20, 1988

[4.15] M. Fukuhare, A. Sanpei, K. Shibuki. *Low temperature elastic moduli, Debye temperature and internal dilational and shear frictions of fused quartz*. Journal of Materials Science, Vol. 32, pp. 1207-1211, 1997

[4.16] R. R. J. Maier, W. N. MacPherson, J. S. Barton, J. D. C. Jones, S. McCulloch, G. Burnell. *Temperature dependence of the stress response of fibre Bragg gratings*. Measurement Science & Technology, Vol. 15, pp. 1601-1606, 2004

[4.17] Y. N. Ning, A. Meldrum, W. J. Shi, B. T. Meggitt, A. W. Palmer, K. T. V. Grattan, L. Li. *Bragg grating sensing instrument using a tunable Fabry-Perot filter to detect wavelength variations*. Measurement Science & Technology, Vol. 9, No. 4, pp. 599-606, 1998

Chapter 5

Modelling of Mid-infrared Glass Fibre for Evanescent Field Gas Sensing

5.1 Introduction

The requirement for detecting flammable, explosive and hazardous gas species and concentration is becoming increasingly important for environmental [5.1], industrial [5.2], medical [5.3, 5.4], and safety reasons [5.5]. Conventional electrical sensors are available for some applications, such as SnO_2 based semiconductor gas sensors for CO, NO_x, CH_4, SO_2, H_2S and CO_2 gas species detecting [5.6, 5.7], but generally a single sensor is typically limited to single species detection and is undesirable in some situations such as measurements in areas of high humidity or potential explosion risk. A common gas sensing technique is spectroscopy, in which the gas absorption spectrum allows the species to be identified through the interaction between the gas and light [5.8, 5.9]. Optical fibres utilizing evanescent waves for gas sensing offer advantages over conventional sensors such as excellent remote access to hazardous areas, and safety in flammable and explosive situations. This also represents an alternative method to long multipath cells requiring expensive devices and accurate adjustments as shown in the literature [5.10, 5.11]. Germanate and tellurite glass fibres have good potential transmission properties in the mid-infrared area (3～5μm), using them as sensing elements can probe the gas species through their fundamental vibration absorption features, thus offer potential to enhance the sensing device sensitivity.

In this chapter, the design of a mid-infrared glass (germanate and tellurite glass) fibre evanescent field gas sensor is investigated and modelled. In order to investigate the overlap of the light field with gas, the power ratio of the evanescent wave to the total

propagating wave of different types of sensing fibre, D-shaped fibre, and tapered fibre, are modelled and calculated. Then the mid-infrared source with tunable wavelength from 3~3.4 μm suitable for a gas sensing device is described. The modelling of a tapered germanate fibre evanescent field gas sensing device and its performance estimation are introduced in detail, including the gas cell length, the relationship of detectable gas concentration range, minimum detectable gas concentration with gas cell length and intrinsic fibre attenuation, and the device resolution. The fabrication of tapered mid-infrared glass fibre and its transmission properties are also experimentally investigated.

5.2 Fundamental of Light Absorption Spectroscopy Gas Sensing

Many gas species exhibit characteristic absorption of light in the infrared region of the electromagnetic spectrum. This forms the basis of many optical techniques for gas detection and measurements. Absorption gas spectroscopy is realized by detecting the absorption spectrum interaction with gases to identify the gas species and gas concentration.

5.2.1 Basic theory

The absorption of light in a homogeneous gas medium is determined from the Beer-Lambert law. The intensity of transmission light through a length of absorbing medium is expressed as [5.12]:

$$I(\lambda) = I_0(\lambda)\exp(-\alpha(\lambda)cl) \tag{5.1}$$

where $I(\lambda)$ is the intensity of transmission light, $I_0(\lambda)$ is the intensity of incident light, $\alpha(\lambda)$ is the absorption coefficient of gas at wavelength λ in unit concentration and unit length, c is the gas concentration, and l is the length of the gas cell in which the light interacts with the medium. Figure 5.1(a) shows the principle schematic of light absorption spectrum gas sensing method and (b) the schematic of light absorption spectrum with the absorption gas spectrum.

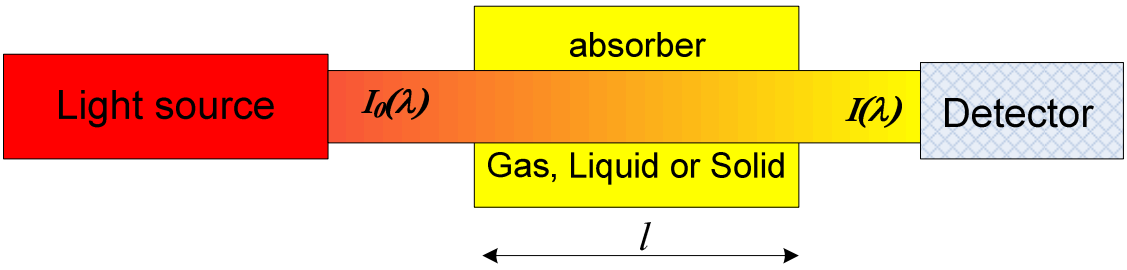

Fig.5.1 (a) Principle schematic of light absorption spectrum gas sensing method

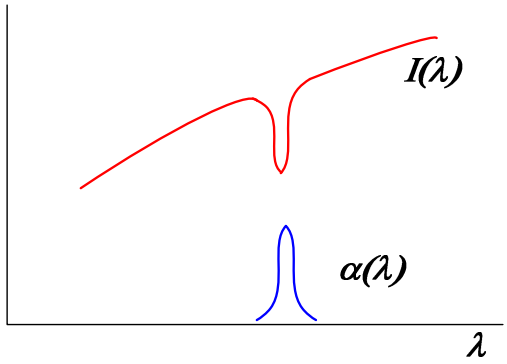

Fig.5.1 (b) Schematic of light absorption spectrum with the absorption gas spectrum

From this simple equation (5.1), it is possible to determine the transmitted intensity and hence the gas concentration at a given wavelength and gas cell length if the absorption coefficient $\alpha(\lambda)$ of the detected gas is known.

Usually it is common to use wavenumbers, ν, rather than wavelength λ in spectroscopy. The absorption coefficient of one single absorption line of gas can be expressed as [5.13, 5.14]:

$$\alpha_{\upsilon_i}(\upsilon) = S_{\upsilon_i} \frac{T_0}{T} N_L g(\upsilon - \upsilon_i) \tag{5.2}$$

where ν is the wavelength in wavenumber (cm^{-1}), ν_i is the centre of absorption line, $S_{\nu i}$ is the molecule line intensity with unit of $cm.molecule^{-1}$, T is the environmental temperature in K, T_0=273K, N_L is the total number of molecules of absorbing gas with unit of $molecule \cdot cm^{-3} \cdot atm$, and $g(\nu-\nu_i)$ is the unit normalized line shape function. The line shape function describes the effect of line broadening as a function of the pressure. At atmospheric pressure, the main factor contributing to the broadening of the absorption line is the collision between the gas molecules, and $g(\nu-\nu_i)$ is completely determined by a Lorentzian profile and is expressed by [5.13, 5.14]:

$$g(\upsilon - \upsilon_i) = \frac{1}{\pi} \frac{\gamma_L}{(\upsilon - \upsilon_i)^2 + \gamma_L^2} \tag{5.3}$$

$$\gamma_L = \gamma_{air} (296/T)^n P_t \tag{5.4}$$

where γ_{air} is the air-broadened half width (cm^{-1}/atm) at T=296K, the reference pressure P_t=1atm, and n is the coefficient of temperature dependence of the air-broadened half width.

The integral absorption coefficient of gas at wavelength λ can be written as [5.15]:

$$\alpha(\lambda) = \sum_{\lambda_i} \alpha_{\lambda_i}(\lambda) \tag{5.5}$$

where the summation is performed over all relevant lines. The absorption coefficients of different gases can be calculated by utilizing the line-by-line parameters in Hitran database [5.14]. The Hitran database is a compilation of previously measured and/or calculated spectroscopic absorption data that can be used to approximate the transmission of radiation through a gas sample.

For an optical fibre evanescent field gas sensing method, a single optical fibre is used as both sensor and a transmission line of optical signals; therefore gas detection can be done in a simple, flexible and possibly distributed way.

In an optical fibre, the light wave propagates not only in the core but also to a much lesser extent in the cladding. The latter component is called an evanescent wave, which decays rapidly with increasing distance from the fibre axis. If the fibre has no cladding or the cladding is made sufficiently thin (such as 3 core sensing fibre with the core close to the cladding-air interface), or the tapered fibre and D-shaped fibre in which the cladding material has been ground down at the pre-form stage or polished on one side to create a D-shaped profile, the evanescent wave will penetrate the region outside the fibre, as shown in figure 5.2. If there is gas outside the fibre, which absorbs the evanescent wave, the power of the propagating light is decreased.

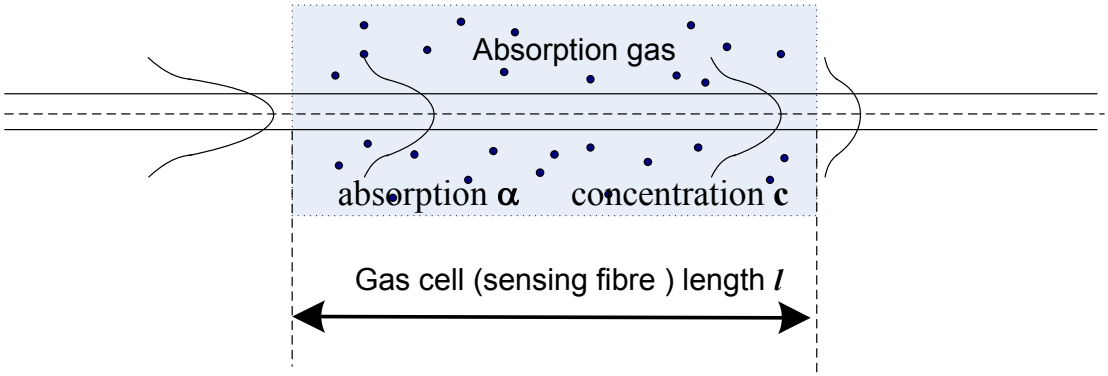

Fig.5.2 Principle of gas detection using an evanescent wave

For an optical evanescent field gas sensor, equation (5.1) can be rewritten as:

$$I(\lambda) = I_0(\lambda) \cdot \exp(-\alpha(\lambda)\eta c l) \cdot 10^{-10\alpha_1 l_1} \tag{5.6}$$

In which, α_1 is the fibre intrinsic attenuation with unit of dB/cm, comprising scattering loss, curvature loss, material absorption loss etc; l_1 is the fibre length with unit of m, the factor of 10 in the exponent arising from the units difference of fibre base attenuation and fibre length. η is the ratio of power of evanescent wave to that of the total propagating wave.

Equation (5.6) shows that the output power of light transmitted through the absorbing gas is determined by two parts: one part is the effect from the absorbing gas, which includes the gas absorption coefficient $\alpha(\lambda)$, absorption gas concentration c, and evanescent field power ratio η, fibre and gas interaction length l; the other part is the effect from the fibre intrinsic attenuation which also exponentially decreases the power output with the fibre intrinsic attenuation α_1 and fibre length l_1. The optical fibre evanescent field gas sensing device sensitivity and gas concentration measurement are determined by the output power difference with and without absorbing gas and the detector system sensitivity. Under the condition of constant source power and detector sensitivity, a smaller gas concentration can be detected and the signal is easier to be recognised if longer fibre and gas cell interaction length is used. On the other hand, the output signal will decrease exponentially with the fibre length increasing due to the intrinsic fibre attenuation, which reduces sensitivity. These two effects compete with each other to determine the evanescent field gas sensing device sensitivity and their effects will be analysed in detail in the following sections.

5.2.2 Gas absorption spectrum and selection

In this section, the absorption bands of some gases that are relevant for safety monitoring in chemical facilities, industries, mines and domestic environments are introduced in detail.

Using Hitran database 2004, the spectral location of absorption bands in the mid-infrared region for different gas species which are monitored for the safety purpose in environments are shown in figure 5.3.

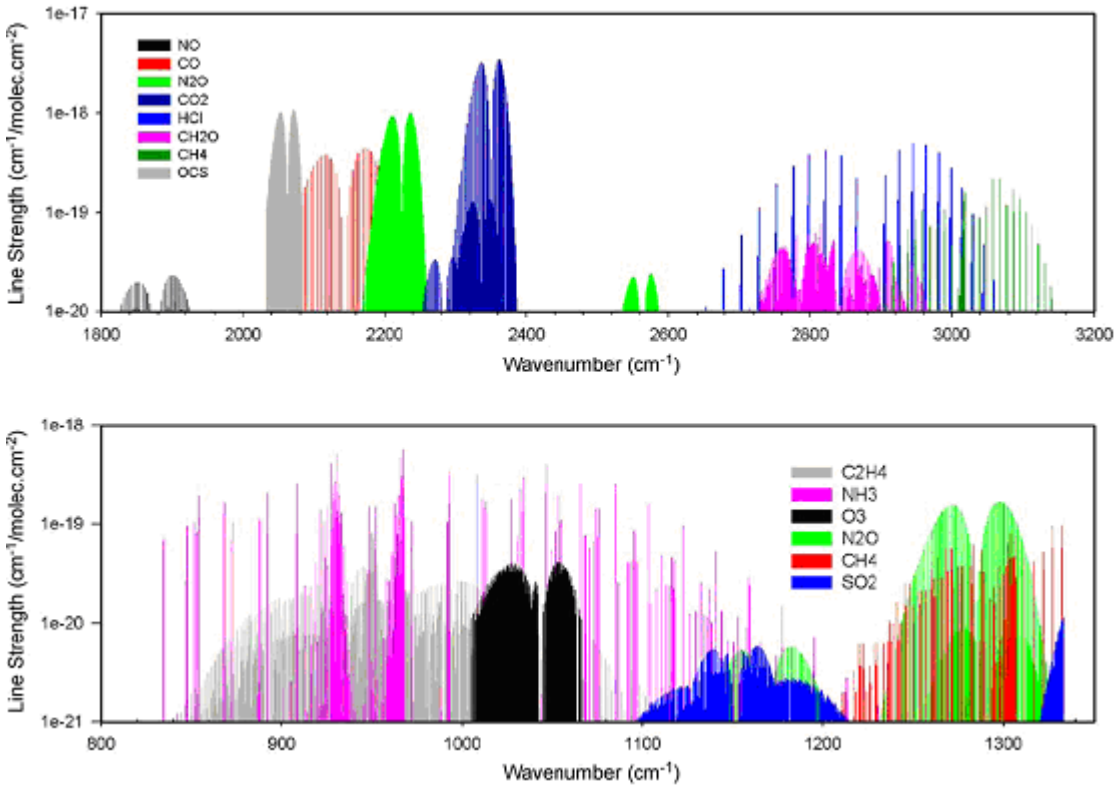

Fig.5.3 Hitran simulation of absorption spectrum in the infrared region for commonly occurring gas species which are monitored for safety purpose [5.11]

The fundamental vibrational absorption features of most gases are generally located in the mid-infrared (IR) region, which is outside the transmission window of silica fibres. Although many gases of interest, such as methane, carbon monioxide, carbon dioxide and hydrogen sulphide, also have overtone and combination absorption lines in the near-infrared region (1~2μm) which can be addressed by silica fibres and laser sources, these lines are very much weaker, typically 200 times weaker than the fundamental absorption features [5.9] and so require long interaction lengths and high sensitivity techniques to make useful gas concentration measurements. Therefore it may

be possible to enhance gas sensitivity by probing the gas species at the fundamental resonances at longer wavelengths (3~6μm). Optical fibres made of mid-infrared glass- germanate or tellurite glasses- have wide transparent optical windows from wavelengths of about 1μm to 5μm, so that a variety of pollutants and combustion gases can be monitored using their strong fundamental vibrational absorption bands. In this work, methane gas is selected as the detectable gas species because it is the main component of harsh gases, and is inflammable and explosive, with a lower explosive limit (LEL) of 5% and an upper explosion limit of 15.4% [5.16], therefore detecting methane gas concentration to below this safety limit is extremely important for the safe operation of industrial mines. The fundamental absorption bands of methane gas at about 3.1~3.5μm wavelength is shown in figure 5.4.

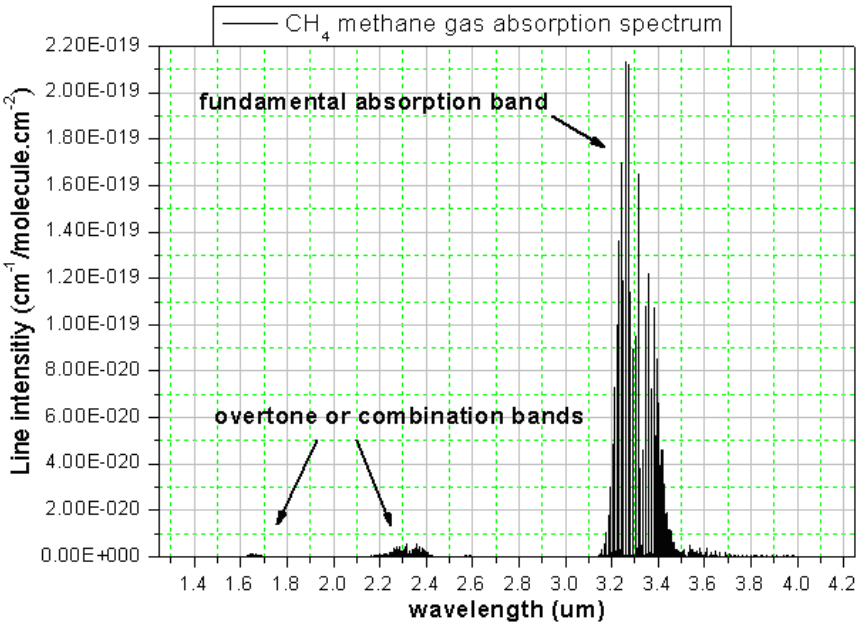

Fig.5.4 Methane fundamental absorption and overtone absorption bands [R]

A nanosecond monolithic optical parametric oscillator with the idler light output of tunable wavelength from 3.0~3.4μm was used as the light source in our modelling and was investigated in the following section 5.2.3.

5.2.3 OPO light source setup and spectrum

A light source with high output power is an important part for mid-infrared optical-fibre evanescent-field sensing. In this section, the light source investigated was a

nanosecond monolithic optical parametric oscillator (OPO) with idler light output at longer wavelength. The idler light from the OPO can be tuned from 3 μm to 3.4μm with the temperature shift range of 20^{o} C~180^{o} C, which covers the central part of the methane gas fundamental vibration absorption spectrum range (3.1~3.5μm).

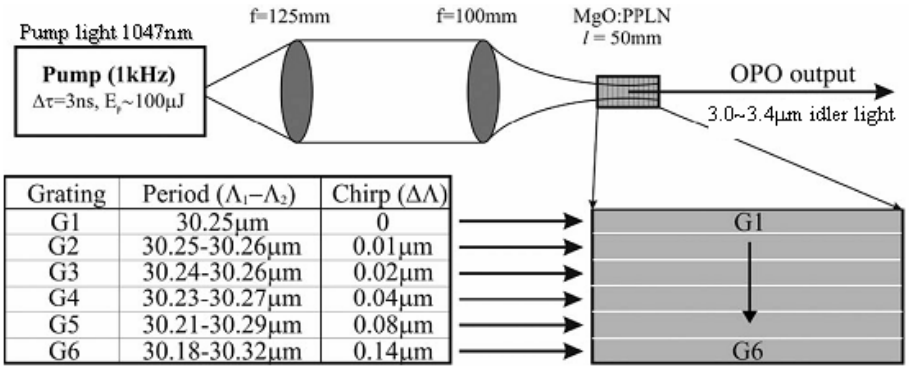

Fig.5.5 Experimental configuration of the OPO light source [5.17]

The experimental configuration of the OPO light source [5.17] is shown in figure 5.5. The output from a Q-switched Nd:YLF pump laser, which operated at 1047nm and produced 110μJ pulses at a 1kHz repetition frequency, was collimated using a 125mm focal length spherical lens. The pulses were focused into a 50mm long, 500μm thick, 5% doped magnesium-oxide-doped periodically poled lithium niobate (MgO:PPLN) crystal on the thickness direction using a 100mm focal length spherical lens to form a waist of radius 60μm (confocal parameter 47mm). The crystal had high-quality plane-parallel faces and coatings possessed an idler reflectivity exceeding 45% to allow the crystal to act as an idler-resonant cavity. Six gratings (chirped and unchirped) with each having a centre period of 30.25μm were written on it. Due to the higher output energy using the first unchirped grating compared with the other chirped gratings [5.17], the first unchirped grating with a constant grating period of 30.25μm was used in the experiment, and setup is built according to figure 5.7 to generate signal pulses with wavelength range of 1520~1610nm and idler pulses with wavelength range of 3~3.4μm when the temperature was tuned from 20°C to 180°C in the experiment. The idler output from OPO was detected using a monochromator.

Figure 5.6 (a) shows the idler light wavelength shift from 3 μm to 3.4 μm with temperature range of 20°C ~180°C, and (b) shows the idler light spectrum with 30nm bandwidth of different wavelengths at each temperature.

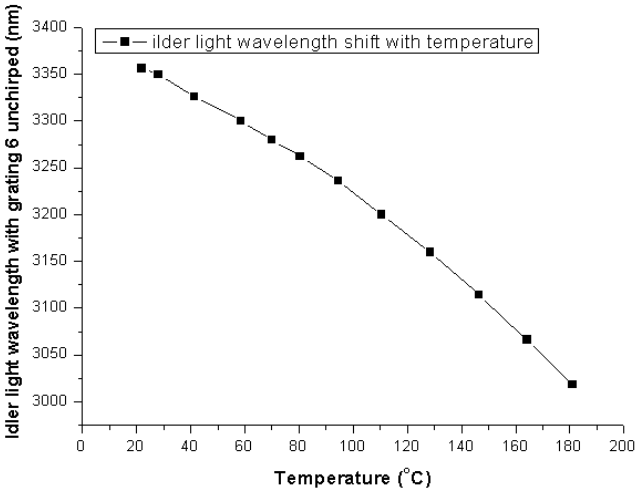

(a)

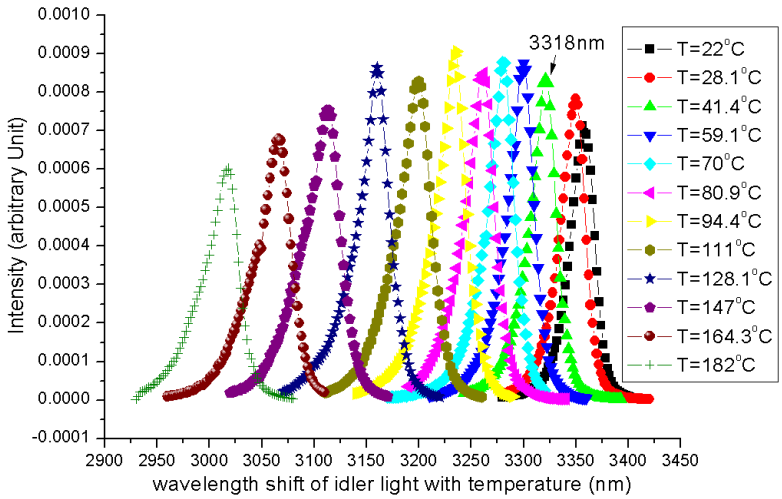

(b)

Fig.5.6 The idler light wavelength shift with temperature (a) and spectrum with 30nm bandwidth of different wavelengths (b)

The methane fundamental absorption spectrum is at 3.1~3.5μm wavelength as introduced in section 5.2.2, the spectrum overlap of the tuned idler light with methane absorption spectrum lines is shown in figure 5.7. The idler light output with central wavelength 3318nm at temperature 41.4°C was selected as the light source with pulse energy of 24μJ and repetition frequency 1KHz. The light power corresponding with the

CH_4 gas absorption spectrum in the wavelength range of 3310~3317nm is integrated to be about 50μW.

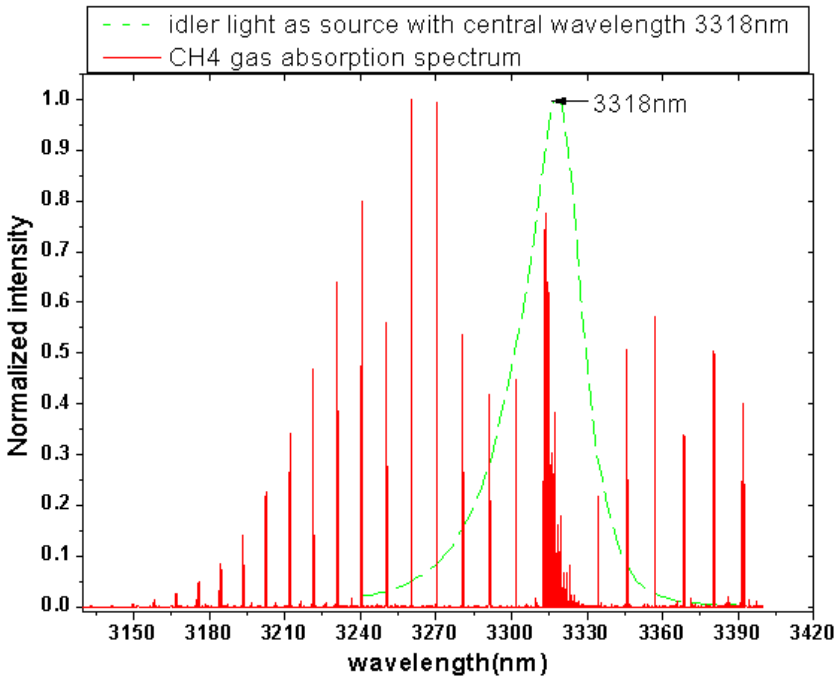

Fig.5.7 Spectral overlap between methane fundamental spectral tone (solid lines- from Hitran database [5.18]) and OPO idler output spectrum at 3318nm wavelength (dotted lines)

5.3 Evanescent Field Modelling of Different Shape Fibres for Gas Sensing

The minimum detectable gas concentration (device sensitivity) of an optical fibre evanescent field gas sensing device is determined by several parameters, including: the gas species absorption coefficient, light source power, detector system sensitivity, evanescent field ratio and interaction length of light with gas species. First two parameters have already been discussed in section 5.2.2 and 5.2.3, another important parameter is the power ratio η of the evanescent wave to the total propagating wave in the fibre.

In an optical fibre, the light wave propagates not only in the core but also in the cladding. The light in the cladding is called an evanescent wave, which decays rapidly with increasing distance from the fibre core axis. For an all fibre evanescent field gas sensing device, it clearly requires strong interaction between the gas and light guided in

the fibre evanescent field. The evanescent field intensity outside the fibre can be increased several orders of magnitude by using fibres without cladding or a cladding material is made sufficiently thin, which may be achieved by using 3 core sensing fibre with a core close to the cladding-air interface, D-shaped fibre or tapered fibre, in which the cladding material has been polished on one side to create a D-shaped profile or ground down at the pre-form stage [5.19, 5.20]. In this section, the power ratio η of the evanescent wave to the total propagating wave in the fibre with different fibre shapes- D shaped fibre, and tapered fibre- are analysed and investigated in detail.

5.3.1 D-shaped germanate and silica fibres evanescent field modelling

D fibres have a D-shaped cross-section, as shown in figure 5.8. This is produced by polishing a flat surface on an optical fibre to expose a small region close to the core [5.19] or the grinding of a parallel flat on a preform and drawing this into D-shaped fibre [5.20].

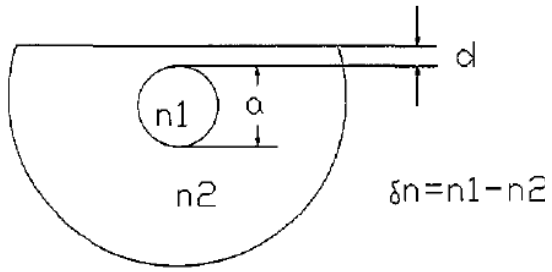

Fig. 5.8 Cross-section of D-shaped sensing fibre

An analysis approach [5.21, 5.22] employing the finite difference method in combination with perturbation techniques to model the electric field distribution in D-fibre indicated that the evanescent field intensity outside the fibre can be optimized by using the D-shaped fibre parameters as follows:

(1) as large as possible core/cladding index difference $\Delta n=n_1-n_2$;

(2) minimised core/flat distance d;

(3) optimum value for the core diameter a.

In this work, D-shaped germanate and silica fibres' evanescent field power ratios were modelled using an electromagnetics modelling software – COMSOL FEMLAB Multiphysics software. Here a single step-index waveguide made of germanate and silica glass is simulated for free-space wavelengths of 1.55μm, and the mode analysis is made on a cross-section in x-y plane of the fibre. During the simulation, the fibre parameters, such as the core/cladding and surrounding material refractive indices, the effective mode refractive index of interested, the core and cladding diameter, and the core/flat distance *d* are required. The simulation is done in 2D plane by solving the Maxwell equation to find the fundamental mode, and the data obtained from the software were analysised using mathematic language Matlab to get the power ratio in the evanescent field on the flat side of the D-shaped fibre.

The singlemode germanate fibre with core diameter 6μm, cladding diameter 130μm as shown in figure 5.9 was used in the modelling. The refractive index of the germanate fibre core and cladding are 1.83 and 1.815 respectively with the core/cladding index difference 0.015.

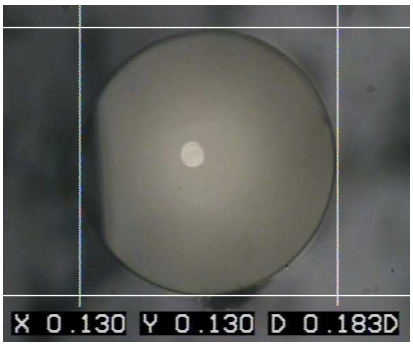

Fig.5.9 Germanate singlemode fibre with core diameter 6μm, cladding diameter 130μm and core/cladding index difference 0.015

In order to get the maximum evanescent field power outside the fibre, the core/flat distance *d* is selected as *0* in the modelling. The effective refractive index of the mode analysed in the software was selected with value of $n_{eff}=1.826586+5.858605\times10^{-18}$. The ratio η of evanescent wave power on the flat side of the D-shaped fibre to total propagating wave power is calculated about 0.003% for the germanate fibre. The optical field distribution in the D-shaped germanate is shown in figure 5.10 (a).

In order to verify the modelling validity, the same modelling method was also used for the D-shaped silica fibre with core diameter a=6μm, refractive index difference Δn=0.03 and the core/flat distance d=0. The optical field distribution in the D-shaped silica fibre is shown in figure 10(b). The power ratio of the evanescent wave on the flat side of the D-shaped fibre to total propagating wave is about 0.11%, which is consistent with the value calculated from the literature [5.23].

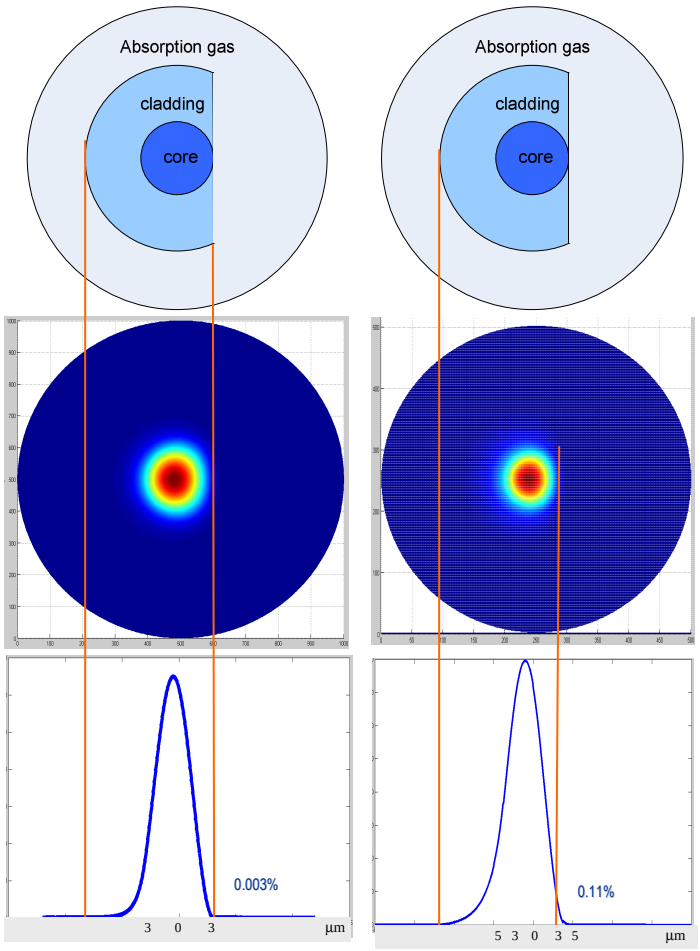

(a) (b)

Fig.5.10 Optical field distribution in the D-shaped germanate fibre (a) and silica fibre (b)

Figure 5.10 shows that most of the light is confined in the fibre core and cladding. At the D-shaped cladding-absorbing gas interface, the optical power penetrating outside the cladding into the evanescent field in the gas area drops rapidly

due to the high index difference between the cladding and surrounding medium, which results in a lower evanescent power ratio for the higher refractive index germanate fibre.

The analyses and modelling in this section show that the evanescent wave power ratio of 0.003% outside a D-shaped germanate fibre is still weak for an evanescent field gas sensing device, moreover, the potential Mid-infrared transmission advantages of germanate glass fibre for the application of gas sensing devices through detecting the gas species strong vibration absorption bands compared with detecting the overtone and combination absorption lines using D-shaped silica fibre with evanescent power ratio of 0.11% is nearly completely lost. An alternative is to use single mode tapered fibre as the sensing element and the evanescent field power ratio outside a tapered fibre will be discussed in the following section 5.3.2.

5.3.2 Tapered germanate fibre evanescent field modelling

Tapered optical fibres have been widely used for optical applications such as couplers, optical multiplexers, optical filters and sensors. A tapered fibre evanescent field gas sensing device relies on the interaction of the external gas species with the evanescent field surrounding the fibre waist, which spreads out into the cladding and reaches the external environment when the core and cladding diameters are gradually reduced. The taper parameters, such as waist diameter, length and shape are important in defining sensing properties. In this section, the influence of taper waist diameter on the power in the evanescent field is discussed, and the power ratios of the tapers with different diameter *d* are modelled and calculated.

Figure 5.11 shows the general structure of tapered optical fibre, which consists of a contracting tapered region, a central uniform waist region and an expanding tapered region respectively.

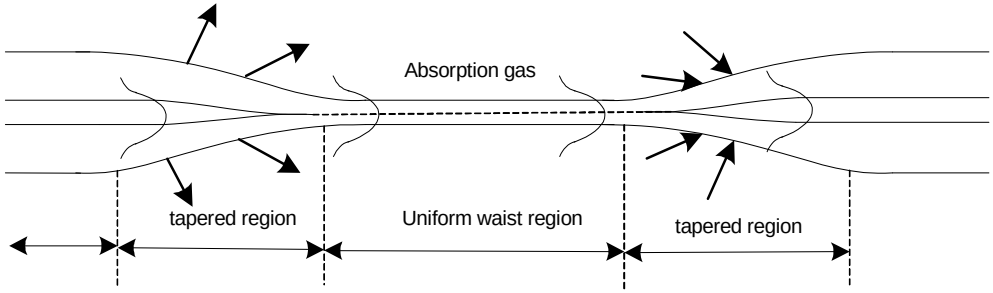

Fig.5.11 General structure and operational mechanics of tapered optical fibre

When the diameter of the uniform waist region is smaller and comparable with the wavelength of the guided light, the index difference between the fibre core and the surrounding medium is large, and the small index difference in a standard fibre between the high-index of the core and the low-index of the cladding inherited from the starting fibre can be ignored. Then the refractive index profile of the uniform waist region can be assumed to be a step-index profile of air-cladding as shown in figure 5.12. Where *a* is the diameter of uniform waist, $n_1$and n_2 are refractive indices of the fibre material and the surrounding medium respectively.

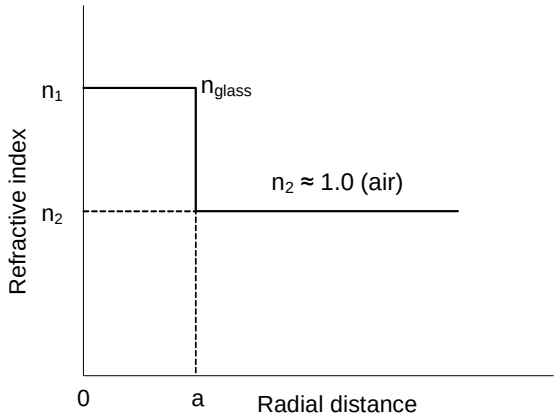

Fig.5.12 Refractive index profile of tapered fibre uniform waist region with air-cladding

For an optical fibre, the normalized frequency V is a dimensionless parameter, which gives information about the number of modes propagating in the fibre and how well the power is confined in the core [5.24]. The parameter V is defined as:

$$V = \frac{2\pi}{\lambda} \rho_{core}(z) \cdot (n_{core}^2 - n_{cladding}^2)^{1/2} \tag{5.7}$$

where λ is the wavelength, ρ_{core} is the core radius; n_{core} and $n_{cladding}$ are the refractive index of the core and cladding respectively.

The mode-field diameter $2w_0$ is an important parameter for the single mode optical fibre which determines the diameter of light field within which $1\text{-}e^{-2}$(86.5%) of the total power is confined. The relationship of the light field radius w_0 with the core diameter $\rho_{core}(z)$ depends on the fibre *V* value and can be seen through the following empirical formula [5.24]:

$$\frac{w_0}{\rho_{core}(z)} = 0.65 + 1.619V^{3/2}(z) + 2.879V^{-6}(z) \tag{5.8}$$

When the fibre is tapered, the mode field distribution in the core varies with the fibre core diameter in line with equation (5.7), (5.8).

At the beginning of the taper region, the light propagates as a core mode and most of energy is confined within the core.

As the fibre is tapered down, stretching the fibre decreases the value of *V*, consequently the intensity distribution of the core mode changes from a narrow profile to a broader one, the light begins to spread out into the cladding and propagates as a cladding mode that is guided by the boundary between the cladding and the air. The position where the propagation mode transfers from the core mode to the cladding mode is referred to as the "core-mode cutoff", and occurs at the point where the V number of the tapered fibre is given by [5.25]:

$$V_{cc} = \sqrt{\frac{2}{\ln s}}\left(1 + \frac{0.26}{\ln s}\right)^{\frac{-1}{2}} \tag{5.9}$$

where *s* is the ratio between the radius of the cladding and the core. The cutoff value V_{cc} is minimum value of V for which light is guided through the core. When the fibre is tapered down, the V value decreases until to a point is reached where $V_{core}(z)$ equals to V_{cc}, then from this point the cladding and the surrounding medium act as the waveguide structure and the light propagates as a cladding mode.

At the uniform region of the tapered fibre, the cladding and the surrounding medium act as the wave guiding structure, and the power distribution in the cladding and the evanescent field can be exactly analyzed and numerical calculated using Maxwell's equation using boundary conditions [5.26], or modelled using a novel finite difference beam propagation method [5.27, 5.28].

In this work, the power distribution ratio of the evanescent wave to total propagating wave of the tapered germanate fibre guided along an infinitely long fibre with different uniform waist diameter were modelled using the COMSOL FEMLAB Multiphysics software in 2 dimensions, in which the parameters of propagating light wavelength, fibre material refractive index and taper diameter are considered. In this modelling, due to the diameter of the uniform waist region is smaller and comparable with the wavelength of the guided light, the index difference between the fibre core and the surrounding medium is large, and the small index difference in a standard fibre between the high-index of the core and the low-index of the cladding inherited from the

starting fibre can be ignored, here only the fibre core refractive index and the interface between the core and surrounding medium is considered.

Figure 5.13 shows the germanate fibre mode field distributions inside the fibre and the evanescent field for different taper waist diameters at wavelength of 3.3μm. As we can see, the 3μm diameter fibre (a) confines most of the light inside the fibre, while as the fibre diameter drops, more light penetrates outside the fibre and is guided in the form of an evanescent wave, as shown in figure 5.13 (b,c,d).

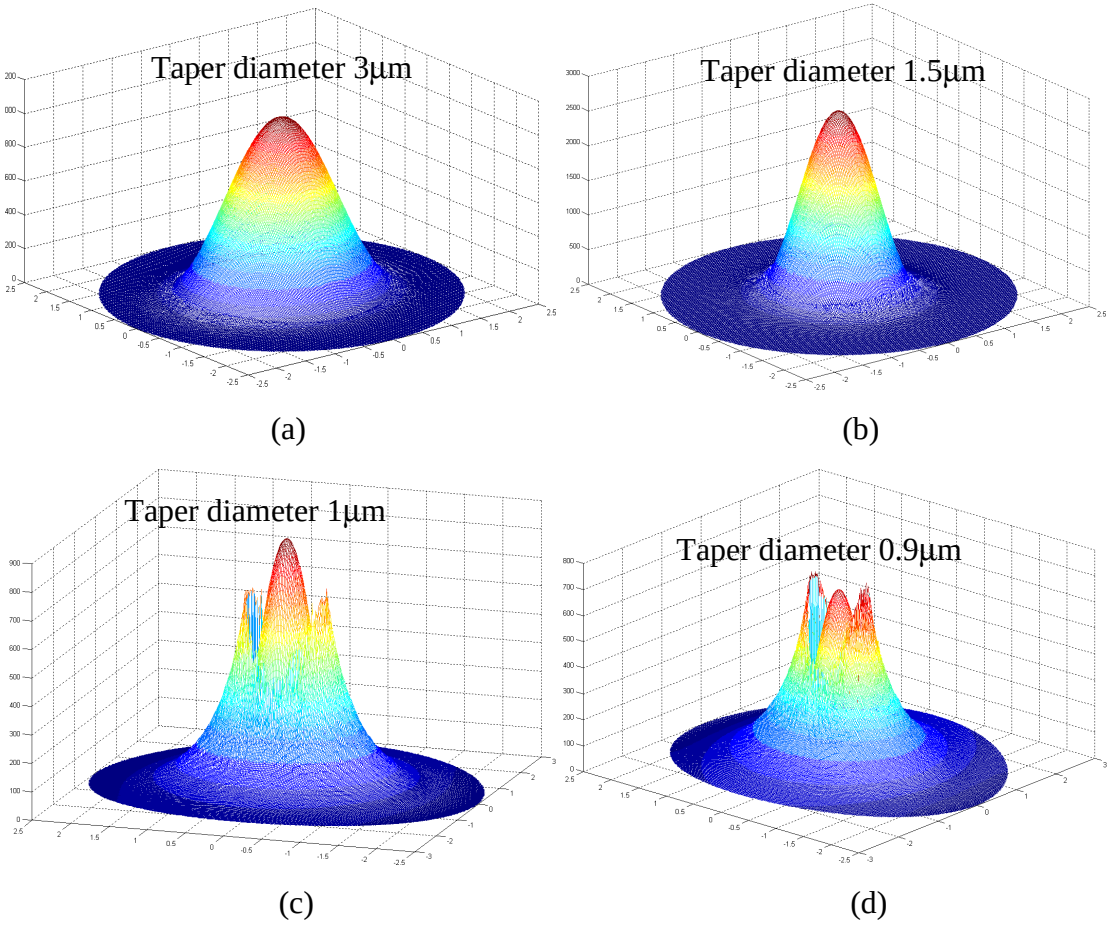

Fig. 5.13 Mode field distribution of 3300nm wavelength light guided by germanate tapered fibre with a diameter of 3μm (a), 1.5μm (b), 1μm (c) and 0.9μm (d)

Figure 5.14 shows the power ratio η of evanescent wave to total propagating wave with the tapered fibre diameter d. It can be seen that the evanescent wave power ratio increases rapidly when the fibre diameter decreases to wavelength range. When the fibre diameter drops below 1μm, more than 40% of the energy is guided in the

evanescent wave outside the germanate fibre core. Compared with only ~0.003% for the D-shaped fibre, such an increase is significant for improving the sensitivity of optical fibre evanescent field sensors. However, maintaining a steady guiding field in such situation (the fibre core diameter is smaller than the wavelength of guiding light) may be difficult because any small deviation such as surface contamination or microbends from the ideal condition leads to a change in propagating fields and radiation loss, and more analysis and work will be required in future.

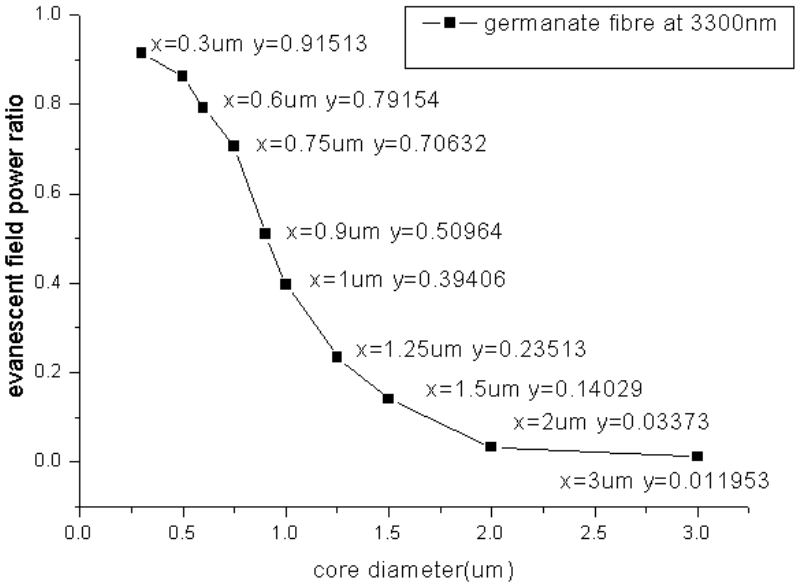

Fig.5.14 Germanate fibre power ratio η of evanescent wave to that of total propagating wave with the tapered fibre diameter at 3300nm wavelength

5.4 Transmission Spectrum Measurement of Bulk Germanate Glass

As discussed in section 5.2.1, the intrinsic fibre attenuation has an important impact on the sensitivity of optical fibre evanescent field gas sensing devices. In section 5.2.2, we observed that the strong fundamental absorption vibrations of most gases lie in the mid-infrared region, which is outside the transmission window of silica fibre (<2μm), thus tellurite or germanate glass fibre shows great potential as sensing element in the optical fibre evanescent field gas sensing devices because the different electronic structures in these glasses promise much lower attenuation in the near and mid-infrared

regions. Here the transmission spectrum of bulk samples of germanate glass are measured using FTIR and OPO idler light source.

Figure 5.15 shows the absorption spectrum of germanate glass bulk sample which was measured by Leeds University. It can be seen that there is strong absorption at wavelength range of 2.8~3.2μm believed to be due to water absorption in the germanate glass bulk sample. Our transmission spectrum measurement using the FTIR and OPO idler light source, as in figure 5.16, also shows lower transmission at the wavelength range of 2.7~3.2μm due to water absorption, which is in good agreement with the absorption spectrum in figure 5.15. The measurement results using FTIR and OPO idler light source show good consistency with each other and the attenuation of the bulk germanate is calculated to be about 12dB/cm at 3.3μm wavelength due to water absorption, and the germanate fibre attenuation at 3.3μm wavelength is nearly equally to the silica fibre. The fibre transmission spectrum in the mid-infrared wavelength 3.1～3.5 μm could not be observed in our experimental measurement due to the water absorption. Now an improved technique, multistage dehydration process, has been used to decrease the OH^- content in the fabricated tellurite glasses with composition of $80TeO_2$-$10ZnO$-$10Na_2O$ and transmittance is about 75% at 3.3μm [5.31].

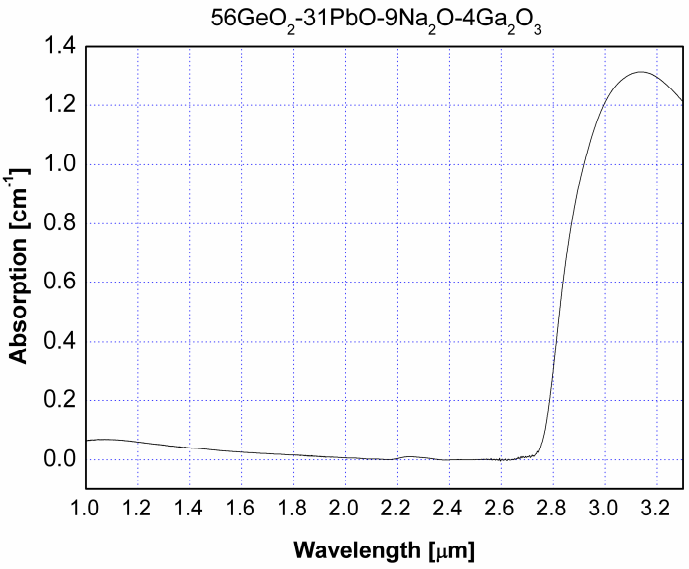

Fig.5.15 Absorption spectrum of germanate glass bulk [measured by X. Jiang at Leeds University]

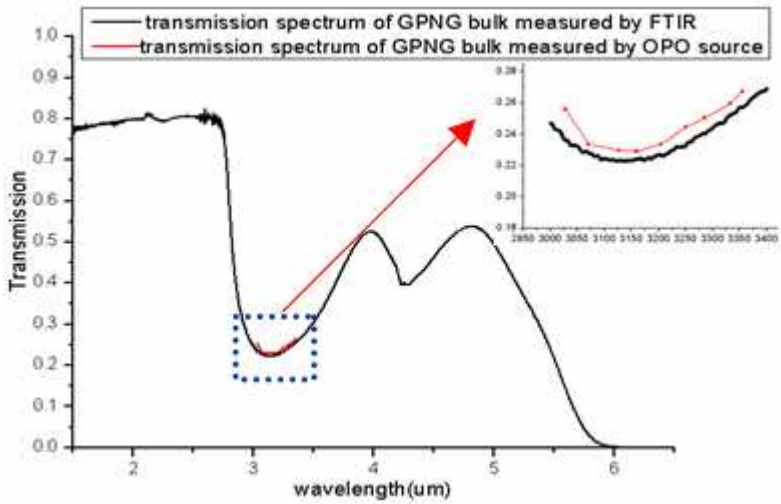

Fig.5.16 Transmission spectrum of germanate glass bulk measured by FTIR and OPO idler light source

The poor transmission properties in the mid-infrared wavelength 3.1～3.5 μm of the supplied germanate glass fibre prevented any further experimental work on the gas species sensing measurement. In the following sections, the influences of the sensing fibre length and fibre attenuation on the evanescent field gas sensor performance using tapered germanate glass fibre as sensing element will be modelled and analysed.

5.5 Tapered Fibre Evanescent Field Gas Sensing Device Modelling and Performance Estimation

The optical fibre evanescent field gas sensing device is based upon the attenuated total internal reflection spectroscopy, which utilizes the absorption of evanescent field penetrating out from the fibre region where is surrounded by the absorbing gas being detected. This method uses a single optical fibre as both a sensor and a transmission line for optical signals; therefore gas detection can be done in a simple, flexible and possibly distributed way. The sensor sensitivity (minimum detectable gas concentration) depends on the fractional power carried by the evanescent wave in the sensing region, the interaction length of the gas with the evanescent field (sensing fibre length) and the optical fibre attenuation. In this section, the influences of the sensing fibre length and optical fibre attenuation on the sensor minimum detectable gas concentration and resolution are analysed, and possible sensor performance is

estimated. Schematic of the model is shown in figure 5.17, where the SiO_2 fibre spliced on two sides of germanate fibre are not considered in the modelling.

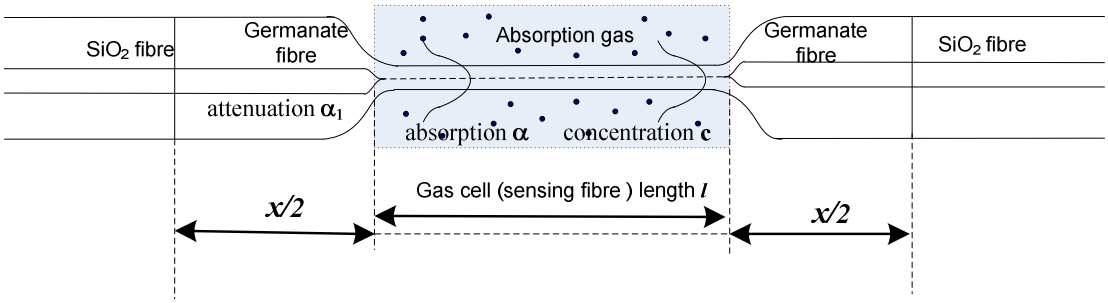

Fig. 5.17 Schematic of the model

5.5.1 Gas cell length limit and detectable gas concentration range

The absorption gas information is carried in and detected by the optical transmission power, as equation 5.6, and the minimum gas concentration that can be detected depends on the signal to noise ratio of the detection system. If the signal to noise ratio P_{signal}/P_{noise}= S/N<1, the signal is obscured by noise, while S/N>1, the signal can be recognised. Using the noise equivalent power of the detector system (*NEP*) and the bandwidth of the detector system $\sqrt{B}$, we get:

$$I_1(\lambda) = I_0(\lambda) \cdot \exp(-\alpha(\lambda)\eta cl) \cdot 10^{-10\alpha_1 l_1} \geq NEP\sqrt{B} \tag{5.10}$$

$$I_2(\lambda) = I_0(\lambda) \cdot 10^{-10\alpha_1 l_1} \cdot \left[1 - \exp(-\alpha(\lambda)\eta cl)\right] \geq NEP\sqrt{B} \tag{5.11}$$

Equation (5.10) shows the absolute signal after the gas cell compared with the detector system sensitivity, equation (5.11) gives the signal difference with and without gas absorption compared with the detector system noise equivalent power, which determines the minimum detectable gas concentration of the sensing device.

In equation (5.10), (5.11), α_1 is the fibre base attenuation with unit of dB/cm, comprising scattering loss, curvature loss, material absorption loss etc; l_1 is the fibre length with unit of *m*, the factor of 10 in the exponent arising from the unit difference of fibre base attenuation and fibre length, l is the interaction length of the gas with the optical evanescent field. Usually the fibre length l_1 is longer than the gas cell length l (light gas interaction length) for the purpose of easy handling in practise. η is the ratio of power of evanescent wave to that of the total propagating wave.

According to equation (5.10), (5.11), the gas cell length limit and detectable gas concentration range are obtained as follows, in which the effects from the fibre attenuation, gas cell length and the detector system sensitivity are considered.

Gas cell length limit with unit of (m):

$$l \le \frac{1}{10\alpha_1}\log(\frac{I_0}{2NEP\sqrt{B}}) - x \tag{5.12}$$

Gas concentration range that can be detected:

$$\frac{1}{\alpha\eta l}\ln(\frac{I_0 10^{-10\alpha_1(l+x)}}{(I_0 10^{-10\alpha_1 l}) - NEP\sqrt{B}}) \le c \le \frac{1}{\alpha\eta l}\ln(\frac{I_0 10^{-10\alpha_1(l+x)}}{NEP\sqrt{B}}) \tag{5.13}$$

Here the fibre length difference of sensing part (gas and evanescent field interaction length) with total fibre length is assumed to be *x* m.

Equation (5.13) shows the detectable gas concentration range of different gas cell length. The left side displays the minimum detectable gas concentration limit which is determined by the signal difference with and without gas compared with the detector sensitivity; it should decrease with increasing fibre gas interaction length if the fibre intrinsic attenuation is not taken into account. That means a smaller gas concentration can be detected using longer fibre gas interaction length. On the other hand, longer fibre will cause the output signal decreasing exponentially with the length due to fibre intrinsic attenuation. These two factors compete with each other to determine the detectable gas concentration range of different gas fibre interaction length *l* as shown in equation (5.13).

5.5.2 Optical fibre evanescent field gas sensor resolution

Another important factor to determine is the minimum resolvable gas concentration.

The sensitivity of the sensor to changes with the gas concentration can be calculated by differentiating equation (5.6) to gas concentration *c*:

$$S = \frac{dI(\lambda)}{dc_{gas}} = -\alpha(\lambda)\eta l I_0 \cdot 10^{-10\alpha_1(l+x)} \cdot \exp(-\alpha(\lambda)\eta c l) = -\alpha(\lambda)\eta l I(\lambda) \tag{5.14}$$

It shows that the sensitivity decreases exponentially with the fibre intrinsic attenuation coefficient α_1. $\alpha(\lambda)$ is the gas absorption coefficient. Therefore the fibre intrinsic attenuation displays an important role in the gas sensing device and its influence on the sensitivity will be analysed in the section 5.5.3.

The sensitivity S in equation (5.14) has an optimum at cell length l which can be found from the derivative of S with respect to l, as shown in equation (5.15-5.17):

$$\frac{dS}{dl} = -\alpha(\lambda)\eta I_0 \cdot 10^{-10\alpha_1 x} \cdot 10^{-10\alpha_1 l} \cdot \exp(-\alpha(\lambda)\eta c l) \cdot \left[1 - \alpha(\lambda)\eta c l - 10\alpha_1 l \ln 10\right] \tag{5.15}$$

From equation (5.15), it can be seen that:

when $$l_{opt} = 1 \Big/ (\alpha(\lambda)\eta c + 10\alpha_1 \ln 10) \tag{5.16}$$

the S has optimum with $$\left|S_{opt}\right| = \frac{10^{-10\alpha_1 x}}{e} I_0 \alpha(\lambda)\eta l_{opt} \tag{5.17}$$

Therefore, for a given gas of concentration c, gas absorption $\alpha(\lambda)$, fibre intrinsic attenuation α_1, and evanescent power factor η, the sensor has its optimum sensitivity S_{opt} for an optimum fibre gas interaction length $l_{opt.}$

The resolution Δc of a sensing device using monochromatic light can be calculated from the sensitivity given by equation (5.14) if the following additional data of the gas sensing device are known:

(1) Monochromatic IR source intensity I_o;

(2) Detector system information: noise equivalent power of the detector system *NEP*, and bandwidth of the detector system *B.*

Then the resolution is given by:

$$\Delta c = \frac{NEP\sqrt{B}}{\left|S\right|} = \frac{NEP\sqrt{B}}{I_0 \alpha\eta l \cdot 10^{-10\alpha_1 (l+x)} \cdot \exp(-\alpha\eta c l)} \tag{5.18}$$

Using $l_{opt} = 1 \Big/ (\alpha\eta c + 10\alpha_1 \ln 10)$, we obtain the optimum Δc with different gas concentration:

$$\Delta c = \frac{NEP\sqrt{B}}{I_0 \alpha\eta l_{opt} \cdot \frac{10^{-10\alpha_1 x}}{e}} = \frac{NEP\sqrt{B}}{I_0} \cdot e \cdot 10^{10\alpha_1 x} \cdot \left(c + \frac{10\alpha_1 \ln 10}{\alpha\eta}\right) \tag{5.19}$$

Equation (5.19) gives the maximum resolution of the gas sensor with the gas concentration at the optimum fibre gas interaction length l_{opt}.

5.5.3 Performance estimation of the optical fibre evanescent field gas sensing device

According to equation (5.13), the detectable gas concentration of the tapered fibre evanescent field gas sensing device is determined by:

(1) the gas absorption coefficient α;

(2) light source intensity corresponding to the gas absorption spectrum I_0;

(3) the ratio of power of evanescent wave to that of the total propagating wave η;

(4) the detector system noise equivalent power *NEP* and bandwidth *B*;

(5) interaction length of the evanescent field with the absorption gas *l* and the fibre base attenuation α_l.

For our estimation, methane gas is selected as the detectable gas species because it is the main component of toxic gases, and is inflammable and explosive[5.16], therefore detecting methane gas concentration to below this safety limit 5% is extremely important for the safe operation of industrial mines.

The methane gas fundamental absorption vibration at 3.32μm was selected, which is nearly 200 times stronger than the overtone and combination absorption lines as introduced in section 5.2.2, and hence offers potential for enhanced sensitivity. The absorption coefficient of methane gas at 3.392μm with the value of α=8.3 atm^{-1} cm^{-1} in literature [5.29] was used in this work for the performance estimation, because 3.32μm and 3.392μm absorption lines belong to the same fundamental absorption vibration band and the absorption coefficient are roughly consistent with each other.

The idler light output from an optical parametric oscillator [5.17] at central wavelength 3318nm was used as the light source with pulse energy of 24μJ and repetition frequency 1 KHz, as in section 5.2.3. The light power corresponding with the CH_4 gas absorption spectrum in the wavelength range of 3310~3317nm is integrated to be about 50μW.

In section 5.3.2, the power ratio η of evanescent wave to total propagating wave of the tapered fibre with different diameter *d* was modelled and calculated, as shown in figure 5.14. If the optical fibre is tapered with the uniform waist diameter of 1μm, the power ratio in the evanescent wave to the total propagating wave is about 39%.

A PbSe infrared detector was used in our modelling with noise equivalent power *(NEP)* 1.5×10^{-10} $W/(Hz)^{1/2}$ and minimum bandwidth 0.2Hz [5.30].

Modelling results

Using equation (5.13) and the sensing device parameters as follows: methane gas absorption coefficient α=8.3atm^{-1} cm^{-1}, light source I_0=50μW, evanescent field

ratio η=39% of the tapered fibre with 1μm uniform waist diameter, and the detector noise equivalent power $NEP\times(B)^{1/2}$ =6.7×10^{-8} mW, the detectable gas concentration range of different gas cell length l in our modelling is determined by:

$$\frac{-1}{\alpha\eta l}\ln(1-10^{-6+10\alpha_1(l+x)}) \le c \le \frac{1}{\alpha\eta l}\ln(10^{6-10\alpha_1(l+x)}) \qquad (5.20)$$

In the following, we will analyse the detectable gas concentration range and the sensitivity of the sensing device with different gas cell length l in two aspects:

Ⅰ. Variable fibre attenuation α with fixed fibre gas cell length difference x ;

Ⅱ. Variable fibre gas cell length difference x with fixed fibre attenuation α.

Ⅰ. Modelling results of the detectable gas concentration range and the minimum detectable gas concentration for different gas cell length *l*, with variable fibre base attenuation α and fixed fibre gas cell length difference *x=60cm*

The modelling result with fibre intrinsic attenuation of 0.1dB/cm and fibre gas cell length difference of 60cm is shown in figure 5.18.

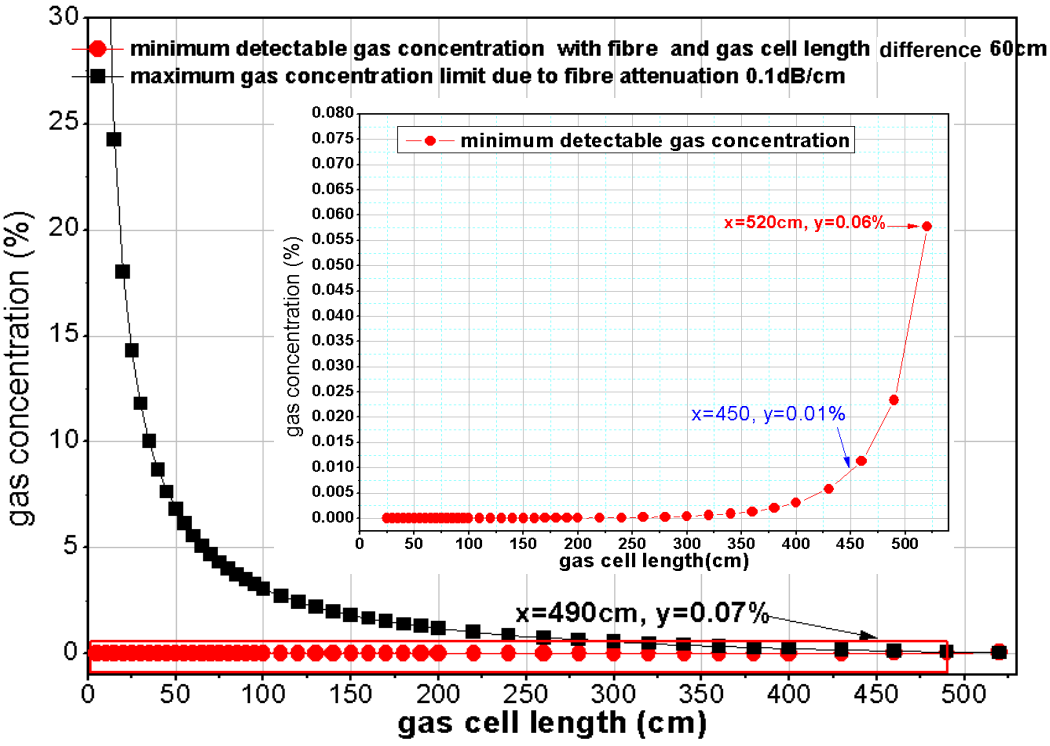

Fig 5.18 the minimum detectable gas concentration and the detectable gas concentration range for different gas cell length, fibre attenuation 0.1dB/cm

The black square dotted line corresponds with the maximum detectable gas concentration for different gas cell lengths, which is determined by the fibre intrinsic attenuation and the detector system sensitivity.

The red circle dotted line shows the minimum detectable gas concentration for different gas cell lengths, which is determined by the signal difference with and without gas compared with the detector sensitivity. It should decrease with fibre gas interaction length increasing if the fibre intrinsic attenuation is not taken into account or is minor compared with the gas absorption. While from the inserted enlarged figure, we can see that the minimum detectable gas concentration increases with the gas cell length due to fibre intrinsic attenuation which plays a major role compared with the effect from the gas absorption for longer fibre gas interaction lengths.

The values between the black square dotted line and the red circle dotted line display the detectable gas concentration regions for different gas cell lengths, for example, with the gas cell length of 200cm, the detectable gas concentration range is from 1.2% to 0.6ppm theoretically in our modelling. Figure 5.18 shows that the gas concentration detection requirement lowers than 5% in industrial applications can be achieved using the gas cell length (fibre length) shorter than 75cm with the fibre attenuation of 0.1dB/cm.

Figure 5.19 shows the detectable gas concentration range and minimum detectable gas concentration for different gas cell length when the fibre base attenuation is 0.5dB/cm.

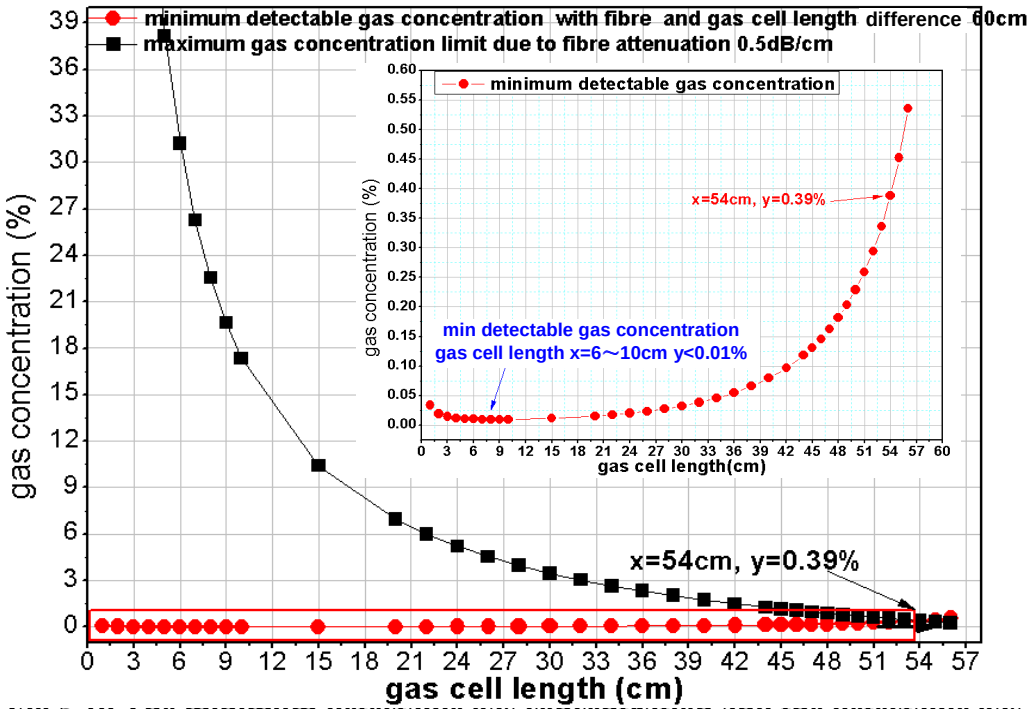

Fig 5.19.The minimum detectable gas concentration and the detectable gas concentration range for different gas cell length, fibre attenuation 0.5dB/cm

The inserted enlarged figure—minimum detectable gas concentration with gas cell length—shows that: at the short cell length range, the minimum detectable gas concentration decreases with the cell length increasing; with increasing cell length, the minimum detectable gas concentration reaches the lowest value, and then increases. The reason for that is the competition of the effect from fibre attenuation with the effect from gas absorption under the given detector system sensitivity limit and light source power. When the gas cell length is very short, higher gas concentration is required to meet the detector sensitivity requirement, which plays a major role compared with the effect of fibre attenuation. At this stage, the minimum detectable gas concentration decreases with the gas cell length increasing. On the other hand, the effect of fibre attenuation increases with the cell length increasing until it is nearly equal to the effect from the gas absorption; at this point the minimum detectable gas concentration has the lowest value. After that, the fibre attenuation shows a major effect and the minimum detectable gas concentration increases with increasing gas cell length. Overall, there is a balance for the effect from gas absorption and fibre attenuation which determines the gas cell length range with lower minimum detectable gas concentration.

The maximum gas cell length with the fibre base attenuation of 0.5dB/cm is about 54cm. The gas cell length range for the minimum detectable gas concentration

lower than 0.01% is about 6~10cm. and the cell length limit for the detectable gas concentration lower than 5% is about 25cm.

Figure 5.20 displays the detectable gas concentration range and minimum detectable gas concentration for different gas cell length when the fibre base attenuation is 0.9dB/cm.

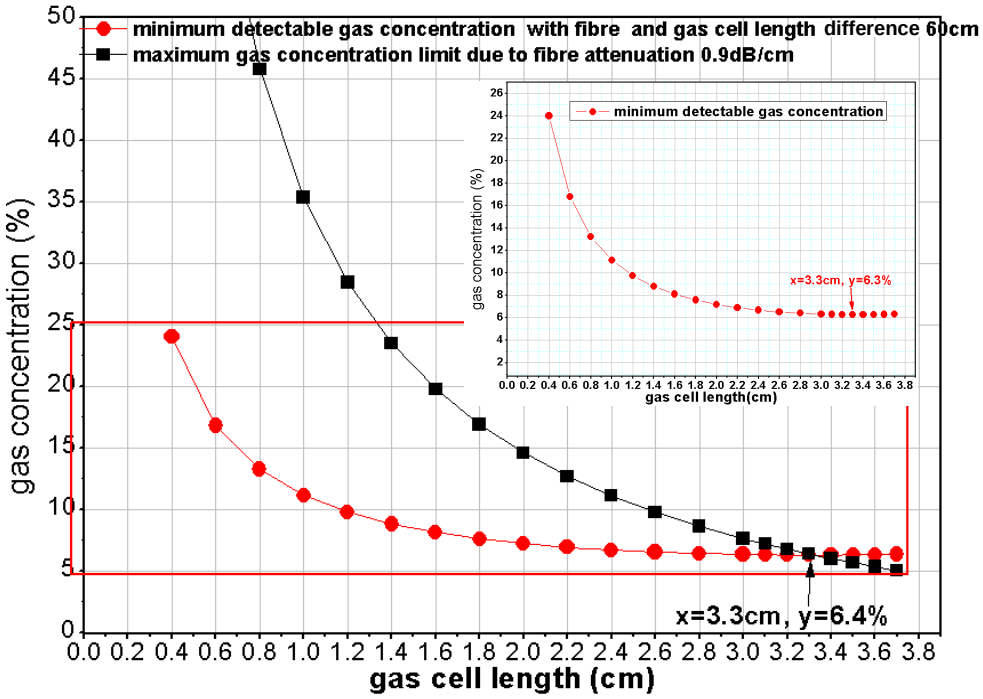

Fig 5.20.The minimum detectable gas concentration and the detectable gas concentration range with different gas cell length, fibre attenuation 0.9dB/cm

The inserted enlarged figure shows that the minimum detectable gas concentration decreases continually with gas cell length increasing up to the maximum gas cell length, that means the gas absorption effect is major and plays an important role on the sensitivity with different fibre length (cell length) compared with the influence from fibre attenuation using a short gas cell length. Figure 5.20 shows that the maximum gas cell length with the fibre intrinsic attenuation of 0.9dB/cm is nearly 3cm, and the minimum detectable gas concentration is 6.3% with gas cell length of 3cm, which is higher than the lower explosive limit (LEL) of methane gas in air 5%.

Above analyses show that with the fixed fibre gas cell length difference, the minimum detectable gas concentration increases with the fibre base attenuation increasing, and the maximum gas cell length that can be used decreases correspondingly.

Figure 5.21 displays comparisons of the minimum detectable gas concentration shift with gas cell length of different fibre base attenuations from 0.1db/cm to 0.9dB/cm, the fibre gas cell length difference is fixed with 60cm.

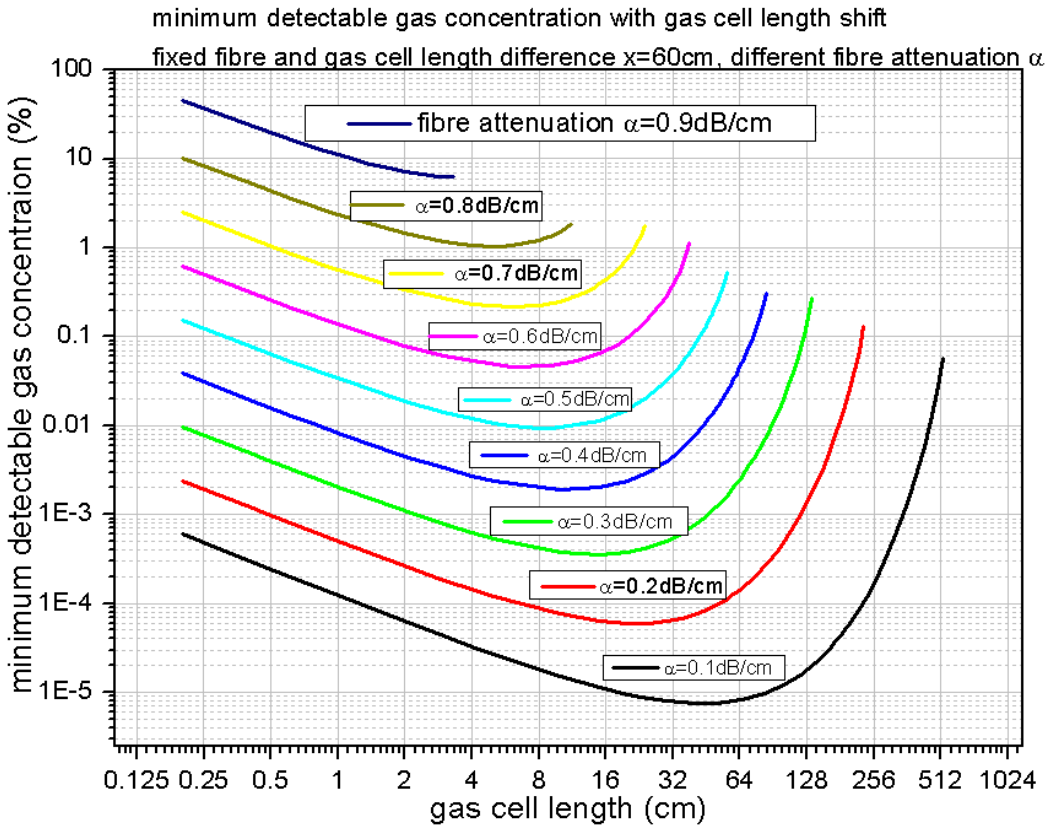

Fig 5.21 Comparisons of minimum detectable gas concentration shift with gas cell length of different fibre attenuation from 0.1dB/cm to 0.9dB/cm

From figure 5.21, we can get the relationship of maximum gas cell length limit and the minimum detectable gas concentration with the gas cell length for different fibre attenuations. For example, with the fibre attenuation of 0.4dB/cm, the maximum gas cell length can be used in the sensing device is about 80cm, and lower than 0.01% gas concentration can be detected with the cell length range of 1～44cm. While for the fibre with attenuation of 0.9dB/cm, the minimum detectable gas concentration is about 6.3% with the cell length of 3cm, which is higher than the lower explosive limit (LEL) of methane gas in air 5%, therefore the length difference between the fibre and gas cell in this sensing device has to be reduced to increase the detectable gas concentration sensitivity. The influence of the length difference between the fibre and gas cell on the

minimum detectable gas concentration with fixed fibre attenuation in our model will be discussed in detail in the following section.

Ⅱ. Modelling results of the detectable gas concentration range and the minimum detectable gas concentration of different gas cell length *l* , with variable fibre gas cell length difference *x* and fixed fibre base attenuation α=*0.9dB/cm*

The modelling results of the minimum detectable gas concentration shift with gas cell length using fibre gas cell length difference from 60cm to 40cm and fixed fibre base attenuation of 0.9dB/cm are shown in figure 5.22.

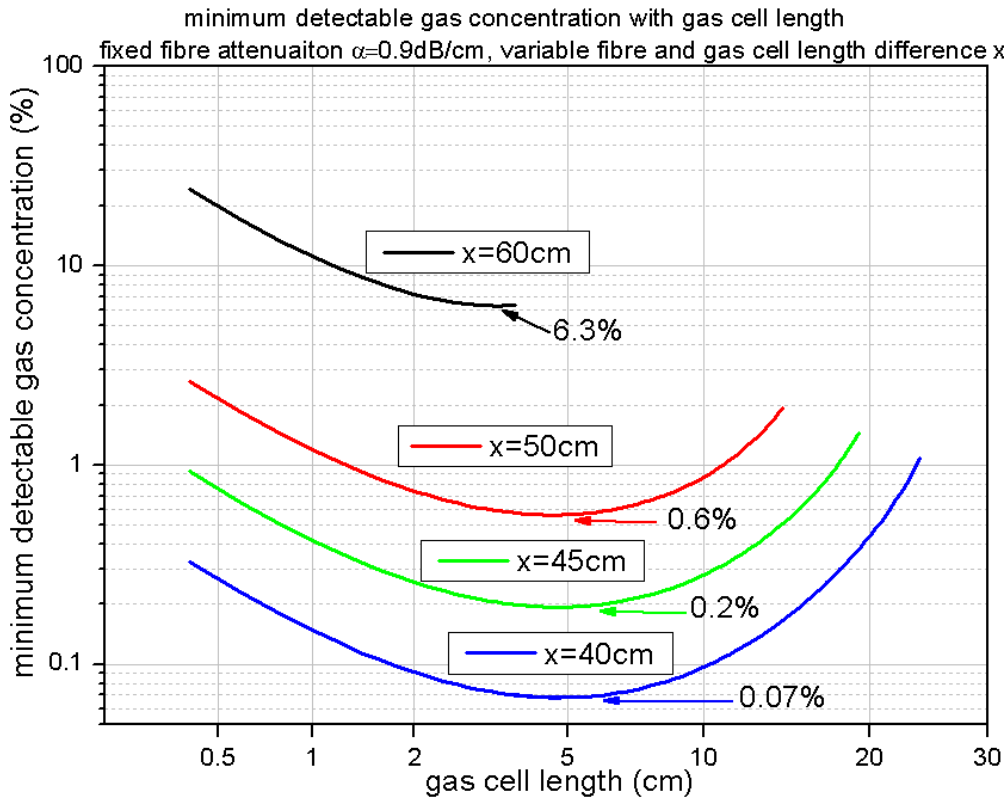

Fig 5.22 Comparisons of minimum detectable gas concentration shift with gas cell length, in which fibre and gas cell length difference is from 40cm to 60cm and fibre attenuation is fixed with 0.9dB/cm

Figure 5.22 shows that with the fixed fibre attenuation of 0.9dB/cm, 0.07% gas concentration can be detected if the length difference between fibre and gas cell is 40cm, while the minimum detectable gas concentration is about 6.3% when the fibre gas cell length difference is 60cm. We can conclude that in order to enhance the sensor

sensitivity, shorter fibre leads should be used for the entry and exit from the gas sensing taper if the attenuation of the fibre being used is large.

The detectable gas concentration range, maximum gas cell length and minimum detectable gas concentration shift with gas cell length of sensing devices with fibre intrinsic attenuation from 1dB/cm to 1.2dB/cm, fibre gas cell length difference from 25cm to 50cm have also been analysed and all the results are shown in table 5.1, and the gas concentration resolution is about in 10ppm magnitude.

Table 5.1 Modelling results summary of variable fibre attenuation and fibre gas cell length difference

Fibre and gas cell length difference	Fibre base attenuation (dB/cm)	Max gas cell length (cm)	Min detectable gas concentration with cell length
60cm	0.1	500	<0.01% gas concentration can be detected when the cell length <450cm
	0.2	220	<0.01% gas concentration can be detected when the cell length <180cm
	0.3	130	<0.01% gas concentration can be detected when the cell length <90cm
	0.4	80	<0.01% gas concentration can be detected with the cell length <44cm
	0.5	54	<0.01% gas concentration can be detected with the cell length range 6~10cm
	0.6	35	<0.06% gas concentration can be detected with the cell length range 3~15cm
	0.7	22	Minimum 0.2% gas concentration can be detected with the cell length of 6cm
	0.8	11	Minimum 1% gas concentration can be detected with the cell length of 5cm
	0.9	3	Minimum 6.3% gas concentration can be detected with the cell length of 3cm
50cm		13.2	Minimum 0.6% gas concentration can be detected with the cell length of 4.6cm
45cm	0.9	18.2	<0.2% gas concentration can be detected with the cell length range 4.6~4.9cm
40cm		23	<0.07% gas concentration can be detected with the cell length range 3.8~6cm
50cm		7	Minimum 2.8% gas concentration can be detected with the cell length of 3.8cm
45cm	1	11.8	Minimum 0.65% gas concentration can be detected with the cell length of 4.2cm
35cm		22	<0.06% gas concentration can be detected with the cell length range 3.6~5cm
30cm	1.1	22	<0.05% gas concentration can be detected with the cell length range 2~7cm
25cm	1.2	22	<0.03% gas concentration can be detected with the cell length range 1~7cm

From above analyses, we can conclude that: for the gas sensing device with given light source and detector system sensitivity, transmitted optical power loss due to the fibre attenuation shows negative effect to the device sensitivity (minimum detectable gas concentration), which competes with the effect from gas absorption to determine the minimum detectable gas concentration. The two important ways to minimize this negative effect are reducing the fibre intrinsic attenuation as much as possible by means of well controlled fabrication processes, or decreasing the length difference between fibre and gas cell in the sensing device. Overall this gas sensing model using tapered fibre evanescent field shows the relationship of maximum gas cell length (sensing fibre length), detectable gas concentration range and minimum detectable gas concentration with gas light interaction length, and gives the required gas cell length (sensing fibre length) range for the expected minimum detectable gas concentration. This gives guidance for the effective length of sensing fibre choice according to different minimum detectable gas concentration requirement in practice.

Model validity verification

In order to verify the validity, the model was applied for two cases reported on literature and compared with the experimental value.

(1) In reference 5.16, the methane gas detection using a hollow core photonic bandgap fibre with weak absorption lines in the near infrared $\nu_2+2\nu_3$ band at 1.3μm was experimentally measured, and the theoretical minimum detectable gas concentration for this system was estimated to be 49ppm. According to the parameter in literature, the minimum detectable gas concentration was also calculated to be about 4ppm using equation 5.13 in our modelling, which is an order of magnitude lower than the value of 49ppm in the literature. This discrepancy can be explained by system losses such as coupling loss that are not considered in our modelling.

(2) For case 2 in reference 5.29, a standard multimode step-index tapered silica fibre with different taper diameter was used as evanescent field methane gas sensor. The minimum detectable concentration of methane was about 1%. Using the same parameter as in literature: fibre attenuation α_1= 0.9dB/cm, gas absorption coefficient α=8.3atm/cm, evanescent field ratio η=0.4, fibre and gas cell length difference 40cm and gas cell length 1cm, the minimum detectable gas concentration is calculated to be about 0.2%, as shown in figure 5.23. The discrepancy of the modelling calculation with

the experimental measurement in literature maybe comes from the source intensity and detector system sensitivity difference.

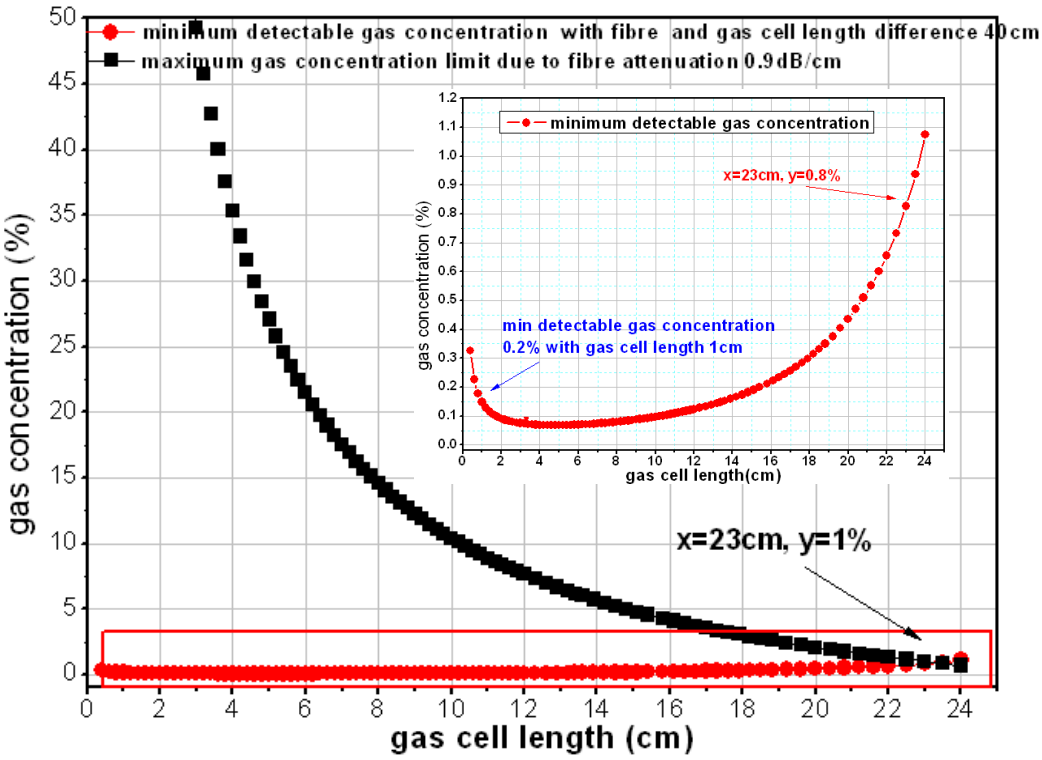

Fig 5.23 Modelling results using the parameters in reference 5.29

Overall, our modelling results are roughly consistent with the experimental measurement values in literature since the model is a somewhat simplified version of the gas sensing device, which verifies the validity of our modelling to a certain extent.

5.6 Tapered fibre fabrication

Tapered optical fibre devices have been widely used for many optical applications, such as supercontinuum generation, interferometric devices, couplers, and sensors. In section 5.5, an optical fibre evanescent field gas sensing device using a tapered germanate glass fibre as the sensing element was modelled and analysed, in which the higher evanescent field ratio and lower transmission loss of the tapered fibre are key factors for device sensitivity. Now the silica nanofibres with diameter reduced to 260nm and length of about 4mm can be obtained using two step taper drawing method [5.31] which opens the possibility of taper tellurite or germanate glass fibre fabrications with micrometer diameters.

In this section, tapering of germanate fibre using a Vytran filament fusion splicer and its transmission measurement are reported in detail.

Vytran FFS-2000 filament fusion splicer, which is typically used for splicing silica fibres, is used in our experiment for the taper fabrication. Using a machine level macro, the fibre holding block (FHB) speed, the pulling distance of the FHBs, the filament fusion power were optimised to control the taper process. The macro obtained from Vytran and the optimised codes used in fabrication of our tapers are shown in appendix B as B.1 and B.2 respectively. The parameters that were changed and the new introduced codes are indicated in bold letters. Using this setup, different tapers with thinnest diameter from 18μm~80μm were obtained by changing the macro codes to control the taper process, as shown in figure 5.24(a~f).

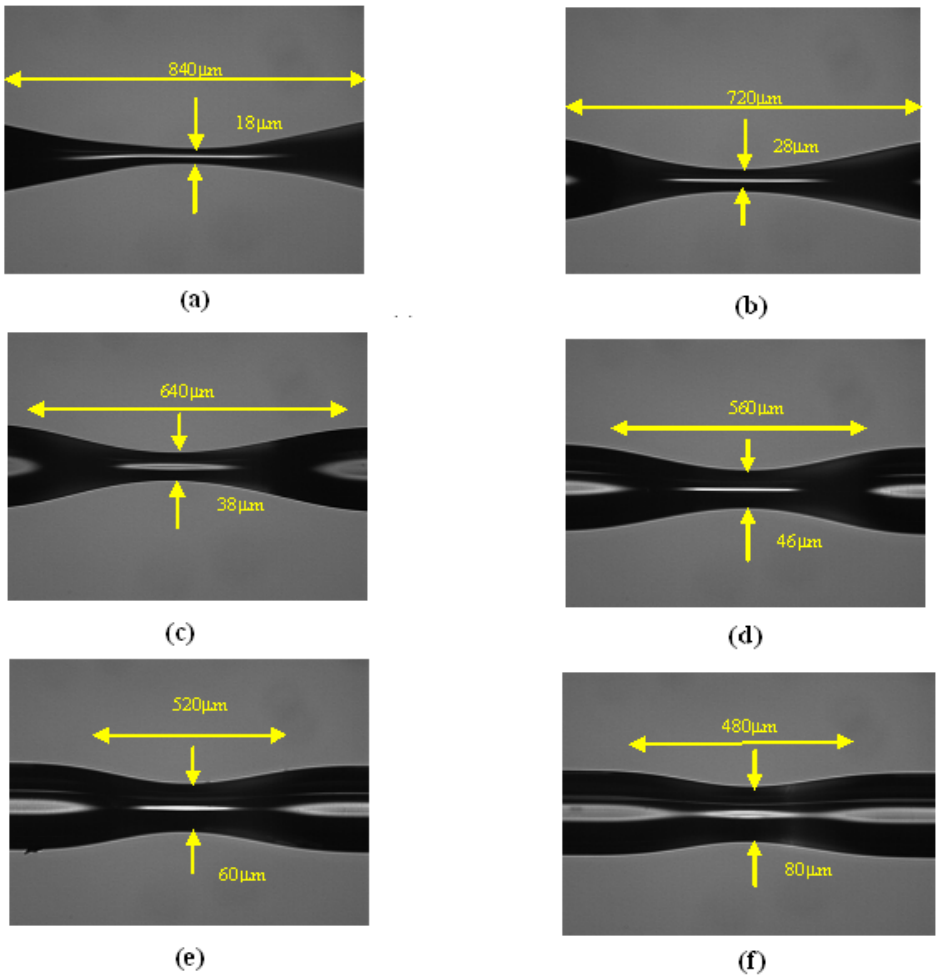

Fig 5.24 Different tapers with thinnest diameter from 18μm to 80μm

Figure 5.24 shows that the thinnest tapered germanate fibre that can be obtained using Vytran splicer is about 18μm with the taper length of 840μm due to the setup

limitation. Although they are not ideal as the sensing elements in an evanescent field gas sensing device due to their lower power ratio in evanescent field according to modelling in section 5.3.2, the parameters control and fibre handle in the germanate fibre tapering process maybe offer some guidance for the future tapering work of this type of glasses using different drawing processes.

An IQS-2300 ASE broadband source operating at 1550nm wavelength with an output power of about 11dBm, and a fibre optic power metre FOT-90A were used to measure the transmission powers before and after tapering. The broadband source was launched into the fibre, and the output power was measured before and after tapering. During this measurement process, the fibre was kept straight and untouched before and after tapering. The output power after tapering were roughly equal to that before tapering, and higher transmission were found in the measurement for different diameter tapers from 18μm to 80μm. That can be explained using our modelling in section 5.3.2: the evanescent field is external to the fibre core while still being guided by the fibre cladding at the taper waist, and as the fibre tapers back to its original size, the field is recaptured by the fibre core. The mode field couples between the core and cladding and the total optical power in the taper remains constant.

On the other hand, we also found that the transmitted power was very sensitive to a small bending or shape change of the fibre, that maybe due to the power loss of the modes guided by the cladding through radiation when the taper is bent. This character of output power variation in a taper due to the bend in the stretched region offers potential of the tapered fibre as displacement, strain or pressure sensors.

5.7 Conclusion

The modelling of mid-infrared glass fibre for evanescent field gas sensing has been described and results predicted. Detected gas species absorption spectrum and optical source in the mid-infrared area have been introduced and investigated. The power ratio of the evanescent wave to total propagating wave in different type of sensing fibres, D-shaped and tapered fibres, have been modelled and tapered sensing fibre fabrication have been investigated. Influence of the fibre attenuation on the device sensitivity have been analysed in detail, the relationship of the minimum detectable gas concentration with gas cell length (sensing fibre length) for various fibre attenuation and fibre cell length differences have been investigated and obtained. Overall this model

shows the maximum gas cell length (sensing fibre length), detectable gas concentration range, and required gas cell length range for the expected minimum detectable gas concentration, which gives guidance for the effective gas cell length choice according to different minimum detectable gas concentration requirement in practice. The model has been applied to two cases reported in the literatures and compared with the experimental values. The model results are roughly consistent with the experimental measurement values in the literature since the model is a somewhat simplified version of the gas sensing device, which verifies the validity of this modelling to a certain extent. Tapering of germanate fibre with diameter of 18μm to 80μm using a Vytran filament fusion splicer have been obtained. This work offers some guidance for the future tapering work of this type of glasses using different drawing processes, although they are not ideal as the sensing elements in an optical fibre evanescent field gas sensing device due to their lower power ratio in the evanescent field because of the high refractive index and difficulty in producing long sub micrometer lengths of fibre.

5.8 References

[5.1] G. Whitenett, G. Stewart, K. Atherton, B. Culshaw, W. Johnstone. *Opitcal fibre instrumentation for environmental monitoring application*. Journal of Optics A: Pure and Applied Optics, Vol. 5, pp. 140-145, 2003

[5.2] W. H. Weber, T. J. Remillard, R. E. Chase, J. F. Richert, F. Capasso, C. Gmachl, A. L. Hutchinson, D. L. Sivco, J. N. Baillargeon, A. Y. Cho. *Using a wavelength-modulaiton quantum cascade laser to measure NO concentration in the parts-per-billion range for vehicle emissions certification*. Applied Spectroscopy, Vol. 56, pp. 706-714, 2002

[5.3] S. A. Kharitonov, P. J. Barnes. *Clinical aspects of exhaled nitric oxide*. European Respiratory Journal, Vol. 16, pp. 781-792, 2000

[5.4] S. A. Kharitonov, P. J. Barnes. *Exhaled markers of pulmonary disease.* American Journal of Respiratory and Critical Care Medicine, Vol. 163, pp. 1693-1722, 2001

[5.5] H. K. Jones, J. Elgy. *Remote sensing to assess landfill gas migration*. Waste Management & Research, Vol. 12, pp. 327-337, 1994

[5.6] K. Jain, R. P. Pant, S. T. Lakshmikumar. *Effect of Ni doping on thich film SnO2 gas sensor*. Sensors and Actuators B: Chemical, Vol. 113, pp. 823-829, 2006

[5.7] G. Eranna, B. C. Joshi, D. P. Runthala, R. P. Gupta. *Oxide materials for development of integrated gas sensors-A comprehensive review*. Critical Reviews in Solid State and Materials Sciences, Vol. 29, pp. 111-188, 2004

[5.8] G. Duxbury, N. Langford. *Quantum cascade lasers bring sensitivity and speed to infrared gas sensing.* Spectroscopy Europe, Vol. 18, No. 5, pp.18-23, 2006

[5.9] G. Stewart, W. Jin, B. Gulshaw. *Prospects for fibre-optic evanescent-field gas sensors using absorption in the near-infrared.* Sensors and Actuators B: Chemical, Vol. 38-39, pp. 42-47, 1997

[5.10] M. L. Silva, D. M. Sonnenfroh, D. I. Rosen, M. G. Allen, A. O'Keefe. *Integrated cavity output spectroscopy measurements of nitric oxide levels in breath with a pulsed room-temperature quantum cascade laser*. Applied Physics B: Lasers and Optics, Vol. 81, pp. 705-710, 2005

[5.11] A. Kosterev, G. Wysocki, Y. Bakhirkin, S. So, R. Lewicki, M. Fraser, F. Tittel, R. F. Curl. *Application of quantum cascade lasers to trace gas analysis.* Applied Physics B: Lasers and Optics, Vol. 90, pp. 165-176, 2008

[5.12] P. F. Bemath. *Spectra of Atoms and Molecules.* Oxford University Press, 2005

[5.13] P. Pfeiffer, P. Meyrueis, D. Patillon, F. Bounaix. *Limiting sensitivity of a differential absorption spectrometer with direct detection in the $2\nu_3$ and $\nu_2+2\nu_3$ vibration bands.* IEEE Transactions on Instrumentation and measurement, Vol. 53, pp. 45-50, 2004

[5.14] L. S. Rothman, C.P. Rinsland, A. Goldman, S. T. Massie, D. P. Edwards, J. M. Flaud, A. Perrin, C. Camy-Peyet, V. Dana, J. Y. Mandin. *The HINTRAN molecular spectroscopic database and HAWKS (HITRAN atmospheric workstation): 1996 edition.* Journal of Quantitative Spectroscopy & Radiative Transfer, Vol. 60, pp. 665-7120, 1998

[5.15] M. Kuntz, M. Hopfner. *Efficient line-by-line calculation of absorption coefficients.* Journal of Quantitative Spectroscopy & Radiative Transfer, Vol. 63, pp. 97-114, 1999

[5.16] A. M. Cubillas, J. M. Lazaro, M. Silva-Lopez, O. M. Conde, M. N. Petrovich, J. M. Lopez-Higuera. *Methane sensing at 1300nm band with hollow-core photonic bandgap fibre as gas cell.* Electronics Letters, Vol. 44, No. 6, 2008

[5.17] K. A. Tillman, D. T. Reid. *Monolithic optical parametric oscillator using chirped quasi-phase matching.* Optics Letters, Vol. 32, No. 11, pp. 1548-1550, 2007

[5.18] L. S. Rothman, D. Jacquemart, A. Barbe, D. Chirs Benner, M. Birk, L. R. Brown, M. R. Carleer, C. Chackerian Jr., K. Chance, L. H. Coudert, et.al. *The HITRAN 2004 molecular spectroscopic database.* Journal of Quantitative Spectroscopy & Radiative Transfer, Vol. 96, pp. 139-204, 2005

[5.19] R. A. Bergh, G. Kotler, H. J. Shaw. *Single-mode fibre-optic directional coupler.* Electronics Letters, Vol. 16, pp. 260, 1980

[5.20] R. B. Dyott, P. F. Shrank. *Self-locating elliptically cored fibre with an accessible guiding region.* Electronics Letters, Vol. 18, pp. 980, 1982

[5.21] F. A. Muhammad, G. Stewart. *Polarised finite-difference analysis of D – fibre and application for chemical sensing.* International Journal of Optoelectronics, Vol. 7, No. 6, pp. 705-721, 1992

[5.22] G. Stewart, J. Norris, D. F. Clark, B. Culshaw. *Evanescent-wave chemical sensors – a theoretical evaluation.* International Journal of Optoelectronics, Vol. 6, No. 3, pp. 227-238, 1991

[5.23] F. A. Muhammad, G. Stewart, W. Jin. *Sensitivity enhancement of D – fibre methane gas sensor using high-index overlay.* IEE Proceedings – J, Vol. 140, No. 2, pp. 115-118, 1993

[5.24] J. A. Buck. *Fundamentals of Optical Fibres*. Wiley-Interscience, 1995

[5.25] A. J. Fielding, K. Edinger, C. C. Davis. *Experimental observation of mode evolution in single-mode tapered optical fibers.* Journal of Lightwave Technology. Vol. 17, No. 9, pp. 1649-1656, 1999

[5.26] J. Lou, L. Tong, Z. Ye. *Modeling of silica nanowires for optical sensing.* Optics Express, Vol. 13, No. 6, pp. 2135-2140, 2005

[5.27] W. Huang, C. Xu, S. T. Chu, S. K. Chaudhuri. *The finite – difference vector beam propagation method: analysis and assessment.* Journal of Lightwave Technology, Vol. 10, No. 3, pp. 295-305, 1992

[5.28] S. Huntington, J. Katsifolis, P. N. Moar, P. Mulvaney, A. Roberts, L. W. Cahill, K. A. Nugent. *Evanescent field characterisation of tapered optical fibre sensors in liquid enviroments using near field scanning optical microscopy and atomic force microscopy.* IEE Proceedings of Optoelectronics, Vol. 146, No. 5, pp. 239-243, 1999

[5.29] H. Tai, H. Tanaka, T. Yoshino. *Fiber – optic evanescent – wave methane – gas sensor using optical absorption for the 3.392 – μm line of He – Ne laser.* Optics Express, Vol. 12, No. 6, pp. 437-439, 1987

[5.30] *PbSe infrared detector, model PDA20H*, Thorlabs

[5.31] A. Lin, A. Zhang, E. J. Bushong, J. Toulouse. *Solid-core tellurite glass fiber for infrared and nonlinear applications.* Optics Express, Vol. 17, No. 19, pp. 16716-16721, 2009

Chapter 6

Discussion and Conclusion

6.1 Introduction

In this thesis, the sensing properties of infrared tellurite and germanate glass fibres have been investigated. An asymmetric fusion splicing technique has been demonstrated and applied for the splicing of tellurite or germanate glass fibre to standard silica fibre due to their lower melting temperatures. The thermal and strain sensing properties of these glass fibres have been studied by analysing the properties of optical fibre Fabry – Perot cavities, which were formed when these high refractive index fibres were spliced to silica fibre, and fibre Bragg gratings. The design of a germanate glass fibre evanescent field gas sensor has been investigated and modelled. This model analysed the influence of the fibre attenuation on the device sensitivity, and showed the relationship of the minimum detectable gas concentration with gas cell length (sensing fibre length) for various fibre attenuation and fibre cell length differences. This data gives guidance for the effective gas cell length choosing according to different minimum detectable gas concentration requirement in practise.

6.2 Thermal Properties

We have experimentally investigated the dispersion character and thermal sensing property of tellurite and germanate glass fibres in this thesis. Using the low-coherence Michelson interferometer and dispersive Fourier transform spectroscopy (DFTS), the effective refractive index and group velocity dispersion of tellurite and germanate fibres were measured. The tellurite fibre has a relatively large refractive index of 2.03, which is about 40% higher than that of silica fibre 1.46. This high

refractive index character offers potential applications of tellurite glass fibre for stimulated Brillouin amplifiers.

An asymmetric fusion splicing technique has been demonstrated and applied for the splicing of tellurite or germanate glass fibre to standard silica fibre. The thermo – optical properties of these two material fibres were investigated by analysing the phase change to temperature of fibre Fabry-Perot interferometers, formed when these tellurite and germanate glass fibres were spliced to silica fibre using this asymmetric splicing method, and the wavelength shift to temperature of FBGs on them. Their temperature coefficients of interferometric phase have been measured to be 89.3± 0.3 rad m^{-1} K^{-1} (tellurite) and 116.5± 0.4rad m^{-1} K^{-1} (germanate) at the mean wavelength of 1536nm in the range 280K to 320K. The core refractive indices (2.03 and 1.83) were consistent with the measured free spectral ranges. The normalized thermal sensitivity of germanate fibre from F-P interferometer and FBG measurement is 15.56×10^{-6}/°C and 16.04×10^{-6}/°C, respectively. For tellurite glass fibre, the normalized thermal sensitivity from F-P interferometer and FBG measurement is about 10.76×10^{-6}/°C and 11.34×10^{-6}/°C, respectively. These measurement values are also in reasonable agreement with values estimated using published data for fibre with similar compositions.

The contributions from the thermal expansion coefficient and thermo-optic coefficient to the fibre thermal sensitivity were analysed, verifying the negative value of thermo-optic coefficient of tellurite glass fibre which can be attributed to its higher thermal expansion coefficient compared with germanate fibre. The thermal responses of germanate glass fibre is about 30% larger than that of tellurite glass fibre even though tellurite fibre has a higher thermal expansion coefficient however this effect is offset by the negative thermal optic term. Compared with fused silica fibre, the thermal reponses of tellurite and germanate glass fibres are both higher than that (normalized thermal response 8.89×10^{-6}/°C) of fused silica fibre. For tellurite fibre the thermal response is about 20% larger than fused silica fibre, while for germanate fibre it is nearly 80% larger than fused silica fibre. Therefore tellurite or germanate glass fibres would show advantages as thermal sensing elements.

6.3 Strain Sensitivities

We have measured the strain response and Young's modulus of tellurite and germanate glass fibres using fibre Fabry-Perot interferometer and fibre Bragg grating

techniques. The optical phase sensitivity to strain and the normalized strain sensitivity of germanate glass fibre were measured as $(6100\pm300)\times10^3$ rad/m and 0.817×10^{-6} /με respectively at 1540nm by a Fabry-Perot cavity interferometer, which is consistent with the value of 0.805×10^{-6} /με from 2nd order fibre Bragg grating measurement. The Young's modulus was measured to be 53GPa. The strain sensitivity and Young's modulus of tellurite fibre were measured as $(5600\pm200)\times10^3$ rad/m and 37GPa respectively using an FFP interferometer. The strain response of tellurite and germanate glass fibre were also theoretically evaluated, and all the experimental measurement results are broadly consistent with values predicted using available published data for glasses of similar compositions.

Compared with fused silica fibre, the phase change per unit length per unit strain ($d\phi/dL$) in germanate and tellurite fibre, with values of $(6100\pm300)\times10^3$ rad/m and $(5600\pm200)\times10^3$ rad/m respectively, are about 30% larger than that in fused silica fibre ($\sim4600\times10^3$ rad/m). Moreover, if we consider the phase change per unit length per unit stress ($\frac{1}{E}\frac{d\phi}{dL}$), the smaller Young's modulus of tellurite fibre (37GPa) compared to fused silica (72GPa) leads to a larger response by a factor of nearly 1.9, then the phase change per unit length per unit stress in tellurite fibre is about 2.5 times of that in fused silica fibre. Therefore tellurite and germinate glass fibres show potential as load sensing element.

6.4 Modelling of Germanate Glass Fibre for Evanescent Field Gas Sensing

The design of a germanate glass fibre evanescent field gas sensor was investigated and modelled. A nanosecond monolithic optical parametric oscillator (OPO) with idler light output tuned from 3 μm to 3.4μm with the temperature shift range of 20°C~180°C has been demonstrated, which covers the central part of the methane gas fundamental vibration absorption spectrum range (3.1~3.5μm) and was applied in the modelling. A tapered germanate glass fibre was used as the sensing element, and the power in the evanescent wave to the total power of the propagating wave for the tapered sensing fibre with different taper diameters were modelled and calculated.

In the model, the influence of the fibre attenuation on the device sensitivity have been analysed in detail. The relationship of the minimum detectable gas concentration

with gas cell length (sensing fibre length) for various fibre attenuation and fibre cell length differences have been investigated and obtained. This model shows the maximum gas cell length (sensing fibre length), detectable gas concentration range, and required gas cell length range for the expected minimum detectable gas concentration of a fibre evanescent field sensor, which gives guidance for the effective gas cell length choice according to different minimum detectable gas concentration requirement in practise. The model has been applied to two cases reported in the literature and compared with the experimental values, and the model results are roughly consistent with the experimental measurement values in the literature since the model is a somewhat simplified version of the gas sensing device; that verifies the validity of this modelling to a certain extent.

Tapering of germanate fibre with diameter of 18μm to 80μm using a Vytran filament fusion splicer has been demonstrated. Although they are not ideal as the sensing elements in an optical fibre evanescent field gas sensing device due to the lower power ratio in evanescent field, the parameters controlling and fibre handling in the germanate fibre tapering process maybe offer some guidance for the future tapering work of this type of glasses using different drawing processes.

6.5 Future Work

The research described in this thesis was to investigate the sensing properties of mid-infrared tellurite and germanate glass fibres. In chapter 3 and 4, the thermo-optical properties and elastic-optical properties of tellurite and germanate fibre have been studied by analysing the optical properties of these material glasses fibre Fabry-Perot interferometer and fibre Bragg grating in them. Both of them show potential as thermal sensing and load sensing elements in sensor devices compared with silica fibre. Therefore future work should be focused on how to apply these novel fibres with transmission in the near- and mid-infrared region as sensors for temperature, strain, loading and multi-parameter measurements. Moreover, multicore fibres as a new fibre structure have been used to develop various types of mechanical sensors to measure curvature [6.1], orientation [6.2] and transverse loading [6.3] and highlighted in a number of reports [6.4, 6.5]. However, most of these works have involved silicate glass optical fibres. Investigating sensing properties of multicore tellurite or germanate glass fibre would bring major benefits to some of the applications mentioned above.

In chapter 5, we modelled the optical fibre evanescent field gas sensor for methane species detection, in which a tapered germanate fibre was used as the sensing element. Due the simplicity of this model, more detailed aspects should be analysed and studied in future works such as the fabrication of fibre taper with diameter lower than 1μm and its optical transmission analysis, signal processing and overall process monitoring.

Recently there are many types of fibres being developed and used in the sensing of gas species and their concentrations. Solid core silica fibre is well developed and had also been used in the sensing of gas species and concentrations by exploiting the weak overtone molecular vibrations below 2μm, however, long interaction lengths and high-sensitivity techniques are required to make useful gas concentration measurements. hollow core photonic bandgap fibre, which offers advantages of higher light gas interaction strength because such fibres can guide over 99% [6.6] of the light outside the fibre material and into the hollow core, while the diffusion time of the gas into the sensing region such as the air core for hollow-core fibre should be taken into account for sensor design. Potential transmission properties in the near- and mid-infrared region (1～5μm) of tellurite, germanate and chalcogenide glass fibres remove the restriction to near-infrared wavelengths associated with silica fibres, which offer great advantages for them as chemical sensing elements for qualitative and quantitative detection of liquid and gaseous chemical species due to the access to the much stronger fundamental absorption bands although their fabrication is not as well developed as for silica. Moreover, exploring alternative fibre structures, such as multicore fibre, micro-structured fibre such as photonic bandgap or hollow core fibre, of these mid-infrared transmission glass fibres as sensing elements would be relevant and perspective for liquid and gaseous chemical species detection.

6.6 Thesis Conclusion

In conclusion, in this thesis the characteristics and sensing properties of novel mid-infrared tellurite and germanate glass fibres have been described. Using fibre Fabry-Perot interferometer and fibre Bragg grating techniques, the thermal and strain sensing properties of these material glass fibres were investigated, and show their potential as thermal sensing and load sensing elements. The design of evanescent field

gas sensor using tapered germanate fibre as sensing element for methane gas species detection has been investigated and modelled. This model shows the maximum gas cell length (sensing fibre length), detectable gas concentration range, and required gas cell length range for the expected minimum detectable gas concentration of a fibre evanescent field sensor, which gives guidance for the effective gas cell length choice according to different minimum detectable gas concentration requirement in practice.

6.7 References

[6.1]. G. M. H. Flockhart, W. N. MacPherson, J. S. Barton, J. D. C. Jones, L. Zhang, I. Bennion. *Two-axis bend measurement with Bragg gratings in multicore optical fiber.* Optics Letters, Vol. 28, No. 6, pp. 387-389, 2003

[6.2]. W. N. MacPherson, G. M. H. Flockhart, R. R. J. Maier, J. S. Barton, J. D. C. Jones, D. Zhao, L. Zhang, I. Bennion. *Pitch and roll sensing using fibre Bragg gratings in multicore fibre.* Measurement Science and Technology, Vol. 15, pp. 1642-1646, 2004

[6.3]. M. Silva-Lopez, C. Li, W. N. MacPherson, A. J. Moore, J. S. Barton, J. D. C. Jones, L. Zhang, I. Bennion. *Transverse load and orientation measurement using multicore fibre Bragg gratings.* Applied Optics, Vol. 44, No. 32, pp. 6890-6897, 2005

[6.4]. A. Fender, E. J. Rigg, R. R. J. Maier, W. N. MacPherson, J. S. Barton, A. J. Moore, J. D. C. Jones, D. Zhao, L. Zhang, I. Bennion, S. McCulloch, B. J. S. Jones. *Dynamic two-axis curvature measurement using multicore fiber Bragg gratings interrogated by arrayed waveguide gratings.* Applied Optics, Vol. 45, pp. 9041-9048, 2006

[6.5]. A. Fender, W. N. MacPherson, R. R. J. Maier, J. S. Barton, D. S. George, R. I. Howden, G. W. Smith, B. J. S. Jones, S. McCulloch, X. Chen, R. Suo, L. Zhang, I. Bennion. *Two-axis temperature-insensitivite accelerometer based on multicore fiber Bragg gratings.* IEEE Sensors J, Vol. 8, pp. 1292-1298, 2008

[6.6]. N. Gayraud, l. W. Kornaszewski, J. M. Stone, J. C. Knight, D. T. Reid, D. P. Hand, W. N. MacPherson. *Mid-infrared gas sensing using a photonic bandgap fiber.* Applied Optics, Vol. 47, pp. 1269-1277, 2008

Appendix A: Matlab Language Code for DFTS Signal Processing to get the Interferograms and Fibre Dispersion

A. 1

```
function [Spect, Phase, WavRange, OptFreq] = spectph(Spectrum, MaxWav, MinWav,
Delay, NrResampPoints, Windo);

SpeedOfLight    =0.299792458; % um/fs

OptMin = 2*pi*SpeedOfLight*1e3./MaxWav;
OptMax = 2*pi*SpeedOfLight*1e3./MinWav;
ResampFFTfint = (2*pi)/(NrResampPoints*Delay);
MinLimit = ceil((OptMin/ResampFFTfint) + 1);
MaxLimit = floor((OptMax/ResampFFTfint) + 1);

MinWin = find(Windo == MinLimit);
MaxWin = find(Windo == MaxLimit);
PlotWindo = MaxWin:MinWin;
Spect = Spectrum(PlotWindo);
ResampFFTfint          = (2*pi)/(NrResampPoints*Delay);
OptFreq  = (Windo(MinWin:MaxWin)-1)*ResampFFTfint;
WavRange = 2*pi*SpeedOfLight*1e3./(OptFreq);
Phase = unwrap(angle(Spect));
```

A. 2

```
clear all
% Constants all in fu (micron fs (PHz)) units
RefSigWavelength = 0.63282;          %Microns
SpeedOfLight     = 0.299792458;      % um/fs

%1. AQUIRE SIGNALS
directoryname='    ';       % Directory containing datafiles.
FileLabel ='1';

Start =1;
```

```
Stop = Start;

ZWinSize = 16384;          % 8192
BWinSize = 16384;          %65536; %32768;
offset = 300000;
ZeroCross = 2;             % Number of zerocrossing per fringe i.e. 1 or 2.
ZExpand =0;                % Control of zeropadding
BExpand =0;

filename = [directoryname FileLabel 'log.txt'];
fidlog = fopen(filename, 'a+t');
i=1;
for Fnumber = Start:Stop;

   %Signal in .bin format. ( From LabView DAQ, signed word integers -16 bit)

filedata = [FileLabel '.dat'];                %[FileLabel num2str(Fnumber) '.dat'];
filename = [directoryname filedata];
SaveFile = [directoryname FileLabel  num2str(Fnumber) 'ex1.mat'];

fprintf(1,'Starting to process %s.\n\n', filename);
pause(1)
fid=fopen(filename);
Sig = fread(fid,[1,inf],'int16');
fclose(fid);


   %2. Signal processing

[ma, mizero] = max(Sig(1:300000));    %Maximum location of zero OPD
[ma, mibal] = max(Sig(mizero + offset:length(Sig)));
mibal = mizero+offset+mibal-1;

ZeroInt = Sig(mizero - (ZWinSize/2) +1:mizero + (ZWinSize/2));
BalInt = Sig(mibal - (BWinSize/2) +1:mibal + (BWinSize/2));

   % The delay interval is set by the zero crossing of the HeNe. Each sample is aquired
with am OPD difference of 632.82nm

DelayInterval = RefSigWavelength/(ZeroCross * SpeedOfLight);        %in (fs)

   % Generate Spectrum

MinWl = 1400; %nm
MaxWl = 1700; %nm

[ZeroIntSp, ZWindo, ZNrResampPoints] = fftspect(ZeroInt,MaxWl,MinWl,
DelayInterval ,ZExpand);
[BalIntSp, BWindo, BNrResampPoints] = fftspect(BalInt,MaxWl,MinWl,
DelayInterval ,BExpand);
```

```
MinPlWl = 1480; %nm
MaxPlWl = 1600; %nm

[ZSp(i,:), ZPh(i,:), ZWl, ZFr] = spectph(ZeroIntSp, MaxPlWl, MinPlWl, DelayInterval,
ZNrResampPoints, ZWindo);
[BSp(i,:), BPh(i,:), BWl, BFr] = spectph(BalIntSp, MaxPlWl, MinPlWl, DelayInterval,
BNrResampPoints, BWindo);

ZSp(i,:)=ZSp(i,:).*conj(ZSp(i,:));
BSp(i,:)=BSp(i,:).*conj(BSp(i,:));

ZSpn(i,:) = 10*log10(ZSp(i,:)/max(ZSp(i,:)));
BSpn(i,:) = 10*log10(BSp(i,:)/max(BSp(i,:)));
i=i+1;
end

a=41:220;
k =1;
p1=polyfit(ZFr(a)-ZFr(a(length(a)/2)),ZPh(k,a),2);
y1 =polyval(p1,ZFr(a)-ZFr(a(length(a)/2)));
p2=polyfit(BFr(a)-BFr(a(length(a)/2)),BPh(k,a),2);
y2 =polyval(p2,BFr(a)-BFr(a(length(a)/2)));

figure;
plot(ZWl,ZPh',ZWl(a),y1,'r',BWl,BPh',BWl(a),y2,'r')

q2=p2-p1;

d1 = -2*q2(:,1)*ZFr(a(length(a)/2))^2/(2*pi*SpeedOfLight*1e6);     %in units of ps/nm
for length of fibre.

disp=d1*100*1000/(5.0*2);  %(10.01*2);  LENGTH OF FIBRE IN cm
wavelength=ZWl(a(length(a)/2));

fprintf(1,'Dispersion at %g nm is calculated to be %g.\n\n', wavelength, disp);
```

Appendix B: Vytran FFS-2000 Filament Fusion Splicer Macro

B. 1 Macro from Vytran Splicer

enablefilament (0) 10	;make sure the filament is off
setdac (4 1300) 20	;set argon to 0.65ish l/min. Note argon interlock not working in macro
setdac (50) 30	;filament power is OFF
Motorto (5 750) 40	;move splice head over to taper pos. Change number to alter distance from strip point
Motorvel (7 100) 50	;set left FHB to 100 steps per second
Motorvel (5 25) 60	;set splice head to ¼ of the FHB vel
Enablefilament (1) 2000	;filament is enabled
Setdac (5 861) 2010	;filament power is set filament is on
Motorexstep (7 -1920) 2020	;left FHB moving out 1920 steps
Motorexstep (5 1000) 2020	;splice head moving right
Macropause (ox1a 1000) 2030	;wait here until the left FHB stops moving
Enablefilament (0) 1	;pause triggered, turn filament OFF
Motorstop (5) 10	;stop splice head
Motorto (5 445) 20	;splice head back to View to Splice position, alter number here to suit
Setdac (4 300) 30	;argon to background
Setdac (5 0) 40	;filament power is OFF
Motorvel (7 2000) 50	;reset left FHB velocity
Motorvel (5 1000) 60	;reset splice head velocity

B. 2 Modified Macro

The introduced code and the main parameters changed in order to obtain good tapers are written in bold.

Enablefilament (0) 10	;make sure the filament is off
setdac (4 1300) 20	;set argon to 0.65ish l/min. Note argon interlock not working in macro
setdac (50) 30	;filament power is OFF
Motorto (5 **500**) 40	;move splice head over to taper pos. Change number to alter distance from strip point
Motorvel (7 **3000**) 50	;set left FHB to 3000 steps per second
Motorvel (8 3000) 50	**;set right FHB to 3000 steps per second**
Motorvel (5 **3000**) 60	;set splice head to ¼ of the FHB vel.
Enablefilament (1) 2000	;filament is enabled
Setdac (5 242) 2010	;filament power is set filament is on
Motorexstep (7 **-5000**) 2020	;left FHB moving out 5000 steps
Motorexstep (8 -5000) 2020	**;right FHB moving out 5000 steps**
Motorexstep (5 1000) 2020	;splice headd moving right
Macropause (ox1a 1000) 2030	;wait here until the left FHB stops moving
Enablefilament (0) 1	;pause triggered, turn filament OFF
Motorstop (5) 10	;stop splice head
Motorto (5 445) 20	;splice head back to View to Splice position, alter number here to suit
Setdac (4 300) 30	;argon to background
Setdac (5 0) 40	;filament power is OFF
Motorvel (7 2000) 50	;reset left FHB velocity
Motorvel (5 1000) 60	;reset splice head velocity
Motorlimits (5 -5000 5000) 1	**;do splice head home**